ISSN 0915-6356

NATIONAL INSTITUTE FOR FUSION SCIENCE

Runaway – Electron – Materials Interaction Studies

H. Bolt and A. Miyahara

(Received – July 31, 1989)

NIFS-TECH-1 Mar. 1990

RESEARCH REPORT
NIFS-TECH Series

NAGOYA, JAPAN

RUNAWAY - ELECTRON - MATERIALS INTERACTION STUDIES

H. Bolt*, A. Miyahara

National Institute for Fusion Science
Nagoya 464-01, Japan

* The NET Team c/o Max-Planck-Institute for Plasma Physics,
Boltzmannstr. 2, D-8046 Garching, Fed.Rep.of Germany.

Abstract

During the operation of magnetic fusion devices it has been frequently observed that runaway electrons can cause severe damage to plasma facing components. The energy of the runaway electrons could possibly reach several 100 MeV in a next generation device with an energy content in the plasma in the order of 100 MJ.

In this study effects of high energy electron - materials interaction were determined by laboratory experiments using particle beam facilities, i. e. the Electron Linear Accelerator of the Institute of Scientific and Industrial Research of Osaka University and the 10 MW Neutral Beam Injection Test Stand of the National Institute for Fusion Science. The experiments and further analyses lead to a first assessment of the damage thresholds of plasma facing materials and components under runaway electron impact.

It was found that metals (stainless steel, molybdenum, tungsten) showed grain growth, crack formation and/or melting already below the threshold for crack initiation on graphite (14-33 MJ/m^2). Strong erosion of carbon materials would occur above 100 MJ/m^2. Damage to metal coolant channels can occur already below an energy deposition of 100 MJ/m^2. The energy deposited in the metal coolant channels depends on the thickness of the plasma facing carbon material D, with the shielding efficiency S of carbon approximately as $S \sim D^{1.15}$.

Key Words: runaway-electrons
disruptions
tokamaks
electron linear accelerator
plasma facing materials

Acknowledgement

The authors greatly acknowledge the help of Prof. Dr. T. Yamamoto of the Institute of Scientific and Industrial Research of Osaka University in providing access to the electron linear accelerator. Thanks are due to the staff of the Radiation Laboratory of the same institute for their support and operation of the accelerator during the experiments.

Contents

1. Introduction

During the operation of magnetic fusion devices the phenomenon of electron runaway in the plasma was frequently observed, e.g. |1-12|. In such cases a part of the thermal electron population is accelerated to very high energies which in present fusion devices may be up to about 100 MeV |13|. Conditions which allow for electron runaway can occur during the initial breakdown phase of a plasma discharge when the electric field is very strong and the plasma particle density is extremely low. Also during low density discharges a fraction of the electrons may be accelerated and carry a considerable part of the discharge current. The most violent formation of runaway-electrons however can occur during the current decay phase of plasma disruptions. Under the electric field which is set up during the current decay a fraction of the plasma electrons is accelerated to high energies within a timescale of milliseconds. The electrons may then either drift towards the plasma facing components of the tokamak or they are forcibly dumped onto component surfaces during positional instabilities of the plasma. In these cases the major part of the electron energy is deposited in the material of the plasma facing components. Thus large fluxes of high energy electrons to the component surface can lead to sudden thermal excursions of the materials which in turn may cause considerable damage to these components and possibly their failure (figure 1.1). Damage of plasma facing components in present day large tokamaks (JT-60, JET, TFTR) like melting, erosion, cracking and fracture was partially caused by runaway-electron impact with energy depositions of up to 500 MJ/m^2 /14-17/.

With regard to large fusion devices of the next generation runaway-electron-materials interaction will be a critical issue in terms of materials selection, component design and component lifetime. It is expected that the increase of the plasma current from 2-7 MA in large present day devices to approximately 22 MA in a next generation device like ITER |18-20| will increase the problems associated with runaway-electron-materials interaction drastically. In addition to the damage of plasma facing materials, the strong dependence of the energy deposition process in a material on the electron energy and

the materials density may lead to significant energy deposition in high density metal structures which are covered towards the plasma by low density plasma facing materials, esp. carbon |21-25|. Thus for example the metal coolant channels of plasma facing components |26-31| might be damaged with the possible consequence of coolant leakage into the vacuum vessel even though these structures are covered by comparatively thick carbon layers.

On this background a study of runaway-electron processes in tokamaks with special emphasis on the runaway-electron-materials interaction during disruptions was performed. The structure of the work is shown in figure 1.2. The runaway-electron generation process and trajectories are treated under the aspect of runaway-electron generation during disruptions. A literature review summarizes the physical high energy electron material interaction effects and the observed runaway-electron related processes in tokamaks like hard x-ray and photoneutron production, material activation by nuclear reactions, and the damage to materials and plasma facing components by runaway-electron impact.

The experimental part is concerned with the effects of high energy electron impact on materials. For the experiments particle beam irradiation facilities were used to simulate the energy deposition process in materials by runaway-electrons. High energy electron irradiation experiments were carried out with the electron linear accelerator of the Radiation Laboratory of the Institute of Scientific and Industrial Research of Osaka University. Here material samples and instrumented probes were subjected to irradiation with 20-30 MeV electrons. By direct evaluation of the structural changes and damage of material samples after irradiation an assessment on their sensitivity to high energy electron impact could be made and a ranking of materials was established. The quantitative determination of the interaction of high energy electrons with carbon metal layer systems was then performed by use of instrumented probes which allowed the measurement of the deposited energy in discrete locations.

The deposition of high heat loads on materials was simulated with an accelerated hydrogen beam. For these experiments the 10 MW Neutral Beam Injection Test Stand of the Institute of Plasma Physics of Nagoya University was used. By adjusting the irradiation parameters to the results of an analysis of the energy deposition by runaway-electrons the response of materials to runaway-electron impact in tokamaks could be determined quantitatively.

The discussion of the implication for next generation devices expands on the analysis of runaway-electron processes and their interaction with wall materials. On the basis of the experimental results the response of materials and plasma facing components is discussed and thresholds values for the occurence of material damage like cracking, erosion and damage of subsurface structures by runaway-electron impact are given.

2. Runaway-Electron Generation in Tokamaks

In magnetic plasma confinement devices [32-37] the phenomenon of electron runaway in tokamaks is a consequence of the long-range, small-angle scattering of particles undergoing collisional interactions [38]. This kind of Coulomb interaction causes a rapid decrease in the cross section for scattering of charged particles, σ, with an increase of velocity, $\sigma \sim v^{-4}$. The dynamic friction force for fast electrons then cannot compensate the acceleration induced by an electric field which results in the continuous acceleration of the electrons [5]. The critical energy for such an electron runaway is defined as the point at which the dynamic friction force and the electric field acceleration of the electrons are balancing each other. The initial gain of energy up to this threshold is followed by further acceleration and may lead to the formation of runaway orbits which, depending on their energy, are more or less displaced from the magnetic flux surfaces and decoupled from the bulk plasma [39]. Further beam formation and pinch processes that lead to an increase of the internal inductance of the runaway components may occur [13].

Finally the runaway electrons will touch the material parts of the plasma containment structure which are most protruding into the plasma. This may happen in a continuous process of runaway electron generation, drift, and runaway electron loss or in a sudden violent dump of energy together with a disruptive termination of the discharge |13,16,17|.

The acceleration of plasma electrons may happen under a number of conditions which can be distinguished as follows:

a) The early generation of runaway-electrons during the tokamak start-up, that is the break-down phase and the early stages of the developing discharges when large electric fields are applied |40|.

b) Steady state runaway processes in discharges of low density where a high energy runaway-tail develops which characterizes the electron distribution function |14,42|. In the case of so-called 'slideaway' discharges a large amount of the current can be carried by the runaway-electron population. Here a large part of the circulating bulk electrons shifts to higher energies |43|. This process can be considerably enhanced by plasma impurities |44|.

c) The acceleration of electrons during the current decay phase of a disruption. Here a fraction of the available electrons is accelerated to very high energies which can carry currents of up to 2 MA in present large devices |10|. The generation of these electrons and their interaction with materials is treated in sections 2.3, 3 and 4.

Of these groups the disruption induced runaway production (c) is posing the most serious threats to the operation of present day and future devices since here significant amounts of energy are carried by the electrons. The uncontrolled way of deposition of this energy onto first wall components can cause severe damage to plasma facing materials. The generation of large runaway electron currents during 'slide-away' discharges may be avoided by a proper selection of the

discharge parameters and control of the discharge. Thus the further discussion will mainly concentrate on disruption produced runaway-electrons.

2.1 Conditions for Electron Runaway

The acceleration of an electron in a plasma is determined by the accelerating electric field and the decelerating friction with other plasma particles. Under the assumption of Maxwellian distributions in space of the electrons and ions the dymanic friction force resulting in the change of momentum of a test particle is given as follows |38|:

$$\langle F \rangle = \sum \frac{4\pi e_t^2 e_f n_f \ln\Lambda}{k T_f} \left(1 + \frac{m}{m_t}\right) G(\xi_f) \qquad \text{[equ. 2.1]}$$

with: $\xi_f = (v_t / v_{thf})$

$$G(\xi) = \frac{\Phi(\xi) - \xi \, d\Phi/d\xi}{2\xi^2}$$

$$\Phi(\xi) = \frac{2}{\sqrt{\pi}} \int_0^{\xi} e^{-t^2} dt$$

$$G(\xi) \longrightarrow \frac{1}{2\xi^2} \qquad \text{when } \xi \longrightarrow \infty$$

$$G(\xi) \longrightarrow \frac{2}{3\sqrt{\pi}} \xi \qquad \text{when } \xi \longrightarrow 0$$

indices: t : test particle
f : distribution of field particles

with: $\ln\Lambda$: Coulomb logarithm

ξ : streaming parameter (i.e. drift over thermal velocity)

n_e: density $n_e = \sum Z_j \cdot n_j$

T : temperature

m : mass

v : electron drift velocity

v_{th} : electron thermal velocity

In the onset of acceleration the friction force for $\xi \ll 1$ is |5|:

$$F(v) = m v \nu \qquad \text{[equ. 2.2]}$$

with ν being the frequency of Coulomb collisions as parameters for the slowing down of electrons:

$$\nu = \frac{4\pi e^4 n_e \ln\Lambda}{m^2 v^3} \qquad \text{[equ. 2.3]}$$

From this a critical velocity v_c can be derived where the electric field is balanced against the friction due to Coulomb collisions; $eE = F\ (v = v_c)$:

$$v_c = v_{th} = \sqrt{kT_e/m} \qquad \text{[equ. 2.4]}$$

$$v_c^2 = \frac{4\pi e^3 n_e \ln\Lambda}{m E} \qquad \text{[equ. 2.5]}$$

Above the critical velocity v_c electrons will be gradually accelerated to high energies. This breakpoint is also defined as critical electric field E_c:

$$E_c = \frac{4\pi e^3 n_e \ln\Lambda}{m v_{th}^2} \qquad \text{[equ. 2.6]}$$

Under this field an electron with the energy $mv^2/2 = T_e$ is accelerated to twice its velocity in the mean free time between two collisions. In this region the original symmetric electron distribution function is changed to a directional one. It should be noted that the critical energy E_c deviates from the Dreicer field by about a factor of 2 |5|. The dependence of the Dreicer field on the plasma density and the plasma temperature is shown in Figure 2.1.
From the definition of the critical field a boundary condition has been derived at which no runaway-electrons are produced. The field E_R is given as |45|:

$$E_R = E_c (kT/m_o c) \qquad \text{[equ. 2.7]}$$

For the determination of runaway rates under electric fields $E \ll E_c$ the Fokker-Planck equation needs to be solved. In a modified linear form this equation may be written as |46|:

$$\frac{\delta f}{\delta t} + E\cos\theta \frac{\delta f}{\delta v} - \frac{E\sin\theta}{v} \frac{\delta f}{\delta \theta} = \frac{1}{v^2} \frac{\delta}{\delta v} v^2 \left(\frac{1}{2} \frac{d^2\psi}{dv^2} \frac{\delta f}{\delta v} - hf\right) + \frac{1}{v\sin\theta} \frac{\delta \sin\theta}{\delta\theta} \frac{1}{2v^2} \frac{d\varphi}{dv} \frac{\delta f}{\delta\theta} \qquad \text{[equ. 2.8]}$$

with

v, θ, Ψ : spherical velocity coordinates with polar axis along E

$$\Psi = \sum_{j=i,e} \varphi_j = \sum_{j=i,e} Z_j (\alpha_j)^{1/2} \left[\chi \Phi(\chi) - \frac{1}{2\chi} \Phi(\chi) + \frac{1}{2} \frac{d\Phi}{d\chi}\right]$$

$$\chi = v/(\alpha_j)^{1/2} \qquad h = \sum_{j=i,e} \alpha_j v^2 \left(\frac{d}{dv}\right) v^2 \psi_j \qquad \alpha_i = \frac{m}{M\sqrt{2}} \qquad \alpha_e = \frac{1}{\sqrt{2}}$$

$$\Phi(\chi) = (2/\sqrt{\pi}) \int_0^{\chi} \exp(-t^2)\, dt$$

indices: i: ion
e: electron

Approximate analytic solutions were given by several authors |47-50|. Kulsrud et al. |46| solved this equation numerically. A comparison of the results is given in Figure 2.2.
Dreicer |51,52| undertook the first examination of the runaway-electron generation. He solved the linearized, time dependent Fokker-Planck equation by expanding the electron distribution function $f(v,t) = f_0(v,t) + \mu f_1(v,t)$, where μ is the cosine of the angle between the electric field E and the velocity v with $f_1 \ll f_0$. However the validity of the theory is limited by the imposed form of the distribution function. In particular, the assumption $f_1 \ll f_0$ is violated for $(v/v_0) > (E_0/E)^{1/4}$ |53|. More accurate treatments were undertaken by Gurevich |48| and Lebedev |49|. Here f was not expanded in powers of μ but ln f was expanded in powers of $1-\mu$ because the distribution function was assumed to be very peaked about $\mu = 1$. Furtherly the macroscopic plasma parameters were fixed at their initial values whereas Dreicer |51,52| followed the evolution of the electron temperature in time |5|. In a work by Kruskal and Bernstein |47| the velocity space was divided into five separate regions and f expanded in powers of E. The runaway-rate then can be given as:

$$\lambda = K n \nu(v_{th}) \left(\frac{E}{E_c}\right)^{-\frac{3}{8}} \exp\left[-\frac{E_c}{E} - \left(\frac{2E_c}{E}\right)^{\frac{1}{2}}\right] \qquad \text{[equ. 2.9]}$$

The numerical solution of the runaway rate by Kulsrud et al. |46| was used to determine the constant K to be K = 0.35.

The effect of impurities on the electron runaway is discussed by Cohen |53|. It is found that different mathematical treatments yield largely different results, see Figure 2.3. Since the numerical results by Kulsrud et al. |46| appear to be conservative compared to

the experimental results the constant in the equation for runaway-rates in an impure plasma by Kruskal and Bernstein |47|

$$\lambda = K(Z_e)\left(\frac{E_c}{E}\right)^{3(Z_e+1)/16} n\nu(v_{th}) \exp\left[-\frac{E_c}{E} - \sqrt{\frac{(Z_e+1)E_c}{E}}\right] \quad \text{[equ. 2.10]}$$

$$Z_e = \frac{1}{n_e}\sum_j n_j Z_j^2 \qquad n_e = \sum_j n_j Z_j$$

can be calibrated to be $K(Z_e) = 0.32$ for $Z_e = 1$, $K(Z_e) = 0.43$ for $Z_e = 2$, $K(Z_e) = 0.42$ for $Z_e = 3$, $K(Z_e) = 0.14$ for $Z_e = 10$. This calibration is for $E/E_c = 0.08$.

2.2 Disruptions

Tokamak plasma disruptions which lead to the production of runaway-electrons have been observed in most machines |e.g. 54-70|. For an understanding of the runaway-production mechanism and the subsequent interaction of runaway-electrons with wall components a summarizing description of the processes associated with the development of disruptions will be given.

2.2.1 Causes for Disruptions

In general disruptions can be divided into two major classes, the disruptions which occur when the density limit of the plasma is exceeded or disruptions at low q-values |71-78|. A further minor group of disruptions can be attributed to the current rise phase of the plasma discharge.

In terms of runaway-electron production density limit disruptions generate the highest fluxes of accelerated electrons. In the case of low-q disruptions the rate of current decay is lower which allows less electrons to be accelerated since the electric field is weaker. Current rise disruptions are less violent since here in most cases the stored energy has not yet reached its maximum value.

A schematic of the development of a density limit disruption is shown in Figure 2.4 |71|. The density limit above which disruptions may occur is approximately given for JET as |71|:

$$\bar{n} = 12 \cdot 10^{19} B_T / R q_c \ (m^{-3}) \qquad \text{[equ. 2.11]}$$

with B_T : toroidal magnetic field

R : major radius

q_c : cylindrical approximation for q:

$q_c = 2\pi a\ b\ B_T/\mu_o R I$

a,b : half width, half height of the plasma

μ_o : resistance of the plasma

I : plasma current

At the density limit the power which is radiated from the plasma equals the input power. The same effect occurs when debris from the first wall enters the plasma (so-called 'UFO's') and the radiated power suddenly increases due to impurities |79|. As a consequence the plasma forms a narrower channel that carries the current due to a contraction of the temperature profile |71|. This contraction generally allows for the successive destabilization of the m = 3, n = 1, and the m = 2, n = 1 tearing modes. These magnetic island modes rotate at frequencies between 1 and 10 kHz |70|. If, due to an increase of the poloidal field perturbation the m = 2 mode is brought to a stillstand ('mode-locking') a minor disruption occurs |73|. The position of this mode-locking is given by some arbitrary inhomogeneities, either in the magnetic field or in the symmetry of the inner vessel |70|. The minor disruption allows for an intensified interaction of plasma particles with the wall since the perturbed magnetic structure leads to an increased anomalous particle transport in radial direction. During this process the impurity influx from the most protruding first wall components into the plasma is increased. Usually the plasma then recovers briefly but further minor disruptions follow since stable conditions cannot be reached anymore. The time scale for this series of minor disruptions is 100-200 ms in JET |71|. Finally this sequence ends in a major disruption.

2.2.2 Development of a Major Disruption

The final major disruption which terminates a plasma discharge can be divided into a thermal energy quench phase and the subsequent current quench phase |80-85| during which the stored magnetic energy is dissipated.

The quench of the thermal energy happens in two steps |71|. First the plasma enters a further cycle of a minor disruption as described in section 2.2.1 but the plasma does not recover from this event. From soft x-ray measurements it can be deduced that the plasma at this stage has already lost about half of its thermal energy |79|. The final energy quench then proceeds more rapidly. Within 10-250 μs almost all thermal energy is lost to the walls. During this sequence the plasma is cooled down to temperatures between 5 - 10 eV |71,79| and the major part of the plasma ion population consists of impurity species which were released from the wall during the thermal quench. This is consistent with observed 10^3 fold increases of the carbon III line intensity and a $2 \cdot 10^2$ fold increase of the visible bremsstrahlung during disruptions |79|. The observed carbon radiation is a bulk effect showing the complete penetration of impurities into the core plasma.

The following current quench phase is initiated by the preceeding drastic change of the plasma parameters and a strongly increased resistance of the plasma as given by the Spitzer resistivity |86,87|:

$$\mu(t) \sim \frac{Z_e}{T_e^{3/2}} \qquad \text{[equ. 2.12]}$$

The increased resistance of the plasma causes a drastic increase in the input power, the rapid decay of the plasma current and a strong increase of the loop voltage |79|:

$$I^2\mu = \frac{d}{dt}\left(\frac{1}{2} L_i I^2\right) + I V_l \qquad \text{[equ. 2.13]}$$

with: μ : plasma resistance

L : internal inductance

V_l : toroidal loop voltage

The segmentation of the magnetic field supplies the energy to balance the increased plasma resistivity. However this increased input into the plasma is compensated by impurity radiation so that the plasma temperature does not recover and remains low. The decay of the plasma current happens on a very rapid time scale with values of up to 1 MA/ms |88|. This current decay rate and the corresponding rise of the loop voltage differ from device to device. Values from the literature are listed in table 2.1. However the current decay is not a linear process with time, especially it can change considerably if a part of the available energy is expended in the production of runaway-electrons.

2.3 Runaway-Electron Generation During Disruptions

2.3.1 Electric Field During Disruptions

The electric field E depends on the flux swing Φ which drives the current during the current decay phase |13|:

$$E = -\frac{1}{2\pi R}\,\frac{d\Phi}{dt} \qquad \text{[equ. 2.14]}$$

The flux change during the disruption may be either measured as loop voltage and be integrated or it may be calculated from the current step which occurs until the runaway-electron current is established:

$$\Phi = \int V_l\, dt \qquad \text{[equ. 2.15]}$$

$$V_l = -L\,\frac{dI}{dt} \qquad \text{[equ. 2.16]}$$

with: L : flux inductance of the plasma current

2.3.2 Acceleration and Energy of Runaway-Electrons

Depending on the ratio of the available electric field to the critical field E/E_c and the impurity content of the plasma the runaway rates may be approximated (see equ. 2.6). In the usual disruption cases it seems that only an exponentially small fraction of the available electrons will be accelerated.

The acceleration of electrons follows the relativistic equation of motion under the electric field E |5,13|:

$$\frac{d(\gamma m_o v)}{dt} = eE \qquad \text{or} \qquad \text{[equ. 2.17]}$$

$$\frac{d(\gamma\beta)}{dt} = \frac{e}{m_o c}\,\frac{1}{2\pi R}\,\frac{d\Delta\Phi}{dt} \qquad \text{[equ. 2.18]}$$

with

$$\beta = (\gamma^2 - 1)^{1/2}\,\gamma \qquad \text{[equ. 2.19]}$$

By integration the following expression can be obtained:

$$\gamma = \left\{1 + \left|\frac{e}{m_o c}\,\frac{\Delta\Phi}{2\pi R}\right|^2\right\}^{1/2} \qquad \text{[equ. 2.20]}$$

By replacing

$$\frac{e}{m_o c}\,\frac{\Delta\Phi}{2\pi R} = \frac{c}{m_o c^2}\,\frac{e\Delta\Phi}{2\pi R} = \frac{2.998\cdot 10^8\ [m/s]}{0.511\ \ 10^6\ [eV]}\,\frac{e\Delta\Phi\,[Vs]}{2\pi R[m]}$$

$$= 93.3/R\,[m]\ \Delta\Phi[Vs]$$

Thus for freefall acceleration γ becomes

$$\gamma = \left[1 + (93.3/R[m]\ \Delta\Phi[Vs])^2\right]^{1/2} \qquad \text{[equ. 2.21]}$$

For $\gamma \gg 1$ the runaway-electron energy can be approximated as

$$W = 47.7/R \cdot \Delta\Phi \qquad [MeV, m, Vs] \qquad \text{[equ. 2.22]}$$

Figure 2.5 shows v_o/c and W as function of the flux change.

However at high electron energies above 100 MeV effects of cyclotron radiation influence the acceleration process |13|. The cyclotron loss of an electron is given as |89|

$$U = 8.85 \cdot 10^{-32} W^4/R \quad [\text{[eV/revol., eV, m}] \qquad \text{[equ. 2.23]}$$

The resulting retarding force on the electron is |13|

$$\tilde{E} = 1.408 \cdot 10^{-32} W^4/R^2 \quad [\text{V/m}] \qquad \text{[equ. 2.24]}$$

Thus the equation of motion becomes

$$\frac{d(\gamma m_o v)}{dt} = -eE + \tilde{E} \qquad \text{or} \qquad \text{[equ. 2.25]}$$

$$\frac{d}{dt}(\gamma^2-1)^{1/2} = -\frac{eE}{m_o c} + \frac{1.408 \cdot 10^{-32}}{R^2} \frac{e}{m_o c} (m_o c^2)^4 (\gamma-1)^4 \qquad \text{[equ. 2.26]}$$

Figure 2.6 shows the results of an analytic solution for the case of rectangular voltage pulses and a major radius R = 3 m |13|.

About the distribution function of runaway-electrons high uncertainty exists. The assumption of a shifted Maxwellian distribution is suggested by Matsuoka et al. |90|:

$$f(v,t) = \left(\frac{m_o}{2\pi k T_e(t)}\right)^{3/2} \exp\left(-\frac{m_o (v - v_{th}(t))^2}{2kT(t)}\right) \qquad \text{[equ. 2.27]}$$

However there is no experimental evidence for the validity of this assumption.

2.4 Runaway-Electron Trajectories in Tokamaks

For the description of runaway-electron drift orbits the existence of an axisymmetric field is assumed. With regard to the runaway-electron phenomenon during disruptions this treatment is only qualitative because the magnetic field is subjected to segmentation processes in the course of disruptions.

The trajectories of runaway-electrons consist of a fast Lamor gyration around a guiding centre. This centre forms a drift surface as a result of the movement along helical field lines and the vertical drift [5,91,92]. The components of the guiding centre velocity are

$$\vec{v}_g \cong v_\theta \hat{e}_\theta + v_{\parallel} \hat{e}_\phi + (v_d + v_v) \hat{e}_z \qquad \text{[equ. 2.28]}$$

with

$$v_\theta = \frac{r v_{\parallel}}{qR} = v_{\parallel} \frac{B_p(r)}{B_T}$$

$$v_v = -v_{\parallel} \frac{B_v}{B_T}$$

$$v_d = \frac{1}{R} \left(v_{\parallel}^2 + \frac{1}{2} v_{\perp}^2 \right)$$

The notation of electric fields and velocities is shown schematically in Figure 2.7. The conversation of the angular momentum P_ϕ allows the formulation of the drift orbit displacement as function of the poloidal flux $\psi(r)$

$$P_\phi = \gamma m_o R v_\phi - \frac{e}{c} \psi(r) \qquad \text{[equ. 2.29]}$$

$$\psi(r) = \frac{2\pi R}{c} \int_0^r \frac{dr''}{r''} \int_0^{r''} r' dr' j(r') \qquad \text{[equ. 2.30]}$$

For a flat current profile this function simplifies to

$$\Psi(r) = \int_0^r B_p R \, dr = \frac{R_o I_r}{c \, r_L} \qquad \text{[equ. 2.31]}$$

with r_L : radius of the flat current profile

The radial outward shift d_γ of the runaway orbit can be described by

$$d_\gamma = r_L \frac{v_d}{v_\theta(r_L)} = \varrho_p \frac{r_L}{R_o} = \frac{r_L}{2} \frac{r_L}{R_o} \frac{I_A}{I} \qquad \text{[equ. 2.32]}$$

with ϱ_p : poloidal Larmor radius
I_A : Alfven current

$$I_A = \beta\gamma \, m_o c^3/e = 0.017\sqrt{\gamma^2-1} \quad [\text{MA}] \qquad \text{[equ. 2.33]}$$

The geometrical condition for orbits to intersect protruding wall parts (limiters) is:

$$r_{ci} + d_\gamma + d_p = r_L \qquad \text{[equ. 2.34]}$$

with r_{ci} : critical orbit radius leading to intersection with the limiters
d_p : shift of the current distribution with respect to the geometrical axis

and

$$\frac{I_A}{I} < 2A'\left(1 - \frac{r_{ci}}{r_L} - \frac{d_p}{r_L}\right) \qquad \text{[equ. 2.35]}$$

with A' : ratio of major and minor radii
$A' = R_o/r_1$

In the case of runaway-electron formation during a disruption the accelerating electrons would almost instantly be detached from the cold impure bulk plasma and form a beam component with radial displacement. Classically it then would be possible to derive a

maximum confinement time for runaway-electrons under stationery conditions |39|:

$$W = m_0 c^2 (\gamma - 1)$$

$$\gamma^2 - 1 < \frac{4}{0.017} I^2 \left(\frac{R_0}{r}\right)^2 \qquad [MA] \qquad \text{[equ. 2.36]}$$

$$\tau \approx \frac{2}{0.017} \frac{I m_0 c}{eE} \frac{R}{r} = \frac{R^2}{r_L} \frac{I}{V_l} \qquad [MA, m, V, s] \qquad \text{[equ. 2.37]}$$

However this confinement time exceeds the real confinement time of runaway-electrons in large tokamaks during a disruption by a factor of 10^2 ... 10^3 (...10^4). The reason for this behaviour lies in the rapid radial transport of particles during disruptions which is caused by the segmentation of the magnetic field structure. This deviation from the classical behaviour may macroscopically be described as anomalous diffusion in radial direction |93,94|. Then the diffusion coefficient D may be written as

$$\frac{1}{D} \frac{\delta f}{\delta t} = \frac{1}{r} \frac{\delta f}{\delta r} + \frac{\delta^2 f}{\delta r^2} \qquad \text{[equ. 2.38]}$$

The mean confinement time for runaway-electrons is therefore

$$\tau_R = \frac{r^2}{4D} \qquad \text{[equ. 2.39]}$$

This implies that runaway-electrons circulating in the periphery of the runaway beam would be scraped off at first wall structures (limiters) on the outboard side of the tokamak (equ. 2.34). Since the outward shift increases with electron energy, the higher energy electron part of the runaway distribution is scraped off preferentially.

Because of their high energy the scrape-off length of the electrons is very short and the angle of incidence on the material surface is very small.

In the final stage of the current quench phase the residual plasma may move rapidly towards the inner column or the divertor plates of the tokamak when the destruction of the vertical field cannot follow the current decay of the plasma adequately. This process is especially pronounced in machines which operate with highly elongated plasmas. During this phase then the part of the runaway-electrons of lower energy which are less displaced and thus have not been scraped off beforehand are driven towards the divertor or the inner column where very violent interaction with the plasma facing material may occur.

3. Runaway-Electron - Materials Interaction

3.1 Interaction of High Energy Electrons with Materials

With regard to the response of materials to runaway-electron impact the deposition of thermal energy in the material is the most important effect. Sudden temperature excursions may cause serious damage to materials like evaporation, melting and fracture. For an understanding of the specific energy deposition under runaway-electron impact the physical interaction processes will be explained.

The predominant interaction processes when an electron passes through matter are |95-103|:

1. Bremsstrahlung |104-106| emission in which an $e^{\pm}$ radiates a photon in the electric field of a nucleus;
2. Pair-production |107,108|, in which a photon materializes into an electron-positron pair in the electric field of a nucleus.

At energies in the range up to 100 MeV, depending on the material, the following processes for reducing the electron or photon energies are important:

3. Electron-electron collisions |109,110| (ionization), in which an incident electron elastically scatters from an atomic electron, resulting in two lower energy electrons;

4. Compton scattering |111|, in which photons elastically scatter from atomic electrons, transferring some of their energy to the electrons.

The interaction processes of a high energy electron with a material are shown schematically in Figure 3.1. The longitudinal development of the cascade or shower is characterized by the 'radiation length', X_o. At very high energies this is the distance which an electron must travel so that its energy is reduced by an average factor of e^{-1} |97|:

$$X_o \cong 713\,A\,[Z(Z+1)\ln(183\,Z^{1/3})]^{-1} \quad [g/cm^2] \quad \text{[equ. 3.1]}$$

with: A: atomic weight
Z: atomic number

At very high energies, the distance a photon has to travel before pair production occurs is approximately 9/7 X_o |112|.

The number of electrons and photons in the shower increases exponentially with depth (as exp X/X_o), with additional electrons and photons being produced by pair production and bremsstrahlung |95|. This continues until the average particle energy is below the 'critical energy W_c' for that material. Below this energy

$$W_c = 800/(Z + 1.2) \quad \text{(MeV)} \quad \text{[equ. 3.2]}$$

ionization and Compton scattering play a dominant role in removing energy from the shower, and particle multiplication ceases |95|, Figure 3.2.

During the whole interaction process the electrons themselves do not release significant yields of secondary particles directly. The photons have much larger nuclear cross-sections for reactions as (γ,n), $(\gamma, 2n)$, (γ,p), (γ, pn) and (γ, α). To estimate the yields of secondary particles, it is necessary to know the photonuclear cross-section $\sigma(K)$ for particle production as a function of the photon energy K and the total length L of material traversed by photons of each energy.

The differential track length dL/dK for the electrons of high energy can be given approximately for very thin targets as |97|:

$$\frac{d\tilde{L}}{dK} \cong \frac{1}{2} X^2 X_o^{-1} K^{-1} \qquad \begin{cases} X \ll X_o \\ K < W_o \\ W_o > W_c \end{cases} \qquad \text{[equ. 3.3]}$$

The determination of photon track lengths in thick targets is more difficult. The most accurate treatment can be performed with Monte Carlo calculations which can accomodate all major physical processes (1 - 4) and can be performed also for complex target structures.

The energy transfer during the passage of a particle through a medium termed 'stopping power' |114| may for relativistic electrons be written as |96|:

$$-\frac{dW}{dX} = \frac{2\pi N_A e^4 \varrho Z}{m_o v^2 A} \left[\log \frac{m_o v^2 W}{2I^2(1-\beta^2)} - (2\sqrt{1-\beta^2} - 1 + \beta^2) \log 2 + 1 - \beta^2 + \frac{1}{8}(1-\sqrt{1-\beta^2})^2 \right] \qquad \text{[equ. 3.4]}$$

with N_A : Avogadro's number

A : atomic weight of the material

The above expression is a good approximation for the average rate of energy loss along the electron track providing:

1. The electron energy is large compared to the binding energies of the atomic electrons;

2. The energy is low enough, so that no correction due to the density effect is required, and

3. The energy lost by radiation is small, that means the electron energy is below the critical energy W_c (equ. 3.2).

Although this average value is quite accurate a more complete description of the passage of electrons through matter has to include the variation from the average. The variation in the amount of energy lost by successive particles through a medium is

known a straggling |115| whereas the variation in the particle paths through a matter is named scattering |112|. This includes the evaluation of angular deflections of particles due to collisions. Since these multiple processes of scattering and energy absorption are extremely complicated to evaluate Monte Carlo calculations are usually employed.

For the electron range in material a rough approximation may be given as |116|:

$$S = \frac{1}{\rho} (0.51W - 0.26) \quad [cm, g/cm^3, MeV] \qquad \text{[equ. 3.5]}$$

This range is based on the continuous slowing-down approximation and is thus the pathlength which an electron would travel if its rate of energy loss along the entire path were always equal to the mean rate for its energy.

3.2 Observations in Tokamaks

The main observation on runaway-electron processes in tokamaks are effects which result from interaction with materials. Thus the information on runaway-electron generation, their distribution and trajectories is very vage since it bases mainly on indirect conclusions which are drawn from these observations of interaction processes. As it has been mentioned in the previous section the main effects of runaway-electron materials interaction are the production of x-rays and photoneutrons, the photo activation of material and the occurence of obvious damage on materials which is caused by the thermal load. The main observations on runaway-electrons that can be done during the discharge are hard x-ray and photoneutron measurements whereas during shut-down phases of a machine the activation of plasma-facing components and the vessel can be measured and the damage to materials can be documented. However such analyses after periods of operation only very seldom allow that a local activation or a damage can definitely be ascribed to a single runaway-electron event.

3.2.1 Hard x-ray and Photoneutron Detection

During the interaction of high energy electrons with materials hard x-rays are released. The release of this radiation during tokamak discharges is described in |6,16,44,90,94|. The results of these studies are listed in Table 3.1.

ORMAK |44,94,117|: Runaways which formed during the breakdown phase of a discharge carried only a negligeable fraction of the current (< 1%) but they could gain high energies up to 12 MeV since they were continuously accelerated throughout the entire discharge (t_{dis} ca. 50 ms). Another series of experiments was performed where runaway acceleration was initiated by puffing of argon as impurity gas. The runaway-electrons contributed up to 60 % of the total current. Furtherly by a programmed shift of the plasma to decreasing major radius the coefficient of anomalous runaway diffusion to the outboard side was measured to be D = $10^2 \ldots 10^4$ cm^2/s.

PLT |118-120|: The production of hard x-rays following sawtooth oscillations of the plasma was measured. The confinement time of the runaway-electrons created during a sawtooth oscillation was determined to be 1...5 ms which is about 1/10 of the confinement time of thermal electrons. The dependence of the runaway-electron confinement time to the minor radius is ca. $t \sim r^2$. The maximum energy of runaway-electrons in PLT was measured to be 12 MeV.

DIII |61-63|: Slide-away discharges with runaway-electrons carrying large currents were observed.

DIVA |6|: Systematic measurements of the runaway population in the edge plasma of a divertor configuration were performed. For these measurement a small high Z probe was moved into the edge plasma and the x-rays emitted from the target were detected. A significant shift of the runaway-electron distribution to the outer radius was observed whereas the shift in the separatrix was

significantly smaller (shift on the outboard side ca. 3 x shift in the separatrix region).

Tokyo University |90|: A number of runaway-electron experiments were performed with a small tokamak. Under a loop voltage of 0.5 V/cm runaway currents of about 1/10 of the total current and energies $\leq$ 0.6 MeV were obtained on the time scale of 0.4 ms.

JT-60 |16,122|: Strong emission of hard x-rays was detected during shifts of the plasma position at the end of the current quench phase of disruptions. Figure 3.3 shows an example for a disruption discharge.

The observations on the release of photoneutrons are as follows:

HELIOTRON-E |123|: Typically 10^9 neutrons per pulse were measured which are produced by runaway-electrons of energies in the order of 10 MeV.

JET |10,13,124|: Fast measurements of the transient photoneutron production were performed. Figure 3.4 shows a plot of the photoneutron emission and the development of the plasma current during a disruption. The results indicate that the runaway-electrons can carry currents in the order of 1 MA and more during a disruption (plateau during the current decay phase). The neutron emission plot shows that during the 'stable current' phase a fairly constant rate of runaway-electrons drifts and diffuses outward and the interaction with the plasma facing material leads to the production of photoneutrons. Then at the final stage when the remaining plasma moves toward the inboard side the neutron yield rises strongly due to intense localized interaction with the material on the inboard column. During this phase localized transients in the release of photoneutrons were observed.

Three photoneutron detectors were located at different toroidal positions of the vessel (28.1°, 106.9°, 241.9°). The plot of the detector signals during a disruption, figure 3.5, indicates that highly localized neutron production occurs at positions were the

plasma facing material intersects with the runaway-electron orbit. However it is assumed that only about 20 % of the runaway-electrons produced during a disruption are drawn towards the inner column of the machine during the final collapse while the major part (ca. 80%) interacts with the material on the outboard side during the 'stable runaway-current' phase (figure 3.4). From the neutron yields measured during disruptions an estimate of the fraction of magnetic energy which is expanded into runaway-electron production was made |10,13|:
The neutron production during some 200 disruptions in JET allowed a fit of the neutrons produced with the current at which the plasma disrupted:

$$N = 2.10^{13} \cdot I^{2.6} \quad (I \text{ in MA}) \qquad \text{[equ. 3.6]}$$

Assuming a neutron yield as function of the electron energy W for a structure consisting of carbon tiles which cover an Inconel structure as

$$Y = 4.8 \cdot 10^{-5} W \quad \text{neutrons/electron (W in MeV)} \qquad \text{[equ. 3.7]}$$

the number of electrons per disruption may be given as:

$$N/Y = 4.2 \cdot 10^{17} I^{2.6}/W \quad \text{electrons/disruption (W in MeV)} \qquad \text{[equ. 3.8]}$$

The kinetic energy carried by the runaway-electrons in JET is:

$$NW/Y = 0.07 \cdot I^{2.6} \quad (\text{MJ, I in MA}) \qquad \text{[equ. 3.9]}$$

From this the fraction of the poloidal magnetic field energy that is available for the acceleration of runaway-electrons can be derived as

$$f = 2.9 \cdot 10^{-2} I^{0.6} \quad (I \text{ in MA}) \qquad \text{[equ. 3.10]}$$

3.2.2 Activation Measurements

Measurements of the photoactivation of plasma facing components were performed in several tokamaks. Depending on the plasma facing material and the material for the vessel structure isotopes as listed in table 3.2 were detected. These measurements are giving indication of the runaway-electron energies since the isotope formation of materials depends on whether the characteristic threshold for a nuclear reaction is exceeded or not. Table 3.3 lists the results of activation measurements on various machines.

TFR |125-129|: A poloidal molybdenum limiter was strongly activated in a zone around the equatorial outboard side. The same activation pattern was observed on a stainless steel limiter showing a gaussian distribution around the equatorial mid-plane with a half width, half maximum (HWHM) of 5.7°. From the activation pattern a scrape-off layer thickness of the runaway-electrons of 0.4 mm was derived. A space resolved measurement of the vacuum vessel activation showed in toroidal direction a variation which is increased between the toroidal field coils. This activation pattern is ascribed to the ripple losses of runaway-electrons. In addition a strong peak of the vessel activation was observed in the shadow of the outboard limiter. This effect occured because during runaway-electron impact hard x-rays are released in a tight forward cone which then hit the vessel wall and cause photonuclear reactions.

PLT |130-132|: From the activation pattern of an outboard stainless steel limiter a figure for the scrape-off length of runaway-electrons was derived to be 0.2 mm. The gaussian distribution of the activated products in dependence of the activation threshold for the respective photonuclear reaction was as follows around the equatorial outboard plane:

W = 8 MeV	HWHM = 5.3°
W = 10 MeV	HWHM = 5.0°
W = 12 MeV	HWHM = 4.5°
W = 20 MeV	HWHM = 3.3°

The activation of a tungsten limiter was found to be in reasonable agreement with the detected neutron flux.

JT-60 |16|: Graphite tiles of the bottom divertor which were fractured during operation were strongly activated with ^{7}Be having a threshold energy of 27 MeV. This may be taken as indication of a strong vertical movement of the plasma during disruptions so that runaway-electrons are scraped-off in the divertor (compare also figure 3.3). During limiter discharges however the plasma seems to mainly undergo a horizontal movement during disruptions. Thus ^{7}Be activation was also found on the graphite tiles of the centre column, especially on protruding tiles.

FT |134|: Here the gaussian activation pattern on the equatorial outboard plane looked as follows:

W = 8 MeV	HWHM = 9°
W = 20 MeV	HWHM = 7°

A slight shift of this pattern of 2-3 cm below the equatorial location was observed.

JET |124,133|: The isotope with the highest activation threshold (^{7}Be) was found predominantly on the outboard limiters. The HWHM of this roughly gaussian distributed pattern was about 6.5° in vertical direction. The areas of the center column which were mostly damaged by runaway electrons showed far less ^{7}Be activation. This indicates that orbits of the high energy electron fraction are stronger displaced to the outboard side where they are then scraped-off by the limiter. During the final

collapse of the plasma towards the center column of the machine only the lower energy fraction of the runaway-electrons is interacting with the material of the center column where severe damage was observed (cf. 3.2.3).

3.2.3 Material Damage in Tokamaks due to Runaway-electrons

An overview on the damage to plasma facing materials by runaway-electrons in tokamaks is given in table 3.4. In the following descriptions of the detected damage will be given.

TFR |128,129|: In TFR runaway-electron beams which were trapped by toroidal field ripples and forced to move on banana orbits pierced the stainless steel vacuum vessel. The high runaway-electron contents during the discharges were mainly caused by the low density operation of the device. On a poloidal limiter which consisted of molybdenum melting was found on the outboard segment in the equatorial plane which was obviously caused by runaway-electrons since the area was found to be highly activated (cf. 3.2.2). The same appearance of a melted spot was found on a stainless steel limiter. The main area of melting was found slightly below the equatorial plane (about 3 cm) which is coincident with an observed downward shift of the plasma during the discharges.

ORMAK |5|: A tungsten rod limiter was melted and fractured after about 10 discharges with moderate runway-electron content.

PLT |131,132|: Melting was observed on a poloidal stainless steel ring limiter on the equatorial outboard plane. Also highly localized melting and activation was observed on a tungsten limiter at the same position.

FT |134,135|: Melting and erosion was observed on mushroom segments of the stainless steel limiter on the outboard side with a slight offset downwards from the equatorial plane (about 4 cm).

TEXTOR [136]: A singular damage on a poloidal graphite limiter has been observed in the equatorial outboard plane. Figure 3.6 shows the damaged area. The geometry of the spot indicates that the scrape-off length of the runaway-electrons was well below 1 mm and that the material had been damaged to a depth of about 2 mm which indicates a volumetric energy deposition process in this region (cf. 4.4).

JT-60 [11,16,58,122]: The formation of melt layers of molybdenum and Inconel was observed together with a strong activation of the materials. A significant part of the damage can be attributed to runaway-electron impact during disruptions. Furtherly the fracture of several carbon tiles was caused by runaway-electrons (cf. 3.2.2).

JET [137-140]: The most serious damage to components occured during the initial operation phase when the inboard column of the vessel had been protected with Inconel tiles. About 50 local damages of about 10 cm^2 each with a depth of 1 mm where the metal was molten and the melt partially splashed had been detected. Under the heat load the armour tiles showed strong deformation. As a consequence of this damage the metal plates of the inner column were replaced by graphite and later partially by CFC tiles. After the replacement runaway-electron impact was observed on the edges of the most protruding tiles. Graphite tiles eroded, cracked and fractured under the heat fluxes by runaway-electrons whereas CFC tiles showed erosion only.
The Inconel rods which are used for the attachment of the tiles and which are located about 6 mm below the tile surface did not show signs of damage. As described in section 3.2.2 the carbon tiles on the inboard side of the vessel did not show strong ^7Be activation which implies that this damage was caused by runaway-electrons with energies below 27 MeV mainly.
On one CFC-tile the erosion damage can be attributed to a singular runaway-electron event. Deduced from the weight loss due to erosion the tile must have been subjected to a heat load in the order of 500 MJ/m^2.

On the limiters of the outboard side only one damage spot in the equatorial plane which can be attributed to runaway-electrons and which is similar in appearance to the damage observed in TEXTOR occured. However there is no clear indication on the heat load which is deposited by runaway-electrons in the equatorial outboard plane since the machine was always operated with carbon limiters which are far less sensitive against runaway-electron impact than metal limiters. Thus the damage on Inconel tiles which was observed on the inboard side during initial operation cannot be related to any information on the heat loads to the outboard side.

3.2.4 Runaway-Electron Processes during Disruptions Inferred from Observations in Tokamaks

Plasma electrons are accelerated by the electric field that builds up during the current quench phase of a disruption. If the electric field E is large enough compared to the critical field, substantial amounts of runaway-electrons can be produced. Within a few ms the runaway-electrons develop to a population able to carry large currents in the order of MA. With increasing energy of the runaway-electrons there will be a progressive loss of confinement due to shifts of the drift orbits and anomalous diffusion effects. Most of the high energy electrons will strike structures on the outboard side of the vessel in the equatorial plane. The remaining runaway-electrons which did not yet gain energies high enough to allow a significant offset may then be forced towards the divertor or the inner column when the decay of the vertical magnetic field cannot follow the collapsing plasma current and the remaining plasma is dumped onto the divertor or the inner column. The fraction of runaway-electrons hitting these locations compared to the fraction of runaway-electrons being scraped-off at the outboard side is in the order of 0.2 |13|. The energy of runaway-electrons in large present-day devices can be well above 30 MeV. The areas of interaction with plasma facing materials may be highly localized, in the order of cm^2 and depend strongly on the geometry and alignment of components.

Parts which are even slightly protruding will be the target for runaway-electron scrape-off. Zones of intense runaway-electron

interaction are near the equatorial outboard plane, the divertor and the center column of machines, especially for the case of highly elongated plasmas.

4. Experiment on High Energy Electron Materials Interaction

The experiments on high energy electron-materials interaction were carried out to provide an improved understanding of the runaway-electron processes in tokamaks.

The work was structured in groups with the aims to:

- determine the sensitivity of different materials to runaway-electron damage, section 4.2
- examine the energy deposition process of high energy electrons in materials by temperature measurements, section 4.3
- conduct a quantitative correlation experiment by simulating the deposition process of very high heat fluxes, section 4.4
- determine the sensitivity of component like layer structures to runaway-electron damage, section 4.5.

The facility used for the major part of the experiments was an electron linear accelerator described in section 4.1. The experiments were concerned with determining the processes of energy deposition by high energy electrons in materials, sections 4.2, 4.3 and 4.5.

In addition experiments were carried out by use of a hydrogen beam test stand, section 4.4. These experiments allowed the deposition of high heat fluxes (up to 40 MJ/m^2) and the determination of the materials response to high heat loads.

4.1 Description of the Electron Linear Accelerator

For the experiments on high energy electron-materials interaction the electron linear accelerator of the Radiation Laboratory of the Institute of Scientific and Industrial Research, Osaka University was used |141-144|. The following description is related to this installation. More general information on linear accelerators may be found in the literature |145-148|.

The machine used is a 35 MeV L-band electron linear accelerator with a general layout as shown in figure 4.1. The specifications of the machine are listed in table 4.1. During the experiments the system was operated in the steady state mode. For this operation the relevant system components are explained briefly.

The electron injector consists of an electron gun, grid pulser, and a high voltage power supply. The electron gun is a triode of coaxial structure which consists of an anode, an oxide cathode with curved surface and a mesh grid plated with platinum to prevent grid emission. The power supply, placed near the injector tank, applies the DC negative high voltage ($\leq$ 150 kV) to the grid. The grid pulse is applied to the cathode in order to suppress the grid bias and give positive potential to the grid. Then the electrons are accelerated to the anode and extracted from the anode aperture. The grid pulse for steady state mode operation is generated by a pulser with lengths of 0.1 to 2.5 μs.

The RF system consists of the RF source, transmission waveguides, and accelerating waveguides. Two RF frequencies (1300 MHz and 216 MHz) are generated by a master oscillator and fed to the amplifiers. The pulsed RF of 300 W supplied by the 1300 MHz amplifier then excites the klystron. The output power of the klystron is fed to the accelerating waveguide.

The power and the phase are adjustable with a power splitter and phase shifters. The klystron itself is a RF power source with a maximum output power of 20 MW. It is excited by a line type modulator which consists of a pulse forming network of 18 sections and a ceramic hydrogen thyratron. This thyratron is triggered by a pulse which is timed by the master trigger generator. The uniformity of the high voltage pulse supplied to the klystron can be minimized to be less than 0.5% during 4.5 μs. The amplitude stabilization of the klystron high voltage pulse is achieved by a pulse forming network charging regulator and high voltage stabilizer. A step-up pulse transformer having the winding ratio 1 to 10 generates pulses of about 200 kV which are applied to the klystron cathode.

Figure 4.2 shows the energy spectra of the electron beam for various lengths of beam pulses. In the experiments the steady state

mode of beam loading was used. In this mode the total energy gain V of the electron beam accelerated in the waveguide can be written as [141]:

$$V=(1-e^{-2\tau})^{1/2}\,(P_o\,r')^{1/2}-\frac{i\,r'\,l}{2}\,(1-\frac{2\tau e^{-2\tau}}{1-e^{-2\tau}}) \qquad \text{[equ. 4.1]}$$

with P_o: RF input power

τ : attenuation constant

l : length

r' : shunt impedance

For the specification of these parameters for the linac see table 4.1. The equation 4.1 shows that the energy gain of the electron beam depends on the square root of the RF input power P_o and decreases linearly with increasing current of the accelerated electron beam. Figure 4.3 shows the energy spectra of the beam (1.5 µs) operated in steady state mode.

For the focussing of the beam to reach a high flux density of electrons in the area of the beam window Q-double magnets were employed. The actual experiments were performed with beam parameters as shown in table 4.2.

4.2 Sensitivity of Materials to Damage by High Energy Electrons

4.2.1 Experimental Procedure

The general lay-out of these experiments was to subject samples of different materials to irradiation by a high energy electron beam [149-152]. The set-up for the experiments is shown in figure 4.4.

After preliminary experiments under atmospheric pressure a vacuum chamber was constructed to prevent beam spread and excessive oxidation of the specimen surfaces. The experimental set-up is shown in fig. 4.4. Most experiments were carried out under a vacuum of 10^{-1} Torr. After being coupled out of the linac tube guide by a 20 µm thick Ti-window the electron beam is passed directly into the target chamber through the same kind of 20 µm Ti-window. The linac tube guide and the experimental chamber had to be separated from each

other to prevent contamination of the electron beam facility. The specimen surfaces subjected to normal beam incidence were polished before the experiments.

The energy of the electron beam was adjusted to 20, 25 and 30 MeV. The irradiation parameters are listed in table 4.2.

For the experiments a variety of candidate materials for fusion applications was selected:

- Fine grain graphite EK 98 representing graphites which are widely used as plasma facing material |153-165|.
- SiC + 2% ALN as ceramic material |166-169|;
- Stainless steel which had been in use in fusion devices as limiter and wall material |170-172|;
- Refractory metals like molybdenum (TZM) and tungsten have been in use as limiter materials |173, 174| and are considered as back-up divertor material for next generation devices |175-183|.

Furthermore the density of these materials varies from 1.86 g/cm^3 to 19.1 g/cm^3 which is the most important parameter in terms of high energy electron-materials interaction. The physical properties of these materials are listed in Appendix 1.

The experiments on layer systems focus on compound systems of plasma facing low-Z and low density materials (e.g. graphite) attached to high-Z and high-density materials (e.g. stainless steel or molybdenum). Such compound systems are presently in the focus of development and investigation for application in steady state fusion devices since they allow the active heat removal from plasma facing components |184-193|.

For screening purposes and simplified post-experimental examination initial experiments on layer systems have been carried out with graphite plates of two, five and ten millimeter thickness which were fixed mechanically with nuts and bolts to 10 mm stainless steel and molybdenum bare plates. Beam incidence was normal to the graphite surface of the specimens.

For the further evaluation of the behaviour of layer systems specimens consisting of 5 and 10 mm thick layers of graphite brazed to sandwich substrates of molybdenum-copper-molybdenum were used. The braze for the bonding was Cu-Ag-Ti. A list of the samples subjected

to irradiation together with the irradiation parameters is given in Appendix 2.

After the decay of induced activity, post experimental examinations were carried out to determine damage caused by high energy electron impact. This included visual examination, metallography, optical light microscopy and SEM observations.

4.2.2 Experimental Results

Bulk Materials

Graphite: Graphite did not show any damage or structural change under irradiation of up to 7200 pulses at 20 MeV (= 64.8 kJ). Ceramographic cross sections of an unirradiated graphite and the material irradiated for 7200 pulses are shown in figure 4.5.

SiC + 2% AlN: Like graphite SiC + 2% AlN did not show any damage or structural change under irradiation up to 5400 pulses at 20 MeV (= 48.6 kJ).

Stainless Steel: This material reacts highly sensitive to electron irradiation with 20 MeV. At pulse numbers of 1200 stainless steel already shows initial grain growth. 3600 pulses are sufficient to cause the complete disappearance of the original grain structure (see figure 4.6). Under continued irradiation to 7200 pulses at 20 MeV melting occured. Figure 4.7 shows that the melt process took place in the volume of the material. Interdendritical cracks were found in the resolidified melt.

Molybdenum (TZM): The material is fairly resistant against 20 to 30 MeV irradiation. It shows initial grain growth after 5400 pulses and enhanced grain growth after 7200 pulses.

Tungsten: The irradiation of tungsten (20 and 30 MeV, 3600 pulses) leads to grain growth and the formation of a network of cracks which range deeply into the material (figure 4.8).

The results on the irradiation experiments on bulk materials are summarized in figure 4.9 which indicates the detected threshold values of the deposited energy for the occurance of structural changes and damage on the materials tested. The ranking indicates that graphite and SiC + 2% AlN are most insensitive against 20-30 MeV electron impact. Among the metals tested molybdenum is considerably more resistant than tungsten and stainless steel.

Model Layer Systems (Table 4.3)

Graphite Layers on Stainless Steel: Except for some discoloration under irradiation up to 7200 pulses the graphite layers did not show damage. A comparison of the results on layer systems with stainless steel substrates and the results on stainless steel bulk specimens does not show significant difference in the damage thresholds for the case of 2 mm and 5 mm thick graphite layers. Only a shielding of 10 mm thick graphite reduces the damage on stainless steel substrates compared to unshielded bulk stainless steel.

Graphite Layers on Molybdenum (TZM): The model layer systems of molybdenum covered by graphite were damaged after 5400 pulses at 20 MeV (see figure 4.10). The molybdenum substrates covered by 2 mm and 5 mm thick graphite were subjected to high temperature excursions. Molybdenum itself shows only (slight) grain growth, similar to the results on bulk molybdenum. The temperature of the substrate nevertheless exceeded the melting temperature of stainless steel thus causing melting of the attachment parts. As in the case of graphite/stainless steel structures, only a graphite layer of 10 mm thickness provides sufficient shielding of the molybdenum substrate to prevent any observable damage.

Graphite Layers brazed to Mo-Cu-Mo Substrate These systems consisted of a layer of 5 or 10 mm graphite brazed with Cu-Ag-Ti braze to molybdenum-copper-molybdenum sandwich substrates. Figure 4.11 shows the results of experiments on systems of 5 mm and 10 mm thick graphite brazed to compound substrates composed of a 2 mm molybdenum layer, a

2.5 mm thick copper layer, and a 2 mm thick molybdenum layer. After irradiation of both samples with 20 MeV during 7200 pulses the sample with a 5 mm thick graphite layer shows melting of the intermediate copper phase. In the location of the brazed zone between the 5 mm graphite layer and molybdenum small droplets are found which may originate from the Cu-Ag-Ti braze used for bonding. The specimen with a graphite layer thickness of 10 mm does not show visible damage. Thus also in the case of brazed layer systems, like in the case of the before mentioned model layer systems, a thickness of 10 mm graphite provides significant shielding compared to graphite layers of 5 mm thickness.

In both cases (5 mm and 10 mm graphite thickness) the brazed zone did not suffer disabling damage due to the heat load even though the braze had been remelted in the experiments (figures 4.12,4.13).

4.2.3 Discussion of the Experimental Results

Table 4.4 gives the values of range S and critical energy W derived from equs. 3.2 and 3.5 for materials tested in the runaway-electron simulation experiments.

With increasing beam energy and with increasing atomic number Z the portion of beam energy expended for photon production due to radiative collisions with atoms increases.

With regard to the thermal energy deposition the effects of the density ρ , and the atomic number Z are controversial. Low density and low Z_{av} lead to a favourable deposition of the thermal load in large material volumes but the major part of the kinetic energy is converted to thermal energy whereas in the high density, low Z_{av} case the fraction of the thermal energy is less but the heat load is deposited in far smaller volumes. Thus, with consideration of the physical material properties listed in Appendix 1 several statements on the experimental results can be made.

Due to the long range of electrons in graphite the thermal energy is deposited in a very large volume leading to moderate temperature excursions of the material. Under high energy electron impact this happens even if most of the kinetic electron energy is transformed into thermal energy compared to minor emission of bremsstrahlung. High thresholds for thermally induced damage like erosion and cracking lead to superior resistance of graphite

materials against runaway-electron impact in the energy range of 20 to 30 MeV.

The moderate density of SiC leads to an uncritical energy distribution in the bulk much like that in graphite. The heating rate in the material volume obviously stays below the limit of thermal shock damage occurence in the experiments.

Stainless steel reacts sensitive to high energy electron impact with grain growth and melting. Because of the high density of the material the energy deposition happens in rather small material volumes. Additionally poor thermal conductivity, a low threshold for twin formation and grain growth ($T < 0.7\ T_M$), as well as a low melting point lead to severe damage under high energy electron impact.

The molybdenum samples in the experiments underwent high thermal loads due to unfavourable distribution of the beam energy in small material volumes caused by the high density of molybdenum. The thermal induced damage in molybdenum was far less severe compared to stainless steel due to the high melting point and thus also a high threshold for grain growth initiation in molybdenum.

Although in the high-Z material tungsten the major part of the beam energy is expended into bremsstrahlung production, tungsten seems to undergo extensive temperature excursions due to the extremely short range of electrons which causes energy deposition in very small volumes. In addition part of the bremsstrahlung photons also contribute to the thermal loads by pair production processes. Thus under high energy electron impact on tungsten the temperature threshold for grain growth is easily exceeded. The coarse grain structure developing under these conditions is highly prone to microcracking when the ductile-brittle transformation temperature (DBTT) is passed during the cooling phase after the electron impact.

In layer systems of graphite covering metal substrates most of the kinetic energy of the electrons is deposited in the metal unless very thick graphite shielding is provided. This is caused by the long range of high energy electrons in graphite. Thus in the case of 2 mm and 5 mm graphite layers only a negligible fraction of the beam energy is deposited in the graphite layer whereas a layer of 10 mm graphite absorbs a portion of the beam energy to provide some reduction of the thermal load imposed on the substrate material. Like

the results on bulk materials stainless steel substrates are more sensitive to high energy electron impact than molybdenum substrates. Also in compound systems special attention has to be paid to the brazed interface. Braze materials with a comparatively low melting point such as copper base brazes may be subjected to melting and structural changes.

4.3 Measurements of the Temperature Rise during High-Energy Electron Irradiation

4.3.1 Experimental Procedure

The aim of these experiments was to determine the energy deposition process of high energy electrons in bulk materials by temperature measurements. The experimental set-up was very similar to that described in section 4.2.1. Cylindrical material samples of 20 mm diameter and 30 mm length (stainless steel SUS 316, copper, molybdenum) or 50 mm length (graphite) were used. Copper was selected as additional material because of its high potential as heat sink material for subsurface structures |194-197|. The samples were fitted with a PtRh-Pt thermocouple (ϕ1.6 mm). As shown in figure 4.14 the location of the temperature measurement was in the centre axis of the sample at a distance of 1/3 of the electron range as given in equ. 3.5. The parameters of the irradiation are also listed in figure 4.14.

For a first comparison of the experimental results simple one-dimensional numerical calculations of the energy deposition in the material were performed. A code by Tabata and Itoh |103| was used for these analyses. Materials data for the calculations were taken from Appendix 1.

4.3.2 Experimental Results

The results of the temperature measurements are shown in figures 4.15-4.18. The measured values of the temperature rise are shown in plots a. Plots b show the calculated temperature rise for the local energy deposition at the depth location of the thermocouple as derived from the results of the numerical calucations. These plots do not take thermal diffusion processes within the sample into account. Plots c indicate the temperature rise in the material for the case that the beam energy is uniformly deposited within the sample (9 J per pulse).

The temperature rise for graphite (figure 4.15) is comparatively slow. The initial gradient dT/dt comes close to the theoretical result. With continued irradiation the effects of thermal diffusion become significant and the further temperature rise is mainly characterized by a body heating-like process. The thermal conduction into the aluminium sample holder may have caused the developing discrepancy between the measured and the calculated body heating temperature rise.

In the case of stainless steel also the initial gradient of the measured temperature rise dT/dt is similar to the peaked energy deposition plot. The low thermal conductivity of the material leads to a slower approach of the measured temperature gradient to the gradient of the body heating process. The measurements on copper are very similar to the calculated results for body heating. This is due to the very high thermal diffusivity of copper which leads to a rapid homogenisation of the deposited electron energy over the volume of the material.

The measurements on molybdenum mark an intermediate case between the two calculated plots which can be attributed to the thermal diffusivity of this material being between the values for stainless steel and copper.

4.3.3 Discussion of the Experimental Results

The results of the measurements of the temperature rise in materials under 20 MeV electron irradiation are consistent with the structural changes and damage that was observed on irradiated bulk

materials (section 4.2). They however strongly indicate the qualitative nature of this kind of linear accelerator experiments. For allowing conclusions on the process of energy deposition by runaway-electrons in tokamaks only the initial gradient of the thermal response of the material can be taken as quantitative indication of the energy deposition. With the further progress of the irradiation effects of thermal diffusion become relevant and influence the further temperature rise strongly which is especially obvious for the temperature measurements in copper and graphite.

As a consequence of these results for a further quantitative approach on the issue of runaway-electron materials interaction two experimental lines were pursued:

- For a quantitatively relevant simulation of the deposition process of high amounts of energy in bulk materials of up to 40 MJ/m^2 high surface heat loads were applied with duration times that were long enough so that by thermal diffusion a realistic temperature profile could build up as it would occur in the material under runaway-electron impact in a tokamak. After the exposure of the material to the heat load the structural changes and the damage were documented (section 4.4).
- For a quantitative assessment on the interaction of runaway-electrons with carbon-metal layer systems a series of linear accelerator tests was performed with instrumented samples allowing to determine the effects of energy deposition in subsurface structures (section 4.5).

4.4 High Heat Flux Correlation Experiment

Since the limited power output of the electron linear accelerator does not allow a quantitative determination of the response of materials to runaway-electron impact, a correlation experiment was undertaken. The idea of this experiment was to apply a high surface heat load for a limited time to a carbon material [198-206]. During this time thermal conduction in the material would establish a temperature gradient from the surface into the material which corresponds to the temperature profile caused by runaway-electron impact into a material (see figure 4.19).

4.4.1 Analysis and Selection of the Energy Deposition Parameters

For the analysis of the energy deposition by runaway-electrons in a graphite Monte-Carlo calculations by use of the TIGER code were performed at Sandia National Laboratories |184,207,208|. This code is a coupled electron/photon transport code which combines microscopic photon transport with macroscopic random walk for electron transport. Cross-section data down to 1 keV are included. The results of one-dimensionsal calculations for 20 MeV and 50 MeV electron impact under 90^{o}, 5^{o} and 2^{o} angular incidence onto the graphite surface are shown in figures 4.20,4.21.

These results indicate an exponential decrease of the deposited energy with increasing depth for small angles of incidence. This means that in thick bulk graphite the structural changes will occur predominantly in regions near the surface of electron incidence since here the strongest thermal gradients will occur.

Since this thermal gradient established by runaway-electron impact on graphite is exponentially decreasing with depth, the same gradient can be established by thermal conduction in a material under surface heating. The differential equation for this heating process is given as |209,212|:

$$\frac{\delta}{\delta x}\left(k_t \frac{\delta T}{\delta x}\right) + \frac{\delta}{\delta y}\left(k_t \frac{\delta T}{\delta y}\right) + \frac{\delta}{\delta z}\left(k_t \frac{\delta T}{\delta z}\right) + \dot{q}(x,t) - \rho c_p \frac{\delta T}{\delta t} = 0 \quad \text{[equ. 4.2]}$$

T : temperature
k_t : thermal conductivity
$\dot{q}$: heat flux
ρ : density
c_p : specific heat
t : time
x, y, z : spatial coordinates

Assuming a semiinfinite body with starting temperature $T(x,t) = T(0,0)$ equ. 4.2 simplifies to

$$\frac{\delta^2 T(z,t)}{\delta z^2} + \frac{\dot{q}(z,t)}{k_t} - \frac{\rho c}{k_t} \frac{\delta T(z,t)}{\delta t} = 0 \qquad \text{[equ. 4.3]}$$

A finite difference program (DISRUP*A) |213-219| was used to calculate the temperature distribution in graphite under surface heat loads. A schematic of the program is shown in figure 4.22. Effects of radiation from the heated surface and non-equilibrium evaporation into a vacuum are included.

The thermal stresses which occur as a function of the temperature field in the material are evaluated in one-dimensional form |220|:

$$\sigma_{xx}=\sigma_{yy}=\frac{\alpha E}{1-\nu_p}\left[-T+\frac{1}{2h}\int_{-h}^{h}T\,dz'+\frac{3z'}{2h^3}\int_{-h}^{h}T\,z'\,dz'\right] \qquad \text{[equ. 4.4]}$$

σ_{xx}, σ_{yy} : Stresses

α : linear coefficient of thermal expansion

E_y: Young's modulus

ν_p : Poisson's number

h : $h = d/2$, half thickness of the plate

z' : depth coordinate with start in the plate centre : $z' = -h$ corresponds to $z = 0$

Data of the materials properties thermal conductivity, specific heat, and vapor pressure as derived from |219,221-223| were given as function of the temperature in parametric form as listed in Appendix 1.

Results of the calculations are shown in figures 4.23 to 4.25. For surface heat loads of 100 MW/m^2 and a duration of 200 ms surface temperatures of 3200°C to 3300°C are reached, depending on the thermal conductivity of the material (figure 4.23). The temperature distribution over the depth of a graphite (grade AXF-5Q) is shown in figure 4.20. The plot clearly shows the exponential shape which is very similar to the plot in figure 4.20 showing the energy deposition profile of 20 MeV electrons. The corresponding analysis of the thermal stresses occuring in the graphite AXF-5Q under a heat load of 100 MW/m^2 for durations of 80 ms and 200 ms are shown in figure 4.25. It is found that a field of very high compressive stresses builds up

during the first 80 ms which then remains fairly constant and migrates gradually with the heat into the material. At the same time the field of resulting tensile stresses within the material increases.

The aim of the experiments decribed in the following section is to apply such 'tailored' surface heat pulses which simulate the situation of runaway electron impact on graphite surfaces and to determine the structural response of the material.

4.4.2 Experimental Device and Test Procedure

For the performance of high heat flux experiments on plasma facing materials and full size first wall components the 10 MW Neutral Beam Injection Test Stand at the IPP Nagoya |224-228| had been modified. Figure 4.26 gives a schematic of the rebuilt test stand together with the machine specification.

The ion source of the test stand produces hydrogen beams of up to 120 keV, 75 A and 1 s pulse duration with a gaussian shaped profile of the beam power density. The elongation factor of the oval shaped beam in vertical direction is roughly 2 and depends on the beam condition applied in experiments. For material tests the deflection coils of the test stand are not in operation thus ions and neutrals are striking the material test pieces at a distance of about 5 m from the ion source. Either a set of test pieces or full size first wall components can be inserted into the vacuum vessel by a lock system without breaking the vacuum of the vessel (about 10^{-4} Pa). A drive mechanism allows the test pieces to be vertically positioned in the hydrogen beam. When operated without exposing test pieces to the beam, the beam is dumped into a calorimeter which provides data for the calibration of high heat flux experiments. The repetition rate of the test stand is three to five minutes depending on the power supply mode.

For the beam calibration the calorimeter of the NBI Test Stand vacuum vessel was used. In this calorimeter 25 shielded thermocouples indicate the temperature rise during the beam impact. The horizontal and vertical spacing of the thermocouples in the plane perpendicular to the beam is 50 mm. Since the copper shielding of the thermocouples leads to the measurement of the temperature in the volume of the

material, the recorded temperature is proportional to the energy dumped onto this unit. Thus at a preset pulse length the temperature rise indicates the power density of the beam in this location.

After the conditioning of the ion source was finished and the beam conditions for high heat flux experiments - as indicated by the calorimeter values - were satisfied, the test pieces were positioned in the beam line so that during the next pulse the beam could hit the samples with beam conditions similar to the previously calibrated pulse onto the calorimeter with a variation of the beam power of less than 5 % .

Figure 4.27 gives a calibration curve of the beam power density distribution of a pulse as it has been applied in the experiments. The peak power density of the pulses in the experiments varied between 94 and 105 MW/m^2 with pulse lengths between 158 and 321 ms. A list of the experiments is given in Appendix 2.

Materials used for these tests were several grades of commercial fine grain graphites as listed in Appendix 1,2. The size of the samples was 50 mm x 50 mm x 20 mm. After the exposure to the thermal load the samples were examined for structural changes and damage by light microscopy, SEM and metallographic crossection.

4.4.3 Experimental Results

A list of the experiments which were carried out on 11 different graphites is given in Appendix 2.

The material reaction to the incident heat flux can be described as erosion and crack formation. The thickness of the evaporated layers varied between 0 and 20 µm. However the evaporation which occured in the experiments cannot be correlated directly to the erosion which is to be expected in this context (section 5.4.1.2). A detailed description and analysis of the erosion results can be found at another place [198-203].

The cracks formed in a net-like structure on the material surfaces as shown in figure 4.28. The penetration of the cracks into the material was limited to depths smaller than 1.8 mm as shown in figure 4.29. The graphites showed a variation in their sensitivity to the formation of cracks depending on the material (figure 4.30). The most resistant graphite showed crack initiation under an energy deposition which was roughly twice as high as the energy deposition

which caused crack initiation on the weakest graphite. A detailed analysis of the structural changes and the material damage can be found in |205|. The results are in general consistency with results of other high heat flux experiments in similar parameter regimes |229-248|.

4.4.4 Discussion of the Experimental Results

Due to the thermal expansion of the heated material a field of compressive stresses builds up in the region near the heated surface according to equ. 4.4 and figure 4.25. If the compressive strength is exceeded the material fails by shear and forms cracks in the heated zone, figures 4.28, 4.29 |204|.

Since the temperature profiles which were induced in the materials during the experiments are very similar to the energy deposition profiles by 20-30 MeV runaway-electrons, threshold values for the formation of cracks can be defined:

The energy deposition by runaway-electrons in the plasma facing material at the final collapse of the disrupted plasma is assumed as an instantaneous process since the thermal diffusion length is short compared to the temperature profile within the material (section 3.2.4). In this case effects of thermal conduction can be neglected and the energy is locally expended in heating and at sufficiently high temperatures also in ablation of the material.
However since the threshold for crack formation on graphites is well below the temperatures at which evaporation dominates the incoming energy only contributes to the temperature rise of the material:

$$\Delta T = J \varrho / c_p \qquad \text{[equ. 4.5]}$$

On this basis the threshold for crack initiation as it has been determined in the experiment can be defined as energy deposited per unit surface area (MJ/m^2) (figure 4.30).

Crack initiation threshold under runaway-electron energy deposition:

lowest value:	ZXF-5Q: 14.2 MJ/m^2
highest value:	IG 110: 32.4 MJ/m^2

As a consequence for the application of graphites as plasma facing materials this implies that an energy deposition by runaway-electrons of 20-50 MeV above 14 MJ/m^2 may lead to the formation of cracks in a graphite and above 33 MJ/m^2 certainly cracking would occur. The results also indicate that the depth into which crack occurence was observed is limited to less than 2 mm. An increase of the deposited energy would result in slightly larger crack lengths which are however limited by the exponential shape of the runaway-electron energy deposition profile with depth. With regard to the behaviour of metals under similar conditions the electron energy would be deposited in much smaller volumes of the material, depending on its density. Thus phenomena like melting or crack formation as they had been observed in high heat flux experiments on stainless steel |249-259| or refractory metals |260-269| would already occur at considerably lower energy depositions than for graphite. In tokamak operation this has been observed at JET were material damage was significantly reduced by changing from Inconel to graphite wall protection (see section 3.2.3).

4.5 Measurements of the Sensitivity of Subsurface Structures to High Energy Electron Impact

Plasma facing structures in tokamaks which are close to the scrape-off layer or interact with it are most likely targets for runaway-electron impact. In next generation devices these structures would consist of a plasma facing material layer of carbon or another low-Z material which covers an actively cooled metal substrate made of copper, molybdenum or stainless steel. In case of runaway electron impact onto the low-Z, low density layer a part of the incoming energy might be absorbed by the high density metal substrate. This energy absorption of the substrate is depending on the electron impact conditions, the plasma facing material and its thickness, the metal material and the geometry.

For a quantitative determination of the heat load to a metal substrate which is to be expected under runaway-electron incidence the impact conditions by grazing electrons onto a carbon layer had

been simulated by an axisymmetric model for laboratory experiments, figure 4.31 |270|. Figure 4.32 compares the situation of runaway-electron incidence in a tokamak as derived from sections 2. and 3. with the incidence conditions in the linear accelerator experiments schematically.

4.5.1 Experimental Procedure

The results of the experiments decribed in sections 4.2 and 4.3 showed that for a quantitative approach in determining the energy deposition by high energy electrons in materials the initial temperature gradient may be used provided that thermal diffusion processes are suppressed as far as possible.

For the experiments radially symmetric samples were manufactured at Sandia National Laboratories, Albuquerque, USA (figure 4.31). These samples consist of graphite cylinders of 4, 7, 10, 13, 19 and 25 mm diameter which were inserted into a number of copper rings of slightly larger diameter. Thin ceramic rods were used as spacers between the graphite cylinder and the copper rings which at the same time provided thermal insulation between the graphite and the copper parts. In addition the copper rings were separated from each other by ceramic spacers. To each copper ring a thermocouple was attached to record the temperature rise during irradiation. The whole sample was carefully aligned in the beam line, so that beam incidence occured centrally on one of the front surfaces of the graphite cylinder. Thus the copper rings could only be heated by electrons and photons as a consequence of collisional scattering within the graphite material. The subdivision into eight copper rings allowed the determination of the energy deposition profile along the length of the graphite cylinder of 90 mm.

This subdivision into small copper rings which were thermally isolated from another and the thermal insulation of the copper rings from the graphite allowed measurements of the initial temperature gradient in the copper segments without disturbance by effects of thermal diffusion processes.

Before hitting the graphite cylinder of the sample the electron beam had to pass an aluminium blind with a 4 mm diameter hole by which the original beam diameter of about 5 mm was to be reduced to 4

mm diameter. For an evaluation of the influence of the blind thickness on the experimental results experiments were carried out with blind thicknesses of 20, 30 and 40 mm.

4.5.2 Experimental Results

The thermal response of the copper elements under electron irradiation of the graphite cylinders was taken to determine the energy deposited in the copper elements per electron:

$$J_{Cu} = \frac{\varrho\, c_p}{\tilde{F}\, C} \frac{dT}{dt} \qquad \text{[equ. 4.6]}$$

with

J_{Cu} = energy deposited in Cu per beam electron (MeV/(cm^3 e$^-$)),
ϱ = density of Cu (8.96 g/cm^3),
c_p = specific heat of copper (0.42 J/(gK)),
$\tilde{F}$ = beam electron flux (see table 4.2),
dT/dt = temperature gradient (K/s)

The results of the temperature measurements are shown in figures 4.33-4.37 for 20 and 30 MeV with blind thicknesses of 20 mm and for 30 MeV with blind thicknesses of 20, 30 and 40 mm. The measurement at 30 MeV and 20 mm blind thickness was performed twice to check the reproducibility of the measurements.

The experimental results show that a significant amount of the energy of the incident electrons is absorbed by the copper, although beam electrons did not hit the copper material directly.

The energy deposited in the copper rings is strongly dependent on the position along the graphite cylinder and being in most cases more intense near the irradiated surface. The diameter of the graphite cylinder has strong influence on the amount of deposited energy in the copper segments. The maximum amount of deposited energy in the

case of a 4 mm diameter graphite cylinder (20 MeV) is about six times the maximum amount of a 25 mm diameter graphite cylinder.

However the results show large scatter and are strongly dependent on the thickness of the blind used (section 4.5.3).

4.5.3 Discussion of the Experimental Results

The first measurements were obviously strongly influenced by additional heating effects caused by the aluminium blind of the set-up as shown in figure 4.31. Since the blind was employed to reduce the linac beam diameter of 5 mm to a 4 mm beam about 36 % of the accelerated electrons hit the blind. About 40 % of the electron energy then was converted into photons within the blind |116|.

Since the photon emission is strongly oriented in forward direction a fraction of the photons could hit the first copper rings of the set-up and deposit additional energy which was then included within the overall measurement of the temperature rise in the copper rings.

However in the case of a 40 mm blind most of the photon energy is dissipated within the blind so that the amount of additional photon energy to the copper rings is negligible. With respect to the objective of the experiment the most accurate result is obtained for 30 MeV electron energy and a blind thickness of 40 mm.

The experimental results show that scattering effects lead to a strong heating of the first copper segments in the case of the 4 mm diameter sample. With increasing diameter the peak in the deposition profile is shifted to greater depths which is consistent with the greater distance that has to be covered by collision and scattering processes. For diameters 19 and 25 mm the spatially peaked distribution ceases in favour of a more homogeneous heating.

For a further evaluation of this experiment with respect to the actual situation in tokamaks incidence conditions in a tokamak have to be compared to the experimental incidence conditions. Tokamak runaway-electrons hit first-wall components under grazing incidence on surface areas of about 5 to 50 cm^2. Thus also the volume distribution of the deposited energy profile is rather broad compared to the peaked deposition obtained in the experiments (fig 4.32).

Because of these differences average values of the deposited beam energy on copper were taken for the further evaluation of the experiments.

Since in the case of 30 MeV electron deposition almost all of the energy was deposited within the first 60 mm of the sample, this distance was taken to determine the average deposited energy. The results obtained by use of average values are closer to the real runaway-electron impact condition than those which would employ directly the peak deposition values of the experiments because in the tokamak situation a broad volume energy deposition distribution occurs (figure 4.32).

These average values were compared to a graphite reference thickness D which was derived from the cylindrical sample geometry as follows:

$$D = \frac{d_s - d_b/2}{2} \qquad \text{[equ. 4.7]}$$

where d_s is the diameter of the graphite cylinder and d_b is the diameter of the electron beam.

The results of this evaluation are shown in fig. 4.38. From this figure the influence of the graphite thickness on the shielding of a copper substrate from runaway-electron heating can be derived. It is found that the deposited energy in copper base structures is roughly reciprocal to the thickness of the carbon material layer by which the metal is covered:

$$\overline{J}_{Cu} \cong K \frac{1}{D^{1.15}} \qquad \text{(in MeV/cm}^3\text{, D in cm)} \quad \text{[equ. 4.8]}$$

For all experiments a similar dependence was found which only differs in the value of the constant K (K = 0.4-0.8). No remarkable difference in the averaged energy deposition between 20 and 30 MeV electron impact was observed.

For a first assessment of the response of subsurface structures of plasma facing components equ. 4.8 is correlated to the results of a Monte Carlo computation shown in fig. 4.39 |271|: This

computation shows for 5^0 electron incidence an energy deposition in the subsurface molybdenum of 9 MeV/cm. In this case the molybdenum is covered by a graphite layer of 1 cm. Assuming that no major differences between the electron energy deposition in molybdenum (ϱ = 10.2 g/cm^3) and copper (ϱ = 8.96 g/cm^3) exist the relation for the dependence of the energy deposition in subsurface (copper) structures on the thickness of the surface layer, equ. 4.8 may be calibrated to a deposition of 9 MeV/cm at a surface layer thickness of 10 mm:

$$\tilde{J} \cong 9 \cdot \frac{1}{D^{1.15}} \quad [\mathrm{MeV/cm}] \qquad \text{[equ. 4.9]}$$

However this relation should serve only as a first orientation on the dependence of the energy deposition in copper and molybdenum on the thickness of the carbon surface layer.
The consequences of the thermal and structural response of the materials will be discussed in section 5.4.2.

5. Discussion of the Implications for a Next Generation Device

As terms of reference for the following evaluation the parameter set for ITER (International Thermonuclear Experimental Reactor) as of October 1988 has been taken, table 5.1, figure 5.1|26|.Furtherly a current decay rate of 1-3 · 10^9 A/s during the current quench phase of a disruption at full power was assumed |272|.

5.1 Runaway-Electron Generation during Disruption

According to equ. 2.6 the critical field for electron runaway in ITER would be:

$$E_c = \frac{4\pi e^3 n_e \ln\Lambda}{m k T_e}$$

$$E_c \cong 2.7 \cdot 10^{-13} \frac{n_e \ln\Lambda}{k T_e}$$

with: $n_e = 10^{13}, 10^{14}$ /cm^3

kTe = 10 eV

$\ln \Lambda = 20$ |87|

E_c ($n_e = 10^{13}$/cm^3) = 5.4 V/cm

E_c ($n_e = 10^{14}$/cm^3) = 54 V/cm

The extreme condition for the complete suppression of electron runaway would be (equ. 2.7):

$$E_R = E_c \, (kT_e/m_0c^2) \approx 10^{-3} \text{ V/cm}$$

The electric field that is set up during the current quench phase of a disruption at full power can be calculated according to equs. 2.14-2.16:

$$V_l = -L \frac{dI}{dt}$$

$$\Delta\Phi = \int V_l \, dt$$

$$E = -\frac{1}{2\pi R} \frac{d\Phi}{dt}$$

with: L = 4.8 µH |10|

dI/dt = 1.10^9, $3 \cdot 10^9$ A/s

Δ I = 20 MA

$\Rightarrow$ t = 20, 7 ms

$\Delta\Phi$ = 96 Vs

dI/dt = $1 \cdot 10^9$ A/S: V_l = 4800 V, E = 1.32 V/cm

dI/dt = $3 \cdot 10^9$ A/S: V_l = 14.400 V, E = 3 .95 V/cm

Thus a ratio of the disruption electric field to the critical field for electron runaway in the order of

$$E/E_c = \frac{3.95}{5.4} = 0.73 \text{ for } \frac{dI}{dt} = 3 \cdot 10^9 \text{ A/S and } n_e = 10^{13}/\text{cm}^3$$

to

$$E/E_c = \frac{1.32}{54} = 0.024 \text{ for } \frac{dI}{dt} = 1 \cdot 10^9 \text{ A/S and } n_e = 10^{14}/\text{cm}^3.$$

For a value $Z_{eff} = 3$ due to carbon impurities according to equ. 2.10 and figure 2.3 electron runaway rates larger $\lambda = 10^{-5}$ occur at $E/E_c \geq$

0.06. Thus electron runaway under disruptions in ITER will be a most likely phenomenon to occur.

An estimate of the energy of runaway-electrons neglecting cyclotron losses gives (equ. 2.22):

$$W = \frac{47.7}{5.8} \cdot 96 \quad \text{MeV} = 789.5 \text{ MeV}$$

with $R = 5.8$ m

$\Delta\Phi = 96$ Vs

Cyclotron radiation exerts a retarding force on the electrons (equ. 2.24):

$$\tilde{E} = 1.408 \cdot 10^{-32} \frac{W^4}{5.8^2} \text{ V/m} \quad (W \text{ in eV})$$

Above 150 MeV this effect becomes significant in retarding further electron acceleration. At 500 MeV this force is 26 V/m which indicates a possible electron acceleration up to this order.

According to the scaling of JET (equ. 3.10) the fraction of the poloidal field energy that is spent into runaway-electron acceleration |10,13|

$$f = 2.9 \cdot 10^{-2} I_p^{0.6}$$

would be in the case of a 20 MA disruption in ITER

$$f = 17.5 \%$$

At a poloidal field energy of 600 MJ |273| this would correspond 60-120 MJ energy which can be potentially carried by runaway-electrons if one regards the uncertainty of the assumptions taken above.

5.2 Runaway-Electron Trajectories and Wall Contact

A very rough approximation for the displacement of runaway-electrons can be derived from equ. 2.32:

$$d_\gamma \approx \frac{r_L}{2} \frac{r_l}{R_o} \frac{I_A}{I}$$

Since due to the high electron energies the Alfven current is very high (equ. 2.33, up to 7 MA) and the runaway-electron fraction carries almost the whole current, $\frac{I_A}{I} \approx 1$, thus

$$d_\gamma \approx 0.34 \text{ m}$$

with: $r_L = 2\text{m}$

However the condition of equ. 2.35 is violated by $\frac{I_A}{I} \approx 1$ and the result is of more qualitative nature.

The implication of this result is that the high energy electron fraction will be quickly displaced to the outer radius and then scraped off at the most protruding sections of the first wall in the equatorial outboard plane.

Due to strong radial diffusion processes (equ. 2.38) also the electrons which were accelerated in the center of the cold plasma would be quickly transportated to radii where they would be scraped off. Assuming an anomalous diffusion coefficient for runaway electrons across the magnetic field which is undergoing segmentation of $D = 10\ m^2/s$ anomalous diffusion over a distance $r_L - d_\gamma = 1.7$ m would require about 290 ms which gives the order of magnitude of the possible confinement time of runaway-electrons.

Depending on the time of the final collapse of the residual plasma towards the inner column or the divertor plates a larger or smaller fraction of the runaway-electrons then would intersect

the plasma facing materials on the center column or divertor on a very short timescale.

By taking the trajectory offset value of $d_\gamma = 0.34$ m only the crossection through which runaway-electrons are carried would shrink from A_0 to A_1:

$$A_o = \pi r_o^2 = 12.57\ m^2 \longrightarrow A_1 = \pi (r_o - d_\gamma)^2 = 8.66\ m^2$$

Allowing 20 ms time for anomalous diffusion the crossection would shrink to

$$A_2 = \pi (r_o - d_\gamma - d_d)^2 = 4.60\ m^2$$

with d_d : diffusion length

$$d_d = \sqrt{D\,t} = 0.45\ m$$

Taken a homogeneous distribution of the runaway-electrons over the crossection A at the point of the final plasma collapse with

$$A_1 / A_0 = 0.68$$

and neglecting anomalous diffusion 32 % of the runaway-electron energy would have been deposited on wall at the equatorial outboard plane and 68 % on the inboard side. In the case of 20 ms anomalous diffusion the ratio would be

$$A_2 / A_0 = 0.37$$

with 63 % outboard side deposition and 37 % inboard side deposition of runaway-electron energy.
In JET a ratio of roughly 80 % outboard side deposition and 20 % inboard side deposition of runaway-electron energy has been observed [13]. Since the analysis performed above is more of qualitative nature it is assumed that between 50 and 80 % of the runaway-electron energy is deposited on the outboard side of the device.

5.3 Interaction with Plasma Facing Components

As derived in section 5.1 electrons which are accelerated during disruptions can carry energies in the order of 60-120 MJ. 50 to 80 % of this energy would be deposited on the outboard side of the machine due to the outward shift and anomalous diffusion effects of the runaway electrons. The incidence onto the material surfaces is grazing with very short scrape-off lengths (< 1 mm). Thus any slightly protruding part in the regions of runaway-electron incidence would be hit preferentially.

5.3.1 Electron Energy Deposition on the Equatorial Outboard Side

Mainly electrons of high energies (100...500 MeV) would be scraped off at the outboard side of the machine since their trajectories are significantly displaced to major radii. Thus during the current quench phase of plasma disruptions of a duration of presumably 20 to 100 ms between 30 and 100 MJ could be deposited on components at the outboard side of the device. Activation measurements of outboard components of tokamaks indicate a gaussian distribution of the incoming runaway-electron flux with following vertical spread (half width, half maximum, see section 3.2.2):

TFR:	HWHM:	5.7^{o}	
PLT:	HWHM:	5.3^{o}	(8 MeV)
		5^{o}	(10 MeV)
		4.5^{o}	(12 MeV)
		3.3^{o}	(20 MeV)
FT:	HWHM:	9^{o}	(8 MeV)
		7^{o}	(20 MeV)
JET:	HWHM:	6.5^{o}	(27 MeV)

Thus for an estimation of the maximum surface heat load to the outboard plane in ITER a HWHM of 5^{o} is assumed. The resulting peak heat load for a deposition of 30-100 MJ onto the outboard circumference

of 49 m would then be 1.6 - 5.3 MJ/m^2. However this deposition does not regard the extreme peaking in toroidal direction which has to be expected due to the very small scrape-off length of the high energy electrons. Measurements on TFR and PLT indicate scrape-off layer thicknesses of 0.2 - 0.4 mm. With regard to technically possible alignment accuracies this implies that peaking factors of 100 may occur.
For the design of a toroidal belt limiter in the equatorial outboard plane a HWHM of 7^{o} of the incoming runaway-electron flux is assumed. Thus the poloidal extend for a limiter onto which 95 % of the incoming electrons would impact is $\pm$ 0.575 m. Allowing for an additional offset of $\pm$ 0.20 m from the equatorial plane due to plasma shifts the poloidal extend would be about $\pm$ 0.8 m.

5.3.2 Electron Energy Deposition on the Divertor and/or the Inboard Side

Electrons of energies supposedly below 100 MeV would hit the divertor or the inboard wall of the device during shifts of the plasma position in the course of the current quench phase. Whether the divertor or the center column would be hit preferentially depends on the vertical and horizontal stability of the plasma. However there is strong indication that highly elongated divertor plasma configurations would be mainly instable on the vertical axis and thus the runaway-electrons would be scraped-off on the divertor surface. Energy depositions of 20-60 MJ would have to be expected.

Energy deposition on the divertor target:
It is assumed that the runaway-electrons which would be deposited in the divertor follow the magnetic flux surfaces quite closely and would be deposited in a very narrow channel at the position where the separatrix intersects with the divertor plate or very near to it. There is indication from JT-60 that the runaway electrons would impact on the electron side |16|. Since the main energy deposition would occur during a violent vertical movement of the plasma only one of the two divertor targets would be hit. Assuming a half width half maximum (HWHM) of the deposition channel of 0.05 m |273| and a

gaussian distribution of the deposited energy in toroidal direction the peak energy deposition for 20-60 MJ energy deposition would be 5-15 MJ/m^2 . The full width onto which 95 % of the energy would be dumped is 0.23 m on a circumference of $2\pi \cdot 5.8$ m = 36.4 m. With regard to the possible peaking of the energy deposition in toroidal direction also here the peaking factor is completely unknown but may be as high as 100.

Energy deposition on the centre column:
In the case of a mainly horizontal shift of the plasma towards the centre column 20-60 MJ energy could be deposited. Also here the extremely short scrape-off length may lead to very highly localized energy deposition because of unavoidable geometrical imperfections which cause deviations from perfect alignment with respect to the magnetic flux surfaces. The observed value from JET of energy densities up to 500 MJ/m^2 appears to be a realistic value for ITER, too. The location can be significantly offset from the equatorial plane in the case of a combined horizontal and vertical movement.

5.4 Materials Response to Runaway-Electron Impact and Threshold Values of the Energy Deposition

The following evaluation of the response of materials is based mainly on the experimental results as described in section 4. Under runaway-electron impact damage would have to be expected to occur on the plasma facing material and the underlying metal structures, esp. coolant channels.

5.4.1 Plasma Facing Material

In terms of sensitivity to damage under runaway-electron impact graphite has proven to be significantly less sensitive than refractory metals like tungsten or molybdenum (section 4.2). All metals tested showed grain growth, crack formation and/or melting

below 14 MJ/m^2, the threshold for crack initiation in the graphite with poorest thermal shock resistance.

5.4.1.1 Crack Formation/Fracture of Carbon Materials

The thresholds for crack formation on graphites as function of the deposited runaway-electron energy were determined to lie in between 14 and 33 MJ/m^2, depending on the graphite grade, for electrons below 50 MeV (section 4.4, figure 4.30).
During such an energy deposition cracks of about 1-2 mm length would be initiated. At higher deposited energies crack formation becomes stronger and may eventually cause the fracture of components. In addition cracks which were initiated by runaway-electron events can gradually grow to fracture |204,205|. For a further evaluation of this aspect an approach on fracture mechanics of graphite |274-283| and fatigue effects |284-292| would be needed.
The most favourable group of carbon materials for plasma facing applications in terms of thermal shock resistance under runaway-electron impact are carbon-carbon (C-C) composites. These materials show values of thermal shock resistance and thermal shock fracture toughness which are 10 to 20 times higher than those of graphites |293,294|. In high heat flux experiments as described in section 4.4 these materials did not show crack initiation or fracture |198,201|. Thus with regard to energy deposition during runaway-electron events as they are anticipated for ITER (section 5.3) the only materials which could potentially withstand heat loads of more than 100 MJ/m^2 without fracture are C-C composites.

5.4.1.2 Erosion of Carbon Materials

In terms of surface erosion of carbon materials under runaway-electron impact no significant differences between graphites and C-C composites are expected. Since large amounts of energy are distributed over the depth of the material effects of thermal diffusion during the duration of the impact may be neglected and an

instantaneous deposition may be assumed for the estimation of materials erosion under runaway-electron incidence.
The following estimate of the erosion thickness was derived from the results of the Monte Carlo calculations as shown in figures 4.20 and 4.21. From these plots a correlation between deposited surface energy and erosion thickness can be derived for 20 MeV and 50 MeV runaway-electron incidence. For this evaluation a heat of ablation for carbon was assumed as follows:

$$H' = (\Delta T_{gr}\, c_p + H\varrho/K) \qquad \text{[equ. 5.1]}$$

with: $\Delta T_{gr} = 3000^{o}C$ thermal excursion which is necessary to reach the regime of high vapour pressure (at 4000^{o} C about 10^5 Pa |295,296|)

$c_p = 2$ J/gK specific heat of graphite at 2000^{o} C

$H = 63000$ J/gK heat of sublimation for monatomic evaporation

$K = 6$ factor to reduce H; there is experimental evidence that erosion under pulsed heat loads significantly exceeds the analytic values if H = 63000 J/gK is used. Reasons for this behaviour of graphite are the erosion of multiple carbon species and of microscopic particles |297-304|.

From figures 4.20 and 4.21 the relation

$$\Delta\delta = f(W_{dep}) \qquad \text{[equ. 5.2]}$$

with $\Delta\delta$: depth into the material (mm)
W_{dep}: deposited runaway-electron energy (MeV/cm)

was taken. Then W_{dep} can be correlated to a corresponding surface energy J_{surf} which is needed for the erosion of material to a depth $\Delta\delta = f(W_{dep})$

$$J_{surf} = H'W/W_{dep} \qquad \text{[equ. 5.3]}$$

with W: electron energy (20 MeV or 50 MeV)

The erosion results for 20 and 50 MeV electron energy deposition are very similar, figures 5.2 and 5.3. It is assumed that for electron energies up to 100 MeV considerable differences in the amount of erosion would occur.

20 MeV electrons: $\Delta\delta(mm) \approx 0.0037\ J_{surf}\ (MJ/m^2) - 0.185$
$(J_{surf} \geq 84\ MJ/m^2)$ [equ. 5.4]

50 MeV electrons: $\Delta\delta(mm) \approx 0.0043\ J_{surf}\ (MJ/m^2) - 0.361$ [equ. 5.5]
$(J_{surf} \geq 84\ MJ/m^2)$

Thus with regard to the use of carbon materials in ITER severe surface erosion will occur at runaway-electron energy depositions in excess of 100 MJ/m^2.

5.4.2 Damage to Subsurface Metal Structures

On the basis of the measurements and the correlation of the experimental results to a numerical analysis as described in section 4.5 a first assessment on the sensitivity of subsurface metal structures, esp. divertor coolant channels which are covered by a plasma facing carbon layer under 20-30 MeV electron impact can be made.

Copper Substrate

Assuming a maximum allowable temperature excursion of small local areas of $\Delta T_{Cu} = 500^{o}C$ (e.g. $500^{o}C \rightarrow 1000^{o}C$) which would lead to melting of the braze material and thus perhaps to local failure of the brazed protection but not to melting of the copper structure the resulting enthalpy is:

$$H''_{Cu} = \Delta T_{Cu} \cdot c_p \cdot \rho = 1881.6\ J/cm^3 \qquad \text{[equ. 5.6]}$$

with: c_p = 0.42 J/gK (copper)

ϱ = 8.96 g/cm^3 (copper)

Using equ. 4.9 ,section 4.5.3, the surface energy deposition J_{surf} which is necessary to cause the thermal excursion ΔT as function of the protection material thickness D would be

$$J_{surf} = \frac{H''_{Cu} W D^{1.15}}{W_{dep}} = \frac{18.816 \cdot 20 \cdot D^{1.15}}{9} \qquad \left[\frac{MJ\ MeV\ cm}{m^2\ cm\ MeV}\right]$$

$$= 41.8 \cdot D^{1.15}\ (MJ/m^2 \text{ with D in cm}) \qquad \text{[equ. 5.7]}$$

The result which is an approximation for 20-30 MeV electron impact is shown in figure 5.4.

Molybdenum Substrate

For the use of a molybdenum substrate an allowable temperature excursion of ΔT_{Mo} = 1200° C was assumed (e.g. 800°C $\rightarrow$ 2000°C).

Thus the resulting enthalpy is

$$H''_{Mo} = \Delta T_{Mo} \cdot c_p \cdot \varrho = 4284\ J/cm^3$$

with c_p = 0.35 J/gK (molybdenum)

ϱ = 10.2 g/cm^3 (molybdenum)

The dependence of the surface energy deposition J_{surf} on the thickness of the protection material for a ΔT_{Mo} = 1200°C thermal excursion would be

$$J_{surf} = 95.2 \cdot D^{1.15}\ (MJ/m^2 \text{ with D in cm})$$

This result is also an approximation for 20-30 MeV electron impact and shown in figure 5.4.

For ITER these results indicate that runaway-electron energy deposition below 100 MJ/m^2 for molybdenum and below 50 MJ/m^2 for copper can already cause severe damage to divertor structures. These

results should be regarded as a first indication of the damage threshold values for energy deposition on the divertor by electrons below 100 MeV.

5.5 Summary of the Implications for a Next Generation Device

In a next generation device like ITER the electric field during the current quench phase of disruptions is supposedly large enough, so that

- the conditions for electron-runaway are fulfilled;
- electron energies of about 500 MeV can be reached;
- 10-20% of the poloidal magnetic field energy may be expended into runaway-electron production which corresponds to 60-120 MJ energy.

Of this energy

- 50-80 % may be deposited on the outboard side in the equatorial plane by high energy runaway-electrons (e.g. 100-500 MeV). The deposition profile in poloidal direction would be gaussian with a HWHM of 5-7 % (0.175-0.246 m) which corresponds to a poloidal peak deposition of 1.6 - 5.3 MJ/m^2. However the very short scrape-off length of runaway-electrons (< 1 mm) will lead to a very high peaking of these values in toroidal direction.

- 20-50 % may be deposited on the divertor surface or on the centre column supposedly by lower energy electrons ($\leq$ 100 MeV). On the divertor the energy would be deposited on a narrow toroidal channel (HWHM $\approx$ 0.05 m) which corresponds to a peak deposition of 5-15 MJ/m^2. However also here very high peaking factors have to be expected for the energy deposition in toroidal direction.

The material behaviour under runaway-electron impact is summarized in figure 5.5.

Protection Materials:

- Refractory metals as plasma facing materials would show crack formation and melting already under very moderate runaway-electron impact ($\leq$ 14 MJ/m^2).
- Graphites will show crack initiation at 14-33 MJ/m^2, depending on the graphite grade.
- C-C composites are supposed to be the only feasible materials in terms of thermal shock resistance under runaway-electron impact in the order of 100 MJ/m^2.
- Erosion of carbon materials becomes significant above 100 MJ/m^2. However the areas which are 'sufficiently' eroded and do not project anymore into the runaway-scrape-off layer will not be subjected to runaway-electron impact furtherly.

Subsurface Metal Structures:

Excessive thermal excursions of divertor coolant channels are to be expected for:

- copper alloys, 10 mm carbon protection: $\geq$ 42 MJ/m^2
  20 mm carbon protection: $\geq$ 93 MJ/m^2
- molybdenum alloys, 10 mm carbon protection: $\geq$ 95 MJ/m^2
  20 mm carbon protection: $\geq$ 211 MJ/m^2.

6. Conclusions

The conditions under which electron-runaway in tokamak plasmas can occur and the acceleration of electrons during the current quench phase of disruptions as well as their trajectories have been studied. A survey on the runaway-electron-materials interaction processes was performed to gain a practical understanding of possible consequences for tokamak operation.
Subsequently experiments to determine effects of high energy-electron-materials interaction were carried out using particle beam facilities, the Electron Linear Accelerator of the Institute of Scientific and Industrial Research of Osaka University and the 10 MW Neutral Beam Injection Test Stand of the Institute of Plasma Physics of Nagoya University. In these experiments metals (stainless steel, molybdenum, tungsten) showed grain growth, crack formation and/or melting already well below the threshold for crack initiation on graphite (14-33 MJ/m^2, depending on the graphite material). The process of volume deposition of electron energy in the material was studied with special emphasis on the possible effects to subsurface metal structures, especially divertor coolant channels which are covered towards the plasma by graphite. The shielding effect of the graphite layer, depending on the thickness was determined to be $S \sim D^{1.15}$ for grazing electron incidence on graphite surfaces.

On the basis of these experimental results a first assessment on runaway-electron effects in a next generation device like ITER was made:

- Runaway-electron generation to about 500 MeV, and 60-120 MJ energy carried by runaway-electrons during disruptions are anticipated.
- 50-80 % of the energy could be deposited on the outboard side, 20-50 % on the divertor surface or on the centre column.
- The scrape-off length of runaway-electrons is very small (< 1 mm) so that very high toroidal peaking factors of the energy deposition may occur.

- Refractory metals are infeasible as plasma facing materials in areas where runaway-electron impact is expected due to their low thresholds for crack-formation and melting. Graphites can be used up to about 30 MJ/m^2 energy deposition, C-C composites are the most preferable material group for plasma facing applications.
- Strong erosion will occur above 100 MJ/m^2 on carbon materials.
- Damage to metal coolant channels, esp. of the divertor is anticipated already below 100 MJ/m^2. Energy deposition on the divertor however may exceed this value several times.

References

1. E.P. Gorbunov, G.G. Dolgov-Savel'ev, V.S. Mukhovatov, V.S. Strelkov, N.A. Javlinskii, Sov. Phys.-Tech. Phys. 5 (1961) 1089

2. V.V. Matveev, A.D. Sokolov, L.A. Suchkova, Sov. Phys.-Tech. Phys. 8 (1963) 530

3. L.A. Artsimovich, Nucl. Fusion 12 (1972) 215

4. C.W. Barnes, J.D. Strachan, Phys. Fluids 26 (1983) 2668

5. H. Knoepfel, D.A. Spong, Nucl. Fusion 19 (1979) 785

6. S. Yamamoto, S. Sengoku, H. Kimura, Y. Shimomura, H. Maeda, H. Ohtsuka, K. Odajima, M. Nagami, N. Ueda, Nucl. Fusion 18 (1978) 205

7. HL-1 Tokamak Group in: Plasma Physics and Controlled Nuclear Fusion Research 1986 (IAEA, Vienna, 1987) 399

8. F. Alladio, E. Barbato, G. Bardotti, et al. in: Proc. 11th European Conf. on Controlled Fusion and Plasma Physics, Aachen (1983) 277

9. A.B. Berlizov, G.A. Bobrovskij, A.A. Bagdasarov et al. in: Proc. Plasma Physics and Controlled Nuclear Fusion Research 1976 (IAEA, Vienna, 1977) 3

10. O.N. Jarvis, G. Sadler, J.L. Thompson in: Proc. 15th Europ. Conf. on Controlled Fusion and Plasma Physics, Dubrovnik (1988)

11. H. Takatsu, T. Ando, M. Yamamoto, T. Arai, K. Kodama, M. Shimizu and the JT-60 Team; paper presented at 1st Int. Conf. on Fusion Nuclear Technology, Tokyo, April 10-15, 1988

12. O.J. Kwon, P.H. Diamond, F. Wagner, G. Fussmann and the ASDEX and NI-Teams, Institute for Fusion Studies, The University of Texas, Austin, DOE/ET-53088-316, IFSR 316 (1988)

13. O.N. Jarvis, G. Sadler, J.L. Thompson, Joint European Torus, JET-P (87) 50 (1987)

14. M. Huguet, J.A. Booth, G. Celentano, E. Deksnis, K.J. Dietz, P.H. Rebut, R. Shaw, K. Sonnenberg in: Proc. 11th Symp. on Fusion Engineering, Austin, Texas (1986) 1239

15. K.J. Dietz, J. Nucl. Mater. 155-157 (1988) 8

16. T. Ando, US-Japan Workshop P-132 on Evaluation of Graphite as First Wall Material and Development of First Wall Engineering for Next Large Fusion Devices, Tokyo, Feb. 3-4, 1989

17. M. Ulrickson, US-Japan Workshop P132 on Evaluation of Graphite as First Wall Material and Development of First Wall Engineering for Next Large Fusion Devices, Tokyo, Feb. 3-4, 1989

18. K. Tomabechi, paper presented at 1st Int. Symp. on Fusion Nuclear Technology, Tokyo, April 10-15, 1988

19. R. Toschi, paper presented at 1st Int. Symp. on Fusion Nuclear Technology, Tokyo, April 10-15, 1988

20. P.H. Rebut, K.J. Dietz, P.P. Lallia, paper presented at 8th Int. Conf. on Plasma Surface Interactions, Juelich, May 2-6, 1988

21. W.P. Eatherly, R.E. Clausing, R.A. Strehlow, C.R. Kennedy, P.K. Mioduszeswski, Oak Ridge National Laboratory, ORNL/TM-10280 (1987)

22. T. Yamashina, Ed.: Overall Characterizations of Graphites as Fusion First Wall Material and Evaluation of the Stability against Plasmas, Interim Report, Jan. 1989

23. H. Bolt, K. Koizlik, J. Linke, H. Nickel, G. Wolf; paper presented at 1st Int. Symp. on Fusion Nuclear Technology, Tokyo, April 10-15, 1988

24. J.M. Dupouy, M.F. Harrison, G. Vieider, C.H. Wu, J. Nucl. Mater. 141-143 (1986) 19

25. A. Miyahara, T. Tanabe, J. Nucl. Mater. 155-157 (1988) 49

26. ITER Concept Definition, ITER-1, Oct. 1988

27. S. Tamura and FER-Design Team; paper presented at 1st Int. Symp. on Fusion Nuclear Technology, Tokyo, April 10-15, 1988

28. M. Yamada, T. Kobayashi, H. Iida, F. Matsuoka, K. Ioki; paper presented at 1st Int. Symp. on Fusion Nuclear Technology, Tokyo, April 10-15, 1988

29. K. Mohri, S. Yamazaki, K. Satoh, T. Kobayashi; paper presented at 1st Int. Symp. on Fusion Nuclear Technology, Tokyo, April 10-15, 1988

30. E. Franconi, V. Rado, G. Simbolotti, V. Violante, G. Zampaglione, P.G. Avanzini, M. Brossa, D. Casali, M. Grattarola, M. Guerreschi, F. Rosatelli, paper presented at 1st Int. Symp. on Fusion Nuclear Technology, Tokyo, April 10-15, 1988

31. G. Vieider, A. Cardella, M. Chazalon, H. Gorenflo, B. Libin; paper presented at 1st Int. Symp. on Fusion Nuclear Technology, Tokyo, April 10-15, 1988

32. H.P. Furth in: E. Teller, Ed., Magnetic Confinement, Vol. 1, Part A (Academic Press, New York, 1981)

33. M.O. Hagler, M. Kristiansen, An Introduction to Controlled Nuclear Fusion (D.C. Heath and Co., Lexington, 1977)

34. L.A. Artsimovich, Controlled Thermonuclear Reactions (Oliver & Boyd, Edinburgh, 1964)

35. J. Raeder, K. Borass, R. Buende, W. Daenner, R. Klingelhoefer, L. Lengyel, F. Leuterer, M. Soell, Controlled Nuclear Fusion (John Wiley and Sons, Chichester, 1986)

36. T.J. Dolan, Fusion Research (Pergamon Press, New York, 1982)

37. D. Gresillon, T. Lehner, Eds.; La Fusion par Confinement Magnetique (Les Editions de Physique, Les Ulis, 1984)

38. V.V. Parail, O.P. Pogutse in: Reviews of Plasma Physics, M.A. Leontovich, Ed. (Consultants Bureau, New York, 1986)

39. T. Kawamura, H. Obayashi, A. Miyahara, Fusion Eng. Des. 8 + 9 (1989)

40. A. Cooper, D.W. Swain, F.B. Marcus, T. Kammash, Oak Ridge National Laboratory, ORNL/TM-5905 (1979)

41. N.T. Besedin, Y.K. Kuznetsov, J.M. Pankratov, Sov. J. Plasma Phys. 12 (1986) 436

42. C.S. Liu, Y.C. Mok, K. Papadopoulos, F. Engelmann, M. Bornatici, Phys. Rev. Letters 39 (1977) 701

43. B. Coppi, R. Pozzoli, Plasma Phys. 16 (1974) 223

44. D.W. Swain, S.J. Zweben, Nucl. Fusion 20 (1980) 711

45. J.W. Connor, R.J. Hastie, Nucl. Fusion 15 (1975) 415

46. R.M. Kulsrud, Y.-C. Sun, N.K. Winsor, H.A. Fallon, Phys. Rev. Letters 31 (1973) 690

47. M. Kruskal, J.B. Bernstein, Phys. Fluids 7 (1964) 407

48. A.V. Gurevich, Sov. Phys. JETP 12 (1961) 7

49. A.N. Lebedev, Sov. Phys. JETP 21 (1965) 931

50. A.V. Gurevich, Y.N. Zhivlyuk, Sov. Phys. JETP 22 (1966) 153

51. H. Dreicer, Phys. Rev. 115 (1959) 238

52. H. Dreicer, Phys. Rev. 117 (1960) 329

53. R.H. Cohen, Phys. Fluids 19 (1976) 239

54. K. Itami, G. Jahns, H. Yamada, K. McGuire, Princeton Plasma Physics Laboratory, PPPL-2260 (1985)

55. M. Ulrickson in: Proc. of the 'Japan - US Workshop on Plasma - Material Interaction/High Heat Flux Data Needs for the Next Step Ignition and Steady State Devices', IPP Nagoya, Jan. 26 - 30, 1987, IPPJ-AM-50 (1987) 475

56. P. Couture, K. McGuire, Princeton Plasma Physics Laboratory, PPPL-2380 (1986)

57. H. Nakamura, T. Ando, S. Niikura, T. Arai, M. Yamamoto, and the JT-60 Team, Japan Atomic Energy Research Institute, JAERI-M-86-173 (1986)

58. JT-60 Team, Japan Atomic Energy Research Institute, JAERI-M-87-009 (1987)

59. T. Ando, H. Takatsu, H. Nakamura, H. Yoshida, M. Yamamoto, K. Kodama, M. Suzuki, M. Shimizu, Proc. 12th Symp. on Fusion Engineering, Monterey, Oct. 12-16 (1987) 89

60. T. Ando, H. Takatsu, M. Yamamoto, K. Kodama, T. Arai, M. Suzuki, M. Shimizu, paper presented at 1st Int. Symp. on Fusion Nuclear Technology, Tokyo, April 10-15, 1988

61. T. Hino, J. DeGrassie, T.S. Taylor, G. Hopkins, C. Meyer, T.W. Petrie, C. Kahn, S. Ejima, and D-III Physics Group, J. Nucl. Mater. 121 (1984) 337

62. M. Nishikawa, H. Yokomizo, A. Kitsunezaki, T.E. McKelvey, T.S. Taylor, D. Doll, N. Brook, R. Seraydarian, J. Nucl. Mater. 128/129 (1984) 493

63. H. Yokomizo, M. Kasai, T. Taylor, R. Callis, D. Doll, H. Aikawa, A. Kitsunezaki, S. Konoshima, T. Matsuda, M. Nagami, M. Shimada, Nucl. Eng. Des./Fusion 1 (1984) 279

64. D.K. Owens, M. Ulrickson in: Proc. 14th Symp. on Fusion Technology, Avignon (1986) 61

65. E. Franconi, M. Barteri, G.M. Ingo, J. Nucl. Mater. 128/129 (1984) 481

66. S.A. Cohen, R. Budny, G.M. McCracken, M. Ulrickson, Nuclear Fusion 21 (1981) 233

67. R.J. Colchin, C.E. Bush, P.H. Edmonds, A.C. England, K.W. Hill, R.C. Isler, T.C. Jernigan, P.W. King, R.A. Langley, D.H. McNeill, M. Murakami, R.V. Neidigh, C.H. Neilson, J.E. Simpkins, J. Wilgen, J.C. DeBoo, K.H. Burell, E.S. Ensberg, J. Nucl. Mater. 76/77 (1978) 405

68. C. Ferro, E. Franconi, A. Neri, J. Nucl. Mater. 111/112 (1982) 573

69. The JET-Team, Plasma Phys. Contr. Fusion 29 (1987) 1219

70. M.A. Pick, G. Celentano, E. Deksnis, C. Froger, M. Hugon, M. Huguet, P.H. Rebut, R.Shaw, L. Sonnerup, P. Stott, paper presented at 15th Symp. on Fusion Technology, Utrecht, Sept.19-23, 1988

71. J.A. Wesson, R.D. Gill, M. Hugon et al., Joint European Torus JET-P (88) 44 (1988)

72. J.A. Wesson, A. Sykes, M.F. Turner, Culham Laboratories CLM-R 233 (1982)

73. B.B. Kadomtsev, Plasma Phys. Contr. Fusion 26 (1984) 217

74. A. Bondeson, M. Persson, Nucl. Fusion 28 (1988) 1887

75. K. Harafuji, T. Hayashi, T. Sato, Plasma Physics and Controlled Fusion 29 (1987) 1483

76. K.J. Hopcraft, A. Sykes, M.F. Turner, Nucl. Fusion 28 (1988) 1265

77. B.V. Waddell, B. Carreras, H.R. Hicks, J.A. Holmes, D.K. Lee, Phys. Rev. Lett. 41 (1978) 1386

78. A. Sykes, J.A. Wesson, Phys. Rev. Lett. 44 (1980) 1215

79. D.J. Ward, R.D. Gill, P.D. Morgan, J.A. Wesson, paper presented at 15th European Conf. on Controlled Fusion and Plasma Physics, Dubrovnik, May 16-20 1988

80. K. Lackner, H.P. Zehrfeldt, Eds., 'Current Disruption in Toroidal Devices', Max-Planck-Institut fuer Plasmaphysik, Garching, IPP III/51 (1979)

81. K.B. Axon, G.A. Baxter, J. Burt, W.H. M. Clark, G.M. McCracken, S.J. Fielding, R.D. Gill, D.H.J. Goodall, M. Hobby, J. Hugill, J.W. M. Paul, B.A. Powell, R. Prentice, G.W. Reid, P.E. Stott, D.D.R. Summers, A.J. Wootton, Plasma Physics and Controlled Nuclear Fusion Research (IAEA, Vienna 1987) 51

82. K.M. McGuire, D.C. Robinson, Phys. Rev. Lett. 44 (1980) 1666

83. TFR Group, Nucl. Fusion 25 (1985) 919

84. S. Tsuji, J. Nagayama, K. Miyamoto, K. Kawahata, N. Noda, S. Tanahashi, Nucl. Fusion 25 (1985) 305

85. D.E. Roberts, J.A.M. de Villiers, J.D. Fletcher, J.R. O'Mahony, A. Joel, Nucl. Fusion 26 (1986) 785

86. L. Spitzer, R. Haerm, Phys. Rev. 89 (1953) 977

87. L. Spitzer, Physics of Fully Ionized Gases (Interscience Publishers, New York, 1962)

88. M. Ulrickson in: Proc. US-Japan Workshop Q-86 on Plasma Materials Interaction/High Heat Flux Data Needs for the Next Step and Steady State Devices, Albuquerque, March 7-11, 1988, Sandia National Laboratories, SAND 88-1072 (1988) 376

89. M.S. Livingston, J.P. Blewitt, Particle Accelerators (Mc Graw - Hill, New York, 1962)

90. K. Matsuoka, K. Yamazaki, N. Inome, T. Uchida, Jap. J. Appl. Phys. 14 (1975) 667

91. K.L. Wong, Nucl. Fusion 22 (1982) 1528

92. N.T. Besedin, J.M. Pankratov, Conf. Abstracts, 12th Europ. Conf. on Controlled Fusion and Plasma Physics, Budapest, Sept. 2-6 (1985) 417

93. V.V. Parail, D.P. Pogutse, Nucl. Fusion 18 (1978) 1357

94. S.J. Zweben, D.W. Swain, H.H. Fleischmann, Nucl. Fusion 18 (1978) 1659

95. P.J. Gollon, IEEE Transactions on Nucl. Sci., NS-23 (1976) 1395

96. R.D. Birkhoff in: Handbuch der Physik, S. Fluegge, Ed., Vol. 34 (Springer, Berlin, 1958) 53

97. W.P. Swanson, Radiological Safety Aspects of the Operation of Electron Linear Accelerators, Technical Report Series No. 188 (IAEA, Vienna, 1979)

98. A. Zuppinger, G. Poretti, Eds., High-Energy Electrons (Springer, Berlin, 1965)

99. L.V. Spencer, Phys. Rev. 98 (1955) 1597

100. H. Kleinpoppen, M.R.C. Mc Dowell, Electronic and Photon Interactions with Atoms (Plenum, New York, 1976)

101. H.S.W. Massey, E.H.S. Burhop, Electronic and Ionic Impact Phenomena, Vol. 1 (Clarendon Press, Oxford 1969)

102. B.W. Schumacher in: Electron and Ion Beam Science and Technology, R. Bakish, Ed. (John Wiley, New York, 1965) 5

103. T. Tabata, R. Ito, Nucl. Sci. Eng. 53 (1974) 226

104. H.W. Koch, J.W. Motz, Rev. Mod. Phys. 31 (1959) 920

105. H. Bethe, E. Salpeter in: Handbuch der Physik, S. Fluegge, Ed., Vol. 35 (Springer, Berlin, 1957) 425

106. S.T. Stephenson in: Handbuch der Physik, S. Fluegge, Ed., Vol. 30 (Springer, Berlin, 1957) 337

107. C.D. Zerby, H.S. Moran, J. Appl. Phys. 34 (1963) 2445

108. R.G. Alsmiller, H.S. Moran, Nucl. Instr. Meth. 48 (1967) 109

109. B. Rossi, High Energy Particles (Prentice-Hall, Englewood Cliffs, 1952)

110. B. Rossi, Rev. Mod. Phys. 13 (1941) 240

111. R.D. Evans in: Handbuch der Physik, S. Fluegge, Ed. Vol. 34 (Springer, Berlin, 1958) 218

112. F. Rohrlich, B.C. Carlson, Phys. Rev. 93 (1954) 38

113. M. Barbier, Induced Radioactivity (North Holland, Amsterdam, 1969)

114. P.B. Pal, V.P. Varshney, D.K. Gupta, Nucl. Instr. Meth. B16 (1986) 1

115. R.R. Wilson, Phys. Rev. 84 (1951) 100

116. S. Schiller, U. Heisig, S. Panzer, Electron Beam Technology (John Wiley, New York, 1982)

117. H. Knoepfel, D.A. Spong, S.J. Zweben, Phys. Fluids 20 (1977) 511

118. C.W. Barnes, J.D. Strachan, Nucl. Fusion, 22 (1982) 1090

119. C.W. Barnes, J.D. Strachan, Princeton Plasma Physics Laboratory PPPL-1916 (1982)

120. C.W. Barnes, Ph.D. Thesis, Plasma Physics Laboratory, Princeton University (1981)

121. G. Sadler, O.N. Jarvis, private communication (1988)

122. M. Takatsu, J. Nucl. Mater. 155-157 (1988) 27

123. S. Besshou, O. Motojima, A. Jiyoshi, K. Uo, J. Nucl. Sci. Technol. 19 (1982) 821

124. G. Sadler, P. van Belle, O.N. Jarvis, G. Gorini, J. Kaellne, V. Merlo, M. Horne, Proc. 3rd JET Workshop on Neutron and Charged Particle Diagnostics, Joint European Torus, JET-IR (86) 04 (1986) 85

125. TFR Group, Nucl. Fusion 16 (1976) 473

126. P.H. Rebut, R. Dei-Cas, P. Ginot, J.P. Girard, M. Huguet, P. Lecoustey, P. Moriette, Z. Sledziewski, J. Tachon, A. Torossian, J. Nucl. Mater. 53 (1974) 16

127. F. Engelmann, A. Sestero, Plasma Physics and Controlled Fusion 1 (1975) 142

128. TFR Group, Phys. Letters, 60A (1977) 219

129. TFR Group, J. Nucl. Mater. 93 + 94 (1980) 203

130. J.D. Strachan, E.B. Meservey, W. Stodiek, R.A. Naumann, F. Girshik, Nucl. Fusion 17 (1977) 140

131. C.W. Barnes, J. M. Stavely, J.D. Strachan, Nucl. Fusion 21 (1981) 1469

132. J. Stavely, C.W. Barnes, R.E. Chrien, J.D. Strachan, Princeton Plasma Physics Laboratory, PPPL-1828 (1981)

133. G. Sadler, K.J. Dietz, private communication (1988)

134. G. Maddaluno, A. Vannucci, J. Nucl. Mater. 145-147 (1987) 697

135. C. Ferro, G. Maddaluno, J. Nucl. Mater. 128 + 129 (1984) 822

136. H. Hoven, K. Koizlik, J. Linke, H. Nickel, E. Wallura, W. Kohlhaas, paper presented at 8th Int. Conf. on Plasma Surface Interactions, Juelich, May 2-6, 1988

137. W.M. Lomer, J. Nucl. Mater. 133 + 134 (1985) 18

138. K.J. Dietz, K. Sonnenberg, E. Deksnis , R. Shaw in: Tokamak Start-up, H. Knoepfel, Ed. (Plenum Press, New York, 1985) 317

139. M.A. Pick, G. Celentano, E. Deksnis, K.J. Dietz, R. Shaw, K. Sonnenberg, M. Walravens, Proc. 12th Symp. on Fusion Engineering, Monterey, Oct. 12-16 (1987) 137

140. M.A. Pick in: Proc. US-Japan Workshop Q86 on Plasma Materials Interaction/ High Heat Flux Data Needs for the Next Step and Steady State Devices, Sandia National Laboratories Albuquerque, March 7-11, 1988, SAND88-1072 (1988) 69

141. H. Sakurai, M. Kawanishi, K. Hayashi, K. Tsumori, S. Takeda, Mem. Inst. Sci. Ind. Res., Osaka Univ. 38 (1981) 51

142. S. Takeda, K. Tsumori, N. Kimura, T. Yamamoto, T. Hori, T. Sawai, J. Ohkuma, S. Takamuku, T. Okada, K. Hayashi, M. Kawanishi, IEEE Transact. Nucl. Sci. NS-32 (1985) 3219

143. S. Takeda, M. Kawanishi, K. Hayashi, H. Sakurai, Nucl. Inst. Meth. 188 (1981) 1

144. T. Yamamoto, K. Oda, H. Kobayashi, M. Kawanishi, Nucl. Inst. Meth. 196 (1982) 469

145. P.M. Lapostolle, A.L. Septier, Ed.; Linear Accelerators (North Holland, Amsterdam, 1970)

146. H. Daniel, Beschleuniger (Teubner Stuttgart, 1974)

147. A.D. Vlasov, Theory of Linear Accelerators (Israel Program for Scientific Translations, Jerusalem, 1968)

148. A.P. Banford, The Transport of Charged Particle Beams (Spon, London, 1966)

149. H. Bolt, A. Miyahara, M. Miyake, T. Yamamoto, Institute of Plasma Physics, Nagoya University, IPPJ-841 (1987)

150. H. Bolt, A. Miyahara, M. Miyake, T. Yamamoto in: Proc. of the 'Japan-US Workshop on Plasma Material Interaction/High Heat Flux Data Needs for the Next Step Ignition and Steady State Devices', Institute of Plasma Physics, Nagoya University, Jan. 26-30, 1987, IPPJ-AM-50 (1987) 302

151. H. Bolt, Plasma 4 (1987) 1

152. H. Bolt, A. Miyahara, M. Miyake, T. Yamamoto, J. Nucl. Mater. 151 (1987) 48

153. TFR-Group, EURATOM-Report, EUR-CEA-875 (1977)

154. A.V. Vorobyev et al., Phyzica Plasmy 4 (1978) 982

155. H. Eubank et al., Proc. 7th IAEA Conf. on Plasma Physics and Controlled Nuclear Fusion Research, Vol. 1 (1979) 167

156. H.F. Dylla, M.A. Ulrickson, D.K. Owens, B. Heifetz, J. Nucl. Mater. 155-157 (1988) 15

157. K.H. Dippel, TEXTOR-Team and ALT-I Group, J. Nucl. Mater. 145-147 (1987) 3

158. W.R. Wampler, B.L. Doyle, A.E. Pontau, J. Nucl. Mater. 145-147 (1987) 353

159. R.S. Ritter, R.V. Budny, S.A. Cohen, J. Nucl. Mater. 145-147 (1987) 793

160. V.M. Chicherov, J. Nucl. Mater. 145-147 (1987) 117

161. D.G. Baratov, A.A. Vasilyev, V.N. Demyanenko, L.E. Demyanenko, S.N. Luzganov, S.V. Mirnov, T.B. Myalton, A.M. Runov, V.P. Fokin, J. Nucl. Mater. 145-147 (1987) 601

162. Y. Pavlov, D.P. Petrov, A.M. Solutsev, A.M. Stefanovski, A.L. Terebkov, A.F. Shcherbak, Sov. J. Plasma Physics 12 (1986) 739

163. P.M. Anderson, C.B. Baxi, E.E. Reis, J.P. Smith, P.D. Smith, paper presented at 1st Int. Symp. on Fusion Nuclear Technology, Tokyo, April 10-15, 1988

164. T. Ando, H. Takatsu, M. Yamamoto, K. Kodama, T. Arai, M. Suzuki, M. Shimizu, paper presented at 1st Int. Symp. on Fusion Nuclear Technology, Tokyo, April 10-15, 1988

165. H. Bolt, K. Koizlik, J. Linke, H. Nickel, G. Wolf, paper presented at 1st Int. Symp. on Fusion Nuclear Technology, Tokyo, April 10-15, 1988

166. L.H. Rovner, G.R. Hopkins, Nuclear Technology 29 (1976) 274

167. G.R. Hopkins, R.J. Price, Nucl. Eng. Des./Fusion 2 (1985) 111

168. H. Hoven, K. Koizlik, J. Linke, H. Nickel, E. Wallura, Berichte der Kernforschungsanlage Juelich, Juel-2002, Juelich (1985)

169. J. Linke, H. Hoven, K. Koizlik, H. Nickel, E. Wallura, J. Nucl. Mater. 155-157 (1988) 324

170. D. Hildebrandt, W. Hintze, B. Juettner, M. Laux, J. Lingertat, P. Pech, H.D. Reiner, H. Strusny, H. Wolff, J. Nucl. Mater. 93/94 (1980) 310

171. D. Hildebrandt, R. Flagmeyer, M. Laux, J. Lingertat, G. Oertel, P. Pech, H.-D. Reiner, S. Rogaschewsky, H. Strusny, F. Taeubner, G. Voigt, H. Wolff, Zentralinstitut fuer Elektronenphysik, ZIE-Preprint 80-4 (1980)

172. H. Bolt, H. Hoven, E. Kny, K. Koizlik, J. Linke, H. Nickel, E. Wallura, Berichte der Kernforschungsanlage Juelich, Juel-2086, Juelich (1987)

173. H. Wolff, H. Grote, A. Hermann, D. Hildebrandt, M. Laux, P. Pech, H.-D. Reiner, G. Ziegenhagen, V.M. Chicherov, S.A. Grashin, V. Kopecky, K. Jakubka, J. Nucl. Mater. 145-147 (1987) 671

174. I.I. Demidenko, V.M. Leonov, N.S. Lomino, V.D. Ovcharenko, V.G. Padalka, G.N. Polyakova, Sov. J. Plasma Phys. 10 (1984) 292

175. International Tokamak Reactor, Phase Two A, Part I, (IAEA, Vienna, 1983)

176. W.M. Stacey, M.A. Abdou, D.B. Montgomery, J.M. Rawls, J.A. Schmidt, T.E. Shannon, R.J. Thome, Nucl. Technol./Fusion 4 (1983) 202

177. F. Moons in: Tokamak Concept Innovations, International Atomic Energy Agency, IAEA-TECDOC-373 (1986) 103

178. T. Mizoguchi, S. Itoh in: ibid., p. 459

179. S.A. Moshkin, E.V. Mura'ev in: ibid., p. 474

180. S. Tsetkovsky in: Reports of the 3rd All-Union Conf. on Engineering Problems of Thermonuclear Reactors, Leningrad, June 20-22, 1984, p. 71

181. T. Tone, M. Seki, A. Minato, T. Horie, H. Kawamura, M. Ogawa, K. Fujimura, T. Takeda, K. Fukuya, H. Iida, M. Sugihara, H. Hashizume, K. Miya, S. Tsujimura, T. Yamamoto, S. Yamazaki, Y. Tanaka, N. Tachikawa, Y. Shibutani, A. Nagata, N. Miki, T. Watanabe, Japan Atomic Energy Research Institute, JAERI-M-86-176 (1986)

182. F. Engelmann, M. Chazalon, M.F.A. Harrison, E.S. Hotston, F. Moons, G. Vieider, J. Nucl. Mater. 145-147 (1987) 154

183. F. Engelmann, M. Chazalon, M.F.A. Harrison, E.S. Hotston, F. Moons, G. Vieider, EURATOM-Report, EU-FU/XII-80/86/55 (1986) Next European Torus, Status Report, EURATOM-Report, EU-FU/XII-80/86/51 (1986)

184. J.B. Whitley, J.A. Koski, R. Aymar in: Proc. 14th Symp. on Fusion Technology, Avignon (1986) 627

185. R. Aymar, C. Bon Mardion, P. Deschamps, C. Leloup, P. Libeyre, J. Vac. Sci. Technol. A5 (1987) 2263

186. J.A. Koski, F.M. Hosking, R.D. Watson, C.D. Croessmann, paper presented at 15th Symp. on Fusion Technology, Utrecht, Sept. 19-23, 1988

187. P. Chappuis, R. Aymar, P. Deschamps, M. Gabriel, J. Whitley, J. Koski, R. McGrath, R. Watson, paper presented at 15th Symp. on Fusion Technology, Utrecht, Sept 19-23, 1988

188. I. Smid, E. Kny, K. Koizlik, J. Linke, H. Nickel, E. Wallura, paper presented at 15th Symp. on Fusion Technology, Utrecht, Sept. 19-23, 1988

189. M. Nayama, M. Toyoda, H. Yamao, T. Uchikawa, H. Morita, S. Tsujimura, K. Ioki, M. Seki, T. Tone, M. Ogawa, M. Araki, in: Proc. 12th Symp. on Fusion Engineering, Monterey, Oct. 12-16 (1987) 129

190. K. Ioki, M. Nayama, S. Tsujimura, M. Seki, T. Horie, paper presented at 1st Symp. on Fusion Nuclear Technology, Tokyo, April 10-15, 1988

191. Y. Gotoh, H. Okamura, S. Itoh, T. Wada, Y. Karatsu, paper presented at 1st Int. Symp. on Fusion Nuclear Technology, Tokyo, April 10-15, 1988

192. F. Moons, R. Howard, G. Kneringer, R. Stickler, paper presented at 15th Symp. on Fusion Technology, Utrecht, Sept. 19-23, 1988

193. D. Besson, M. Coulon, R. Ruaux, R. Faron, J. Archer, D. Juge, B. Libin, F. Moons, paper presented at 15th Symp. on Fusion Technology, Utrecht, Sept. 19-23, 1988

194. H. Bousack, A.W. Baukloh, A. Paul in: Proc. 12th Symp. on Fusion Engineering, Monterey, Oct. 12-16 (1987)

195. H. Bousack, P.W. Phlippen, Kernforschungsanlage Juelich, Juel-2078 (1987)

196. M. Araki, M. Dairaku, T. Inoue, M. Komata, M. Kuriyama, S. Matsuda, M. Ogawa, Y. Ohara, M. Seki, K. Yokoyama, paper presented at 1st Int. Symp. on Fusion Nuclear Technology, Tokyo, April 10-15, 1988

197. C.D. Croessmann, J.B. Whitley, P. Chappuis, M. Lipa, P. Deschamps, paper presented at 15th Symp. on Fusion Technology, Utrecht, Sept. 19-23, 1988

198. H. Bolt, A. Miyahara, T. Kuroda, O. Kaneko, Y. Kubota, K. Sakurai, Inst. of Plasma Physics, Nagoya University, IPPJ-AM-51 (1987)

199. H. Bolt, C.D. Croessmann, A. Miyahara, T. Kuroda, Y. Oka, Inst. of Plasma Physics, Nagoya University, IPPJ-AM-53 (1987)

200. H. Bolt, A. Miyahara, T. Kuroda, Inst. of Plasma Physics, Nagoya University, IPPJ-842 (1987)

201. C.D. Croessmann, H. Bolt, A. Miyahara, T. Kuroda, Y. Oka, K. Sakurai, O. Kaneko, J. Nucl. Mater. 155-157 (1988) 278

202. H. Bolt, A. Miyahara, T. Kuroda, O. Kaneko, Y. Kubota, Y. Oka, K. Sakurai, J. Nucl. Mater. 158 (1988) 224

203. H. Bolt, C.D. Croessmann, A. Miyahara, T. Kuroda, Y. Oka, Fusion Eng. Des. 6 (1988) 167

204. H. Bolt, A. Miyahara, T. Kuroda, High Temp. - High Pressures, 20 (1988)

205. H. Bolt, T. Kuroda, A. Miyahara, H. Nickel, Kernforschungsanlage Juelich GmbH, Juel-2214 (1988)

206. H. Bolt, A. Miyahara, T. Kuroda, J. Linke, K. Koizlik, H. Nickel, C.D. Croessmann, J.B. Whitley, M. Seki, K. Fukaya, S. Yamazaki, paper presented at 1st Int. Symp. on Fusion Nuclear Technology, Tokyo, April 10-15 (1988)

207. R.T. McGrath in: Proc. Japan-US Workshop P-92 on Plasma material interaction/high heat flux data needs for next step ignition and steady state devices, Inst. of Plasma Physics, Nagoya University, Jan. 26-30, 1987, IPPJ-AM-50 (1987) 435

208. C.D. Croessmann, private communication (1987, 88)

209. J.P. Holman, Heat Transfer (McGraw Hill, New York, 1986)

210. H.W. Carslaw, J.C. Jaeger, Conduction of Heat in Solids (Clarendon, Oxford, 1959)

211. R. Behrisch, Nucl. Fusion 12 (1972) 695

212. R. Behrisch, J. Nucl. Mater. 93/94 (1980) 498

213. A.M. Hassanein, G.L. Kulcinski, W.G. Wolfer, J. Nucl. Mater. 103/104 (1981) 321

214. A.M. Hassanein, G.L. Kulcinski, W.G. Wolfer, J. Nucl. Mater. 111/112 (1982) 554

215. W.G. Wolfer, A.M. Hassanein, J. Nucl. Mater. 111/112 (1982) 560

216. A.M. Hassanein, Argonne National Laboratory, ANL/FP/TM-179 (1983)

217. A. Hassanein, J. Nucl. Mater. 122/123 (1984) 1453

218. A.M. Hassanein, G.L. Kulcinski, W.G. Wolfer, Nucl. Eng. Des./Fusion 1 (1984) 307

219. H. Nakamura, T. Hiraoka, A.M. Hassanein, G.L. Kulcinski, W.G. Wolfer, Japan Atomic Energy Research Institute, JAERI-M-83-058 (1983)

220. B.A. Boley, J.H. Weiner, Theory of Thermal Stresses (John Wiley, New York/London, 1960)

221. W. Delle, K. Koizlik, H. Nickel, Graphitische Werkstoffe fuer den Einsatz in Kernreaktoren, Teil II (Karl Thiemig, Muenchen, 1983)

222. Materials Handbook for Fusion Energy System (1986)

223. W. Delle, J. Linke, H. Nickel, E. Wallura, Spezielle Berichte der Kernforschungsanlage Juelich, Juel-Spez-401 (1987)

224. O. Kaneko, Y. Oka, K. Sakurai, T. Kuroda in: Proc. 10th Symp. on Fusion Engineering, Philadelphia, Pennsylvania (1983) 1502

225. Y. Oka, O. Kaneko, K. Sakurai, T. Kuroda, K. Hayashi, K. Masuda, Y. Sanada in: Proc. 13th Symp. on Fusion Technology, Varese (1984) 565

226. Y. Oka, O. Kaneko, K. Sakurai, T. Kuroda, Nucl. Eng. Des./Fusion 4 (1987) 387

227. T. Kuroda, O. Kaneko, K. Sakurai, Y. Oka, M. Shibui, J. Ohmori, Kakuyugo Kenkyu 54 (1985) 371

228. M. Shibui, J. Ohmori, S. Itoh, T. Sasaki, T. Kuroda, O. Kaneko, K. Sakurai, Y. Oka in: Proc. 11th Symp. on Fusion Engineering, Austin, Texas (1986) 877

229. C.D. Croessmann, G.L. Kulcinski, J.B. Whitley, Sandia National Laboratories, SAND86-0764 (1986)

230. C.D. Croessmann, N.B. Gilbertson, R.D. Watson, J.B. Whitley, Fusion Technology 15 (1989) 127

231. J. Bohdansky, C.D. Croessmann, J. Linke in: Proc. 14th Symp. on Fusion Technology, Avignon (1986) 1063

232. J. Bohdansky, C.D. Croessmann, J. Linke, J.M. McDonald, D.H. Morse, A.E. Pontau, R.D. Watson, J.B. Whitley, D.M. Goebel, Y. Hirooka, O. Leung, R.W. Conn, J. Roth, W. Ottenberger, H.E. Kotzlowski, Nucl. Instr. Meth. B23 (1987) 527

233. K. Ioki, M. Yamada, M. Nishikawa, T. Uchikawa, M. Onozuka, H. Yamao, Fusion Eng. Des. 5 (1987) 181

234. M. Onozuka, T. Uchikawa, M. Nayama, H. Yamao, K. Ioki, S. Niikura, H. Nakamura in: Proc. 11th Symp. on Fusion Engineering, Austin, Texas, USA (1986) 920

235. K. Ioki, M. Nishikawa, I.Tatsumi, T. Uchikawa, M. Fujiwara, J. Nucl. Sci. Technol. 22 (1985) 529

236. T. Uchikawa, M. Fujiwara, R. Nayama, T. Irie, M. Onozuka, M.Tomita, K. Ioki, M. Nishikawa, Fusion Technol. 8 (1985) 1748

237. H. Nakamura, S. Niikura, T. Uchikawa, M. Onozuka, H. Yamao, M. Nayama, K. Ioki, Japan Atomic Energy Research Institute, JAERI-M86-048 (1986)

238. D.L. Sevier, P.W. Trester, G. Hopkins, T.E. McKelvey, T.S. Taylor, J. Nucl. Mater. 103/104 (1981) 187

239. G.R. Hopkins, P.W. Trester, J.L. Kaae, J. Nucl. Mater. 128/129 (1984) 802

240. M. Shibui, J. Ohmori, T. Kuroda in: Proc. 14th Symp. on Fusion Technology, Avignon (1986) 1077

241. J.R. Easoz, R. Bajaj, J. Vac. Sci. Technol A3 (3) (1985) 1119

242. M. Ulrickson, J. Nucl. Mater. 85/86 (1979) 231

243. T. Horie, M. Seki, S. Yamazaki, K. Mohri, J. Ohmori, paper presented at 1st Int. Symp. on Fusion Nuclear Technology, Tokyo, April 10-15, 1988

244. S. Sato, K. Sato, Y. Imamura, Carbon 13 (1975) 309

245. S. Sato, Y. Imamura, K. Kawamata, H. Awaji, T. Oku, Nucl. Eng. Des. 61 (1980) 383

246. S. Sato, K. Kawamata, A. Kurumada. H. Ugachi, H. Awaji, R. Ishida, J. Nucl. Sci. Technol. 24 (1987) 547

247. S. Sato, A. Kurumada, K. Kawamata, T. Takizawa, K. Teruyama, paper presented at 15th Symp. on Fusion Technology Utrecht, Sept. 19-23, 1988

248. H. Shinno, M. Fujitsuka, Y. Yamauchi in: Overall characterizations of graphites as fusion first wall material and evaluation of the stability against plasmas, Interim Report, T. Yamashina, Ed. (1989) 166

249. J.R. Easoz, R. Bajaj in: Proc. 10th Symp. on Fusion Engineering, Philadelphia, Pennsylvania (1983) 1008

250. M. Seki, S. Yamazaki, A. Minato, T. Horie, Y. Tanaka, T. Tone, J. Fusion Energy 3 (3) (1986) 181

251. M. Seki, S. Yamazaki, A. Minato, T. Horie, Y. Tanaka, T. Tone, Fusion Eng. Des. 5 (1987) 215

252. K. Koizlik, H. Bolt, H. Hoven, J. Linke, H. Nickel, E. Wallura, Proc. 14th Symp. on Fusion Technology, Avignon (1986) 1057

253. C.D. Croessmann, G.L. Kulcinski, J.B. Whitley, J. Nucl. Mater. 128/129 (1984) 816

254. C.D. Croessmann, G.L. Kulcinski, J.B. Whitley, Proc. 11th Symp. on Fusion Engineering, Austin, Texas (1986) 884

255. C.D. Croessmann, G.L. Kulcinski, J.B. Whitley, Sandia National Laboratories, SAND86-2010- (1986)

256. S.T. Picraux, J.A. Knapp, M.J. Davis, J. Nucl. Mater. 120 (1984) 278

257. D. Quartaert, F. Brossa, P. Moretto, G. Rigon in: Proc. 13th Symp. on Fusion Technology, Varese (1984) 401

258. F. Brossa, E. Franconi, P. Moretto, G. Rigon, J. Nucl. Mater. 141-143 (1986) 210

259. F. Brossa, M. Cambini, D. Quataert, G. Rigon, P. Schiller, J. Nucl. Mater. 155-157 (1988) 412

260. M. Ulrickson, J. Vac. Sci. Technol. 18 (3) (1981) 1037

261. D.W. Doll, M. Ulrickson, J. Nucl. Mater. 85/86 (1979) 191

262. A. Tobin, J. Nucl. Mater. 85/86 (1979) 197

263. K. Nakamura, R. Yamada, M. Saidoh, Y. Murakami, J. Nucl. Mater. 111/112 (1982) 852

264. K. Nakamura, Japan Atomic Energy Research Institute, JAERI-M-82-026 (1982)

265. K. Nakamura, Japan Atomic Energy Research Institute, JAERI-M-85-089 (1985)

266. E. Kny, K. Koizlik, H. Nickel in: Proc. 14th Symp. on Fusion Technology, Avignon (1986) 1069

267. H. Bolt, K. Kiuchi, M. Araki, M. Seki, paper presented at 15th Symp. on Fusion Technology, Utrecht, Sept. 19-23, 1988

268. E. Kny, G. Kneringer, K. Koizlik, H. Nickel, paper presented at 1st Int. Symp. on Fusion Nuclear Technology, Tokyo, April 10-15, 1988

269. M. Shibui, J. Ohmori, Y. Sawada, T. Kuroda, O. Kaneko, K. Sakurai, Y. Oka, Fusion Eng. Des. 5 (1987) 197

270. H. Bolt, A. Miyahara, M. Miyake, T. Yamamoto, C.D. Croessmann, J. Nucl. Mater. 155-157 (1988) 256

271. A.J. Russo, C.D. Croessmann, R.T. McGrath, J.G. Watkins, K. Neimer, U.S. Contributions to the Homework for ITER, section I.4, Feb./March 1989

272. F. Engelmann, private communication (1988)

273. S.A. Cohen, private communication, ITER Divertor Workshop, Max-Planck-Institute for Plasma Physics, Garching, March 6-7 (1989)

274. W. Thiele, W. Delle, F. Schubert, H. Nickel, Kernforschungsanlage Juelich GmbH, Juel-1831 (1983)

275. M. Roedig, G. Kleist, H. Schuster, H. Nickel, Berichte der Kernforschungsanlage Juelich, Juel-1632 (1979)

276. H. Kakui, T. Oku, J. Nucl. Mater. 137 (1986) 124

277. T. Oku, S. Ishiyama, M. Eto, M. Inagaki, T. Hashida, H. Takahashi in: Proc. of the 'IAEA Meeting on Graphite Component Structural Design', Japan Atomic Energy Research Institute, Sept. 8-11, 1986 JAERI-M 86-192 (1987) 217

278. H. Cords, A. Djaloeis, G. Kleist, J. Moench, B. Oefinger, R. Zimmermann, Berichte der Kernforschungsanlage Juelich, Juel-1355 (1976)

279. M. Roedig, G. Kleist, H. Schiffers, H. Nickel in: Contributions for the Fifth London International Conference on Carbon and Graphite, Imperial College, London, Sept. 18-22, 1978, W. Delle, Ed., Juel-Conf-25 (1978) 70

280. T. Hayashida, T. Fukusawa, H. Takahashi, S. Ishiyama, T. Oku in: Proc. of the 'IAEA Meeting on Graphite Component Structural Design', Japan Atomic Energy Research Institute, Sept. 8-11, 1986, JAERI-M 86-192 (1987) 158

281. S. Sato, H. Awaji, H. Akuzawa, Carbon 16 (1978) 103

282. S. Sato, H. Awaji, K. Kawamata, A. Kurumada, T. Oku, Nucl. Eng. Des. 103 (1987) 291

283. M. Sakai, M. Inagaki in: Overall characterizations of graphites as first wall material and evaluation of the stability against plasmas, Interim Report, T. Yamashina, Ed., Hokkaido University (1989) 185

284. J.E. Brocklehurst in: Chemistry of Carbon, P.L. Walker, P.A. Thrower, Eds. Vol. 13th (Dekker, New York, 1977) 145

285. F.H. Ho, ASTM STP 791, II-598-614

286. H.L. Leichter, E. Robinson, J. Am. Cer. Soc. 53 (1970) 197

287. R.J. Price, Proc. 13 Conf. on Carbon, Irvine (1977) 244

288. R.J. Price, Carbon 16 (1987) 367

289. S. Ishiyama, T. Oku, Japan Atomic Energy Research Institute, JAERI-M-86-145 (1986)

290. P. Marshall, E.K. Priddle, Carbon 11 (1973) 541

291. H. Kakui, T. Oku, Japan Atomic Energy Research Institute JAERI-M-8808 (1980)

292. M. Sakai, M. Inagaki in: Overall Characterizations of Graphites as First Wall Material and Evaluation of the Stability against Plasmas, Interim Report, T. Yamashina, Ed., Hokkaido University (1989) 193

293. S. Sato, A. Kurumada, K. Kawamata, paper presented at US-Japan Workshop P132 on Graphite as First Wall Material and Development of First Wall Engineering for Next Large Fusion Devices, Tokyo, Feb. 3-4, 1989

294. W. Eatherly, paper presented at US-Japan Workshop P132 on Graphite as First Wall Material and Development of First Wall Engineering for Next Large Fusion Devices, Tokyo, Feb. 3-4, 1989

295. R.A. Langley, Ed., Data Compendium for Plasma Surface Interactions, Special Issue Nucl. Fusion (1984)

296. H.T. Klippel, paper presented at 1st Int. Symp. on Fusion Nuclear Technology, Tokyo, April 10-15, 1988

297. J.G.v.d. Laan, paper presented at 8th Int. Conf. on Plasma Surface Interactions, Juelich, May 2-6, 1988

298. J.G.v.d. Laan, paper presented at 15th Symp. on Fusion Technology, Utrecht, Sept. 19-23, 1988

299. Y.S. Touloukian, Ed.; Thermophysical properties of high temperature solid materials (Mac Millan, New York, 1967)

300. A. Greenville Whittaker, P. Kintner, Carbon 7 (1969) 414

301. P. Soo, R.E. Shroy, B. Rocks, D.G. Schweitzer, C. Sastre, Brookhaven Natl. Laboratory, BNL-NUREG-23717 (1979) 109

302. C.A. Klein, R.F. Menefee, B.D. Krenek, M.J. Berry, J. Appl. Phys. 61 (1987) 1701

303. J.T. Clarke, B.R. Fox, J. Chem. Phys. 51 (1969) 3231

304. H. Bolt, J.G.v.d. Laan, H.T. Klippel, European Contributions to the Homework for ITER, sections I.,II., Feb. 1989

Nomenclature

a	half width of an elogated plasma
A	atomic weight
A_i	areas of the poloidal plasma crossection
A'	R_o/r_1: ratio of major and minor radii
b	half height of an elongated plasma
B_T	toroidal magnetic field
B_p	poloidal magnetic field
c	velocity of light
c_p	specific heat
C	Coulomb number
d_b	beam diameter
d_d	diffusion length
d_p	shift of plasma
d_s	diameter of the graphite cylinder
d_γ	shift of the drift orbit
D	coefficient for anomalous diffusion
D	reference thickness for carbon layers
e	electron charge
E	electric field
E_c	critical electric field
E_y	Young's modulus
$\tilde{E}$	retarding force due to electron cyclotron losses
F	momentum of a test particle
$\tilde{F}$	beam electron flux
h	half thickness of a plate
H	heat of monatomic sublimation
H'	heat of ablation (graphite)

H''	enthalpy for temperature rise ΔT in a subsurface material
I	plasma current
I_A	Alfven current
J	energy
J_{Cu}	energy deposited in copper per beam electron
J_{surf}	energy deposited per unit surface area
$\tilde{J}$	energy deposited in subsurface copper or molybdenum per beam electron
k	Boltzmann constant
k_t	thermal conductivity
K	photon energy
K	constant for the determination of runaway rates (equs. 2.9,2.10)
K	correction constant for the heat of monatomic sublimation (equ. 5.1)
K	constant for the determination of the deposited energy in subsurface copper (equ. 4.8)
l	length
L	inductance
$\tilde{L}$	track length
m	mass
n	density
$\bar{n}$	density limit for disruption
N	number of neutrons produced by γ-n reactions
N_A	Avogadro's number
P_o	RF input power
P_ϕ	angular momentum
q	safety factor
$\dot{q}$	heat flux

r	minor radius
r_c	radius of magnetic or drift surface
r_{ci}	radius of the drift surface just intersecting outer limiter
r_L	limiter radius
r'	shunt impedance
R	major radius
s	electron range in a material
t	time
T	temperature
U	cyclotron loss of an electron
v	velocity
v_c	critical runaway velocity
v_{th}	electron thermal velocity
V	energy gain of electron beam accelerated in the waveguide
V_l	loop voltage
W	electron energy
W_c	critical energy for photon production
W_{dep}	deposited runaway-electron energy
x	spatial coordinate
X_o	radiation length
y	spatial coordinate
Y	neutron yield
z	spatial coordinate
z'	depth coordinate
Z	atomic number

α	coefficient of linear thermal expansion
β	relativistic velocity
γ	relativistic energy factor
δ	depth into the material, erosion depth
θ	spherical velocity coordinate (azimuthal angle in poloidal plane)
λ	electron runaway rate
μ	$= \cos \theta$
μ	resistivity of a plasma
ν_p	frequency of Coulomb collisions
ν	Poisson number
ξ	streaming parameters
ρ	density
ρ_p	poloidal Larmor radius
σ	cross-section for scattering of charged particles
σ_{ij}	stresses
τ	attenuation constant
τ_R	maximum runaway-electron confinement time
Φ	mean confinement time of runaway-electrons (diffusion)
Ψ	flux swing
$\Psi(r)$	spherical velocity coordinate
$\ln\Lambda$	poloidal magnetic flux function
	Coulomb logarithm

List of Tables

List of Figures

Figure 3.2: Critical energy W_c as a function of the atomic number Z (equ. 3.2) |97|.

Figure 3.3: Plots of current, hard x-ray and soft x-ray emission, and plasma position during a JT-60 discharge which was terminated by a disruption. Besides a radial shift the plasma performs strong vertical movements |16|.

Figure 3.4: Neutron emission and plasma current during a disruption in JET. The hesitation in the decay of the plasma current indicates that a runaway-electron current of > 1 MA has been established for a duration of more than 20 ms |13|.

Figure 3.5: Plots of the neutron emission during a disruption in JET. The detectors were located at different toroidal positions. The different relative amplitudes of the signals indicate that the neutrons originate from several distinct locations |13|.

Figure 3.6: Metallographic cross-section through a graphite limiter from TEXTOR. The limiter surface was hit by a runaway-electron event which caused cracking of the graphite on a surface area of several cm^2.

Figure 4.1: Layout of the electron linear accelerator of the Institute of Scientific and Industrial Research, Osaka University, which was used for experiments.

Figure 4.2: Beam energy spectra for different pulse lengths of the electron linear accelerator.

Figure 4.3: Typical energy spectra of the electron linear accelerator beam (1.5 µs) in the steady state mode. The current decreases with increasing beam energy.

Figure 4.4: Set-up for linear accelerator experiments. The beam is coupled into the target chamber via 20 µm thick Ti-foils. Beam incidence onto the specimen surface is perpendicular.

Figure 4.5: a) Cross-section of unirradiated graphite EK 98
b) Cross-section of a graphite EK 98 sample subjected to 7200 pulses, 20 MeV (64.8 kJ)

Figure 4.6: Cross-section of a stainless steel (SUS316) sample subjected to 3600 pulses, 20 MeV (32,4 kJ).

Figure 4.7: Stainless steel sample melted after 7200 pulses, 20 MeV (64.8 kJ)

Figure 4.8: Tungsten sample subjected to 3600 pulses, 30 MeV (38.9 kJ)
a) SEM image of the impact surface
b) Cross-section showing the crack penetration

Figure 4.9: Results of the irradiation tests on bulk materials at 20 and 30 MeV as function of the deposited energy.

Figure 4.10: Model layer systems after electron irradiation, 5400 pulses, 20 MeV (48.6 kJ). Graphite layers (left) have been attached to molybdenum substrates (right) by stainless steel nuts and bolts. Thermal excursions of the substrates occured in the case of thin graphite layers and caused melting of the attachment parts.

Figure 4.11: Brazed layer systems of graphite brazed Mo-Cu-Mo substrate after irradiation, 7200 pulses, 20 MeV (64.8 kJ). The specimen with a graphite layer of 5 mm thickness (left) underwent melting of the Cu-phase. The specimen with a 10 mm graphite layer (right) shows no damage.

Figure 4.12: Cross-section of the left side sample of fig. 4.11 showing the melted Cu-layer.

Figure 4.13: Cross-section of the right side sample of fig. 4.11. No damage occured in the interface region.

Figure 4.14: Set-up of experiments measuring the temperature rise in the materials under high energy electron irradiation.

Figure 4.15:
1. Energy deposition distribution of 20 MeV electrons in the semi-infinite absorber of graphite
2. Temperature rise within the graphite sample during 20 MeV electron irradiation

a) measured
b) no thermal diffusion, b') at energy peak
c) uniform body heating

Figure 4.16:
1. Energy deposition distribution of 20 MeV electrons in the semi-infinite absorber of stainless steel
2. Temperature rise within the stainless steel sample during 20 MeV electron irradiation

a) measured
b) no thermal diffusion
c) uniform body heating

Figure 4.17:
1. Energy deposition distribution of 20 MeV electrons in the semi-infinite absorber of copper.
2. Temperature rise within the copper sample during 20 MeV electron irradiation

a) measured
b) no thermal diffusion
c) uniform body heating

Figure 4.18:
1. Energy deposition distribution of 20 MeV electrons in the semi-infinite absorber of molybdenum
2. Temperature rise within molybdenum sample during 20 MeV electron irradiation

a) measured
b) no thermal diffusion
c) uniform body heating

Figure 4.19: Schematic of the high heat flux correlation experiment

Figure 4.20: Monte Carlo calculation of the energy deposition in carbon by 20 MeV electrons under different angles of incidence |208|.

Figure 4.21: Monte Carlo calculation of the energy deposition in carbon by 50 MeV electrons under different angles of incidence |208|.

Figure 4.22: Schematic of the numerical calculation procedure used for parameter determination for the high heat flux tests.

Figure 4.23: Thermal conductivity of different graphites as function of the temperature, the calculated maximum surface temperature and the thickness of the evaporated surface layer for a heat load of 200 MW/m^2 for 200 ms duration.

Figure 4.24: Temperature profiles in graphite AXF-5Q under a heat load of 100 MW/m^2 for various durations.

Figure 4.25: Numerically determined thermal stresses as function of the depth from the heated surface for a surface heat load of 100 MW/m^2 for the graphite AXF-5Q
a) stress distribution after 80 ms pulse length
b) stress distribution after 200 ms pulse length

Figure 4.26: Schematic and specification of the 10 MW NBI-test stand used for the experiments described in section 4.4. Materials samples can be driven in the beam line via a look system.

Figure 4.27: Spatial beam power density distribution for a beam pulse as applied in the experiments.

Figure 4.28: Crack pattern on the surface of an ultra fine grain graphite (ZXF-5Q) after a surface heat load of 97 MW/m^2 for 290 ms (28.1 MJ/m^2).

Figure 4.29: Cracks on the surface of an ultra fine grain graphite (ISO880) after a surface heat load of 93 MW/m^2 for 214 ms (19.9 MJ/m^2).

Figure 4.30: Results of the correlation experiment on crack formation in graphite.

Figure 4.31: Schematic of the experimental set-up as described in section 4.5

Figure 4.32: Comparison of the electron incidence situation in the experiments and in a tokamak.

Figure 4.33: Energy deposition profiles for different diameters of the graphite cylinder d_S (20 MeV, 20 mm blind).

Device	*Current [MA]*	*Decay Time [ms]*	*Decay Rate [MA/ms]*
ISX-B	0.1	1	0.1
Alcator A	0.18	0.7	0.26
T-10	0.3	5	0.06
PDX	0.3	1	0.3
PLT	0.35	1	0.35
Alcator C	0.5	1	0.5
JT-60			≤ 0.47
JET			≤ 0.85
TFTR			≤ 1

Table 2.1: Current quench phase parameters during disruptions in tokamaks

Device	*References*	*Runaway-Electron Energy*	*Loop Voltage*	*Observations*
ORMAK	44,94,117	mean 1.5-2 MeV max. 10-12 MeV	< 0.1 V/cm	• impurity induced runaway acceleration at low densities ($\sim 10^{13}$/cm^3) • $I_{runaway}/I_{peak} \sim 0.6$, $I_{runaway}$ <50 kA • breakdown formation: $I_{runaway}/I_{peak} \leq 0.01$ • experiments on anomalous runaway-electron diffusion: D = 10^2-10^4 cm/s
PLT	118-120	mean 1 MeV		• runaway during sawtooth oscillations: runaway electron confinement ~ 1/10 thermal electron confinement (t_{conf} ~ 1-5 ms) dependence $t_{conf} \sim r^2$
DIII	61-63			• slideaway discharges with high thermal loads to limiters
DIVA	6	0.1 MeV		• measurements with high Z-probe in plasma boundary: profile shift of runaway orbits in divertor discharges
(Tokyo University)	90	< 0.6 MeV	0.5 V/cm	• $I_{runaway} \sim 0.1$ I_{peak}

Table 3.1: Observations of runaway-electron produced hard x-rays in tokamaks

Device	*References*	*Material*	*Activation Pattern*	Distribution (vertical)	Remarks
TFR	125-129	Mo, stainless steel	• equatorial outboard plane • vacuum vessel activation	gaussian, HWHM = 5.7°	scrape-off length ~ 0.4 mm mainly due to ripple losses
PLT	130-132	W, stainless steel	• equatorial outboard plane	gaussian W = 8 MeV, HWHM = 5.3° W = 10 MeV, HWHM = 5.0° W = 12 MeV, HWHM = 4.5° W = 20 MeV, HWHM = 3.3°	scrape-off length ~ 0.2 mm
JT-60	16	graphite	^{7}Be on divertor tiles		especially fractured tiles were strongly activated
FT	134	stainless steel	equatorial outboard plane	W = 8 MeV, HWHM = 9° W = 20 MeV, HWHM = 7°	
JET	124,133	graphite	equatorial outboard plane, centre column (^{7}Be)	gaussian, HWHM ~ 6.5°	strong activation outboard, less activation of damaged centre column tiles

Table 3.2: Observations of photoneutron production in tokamaks

TARGET	REACTION	PRODUCT	THRESHOLD [MeV]	HALF LIVE $T_{\frac{1}{2}}$	LINE ENERGY E_γ(kev)	INTENSITY %
^{12}C	γ,x (x=α,n)	^{7}Be	26.3MeV	53.4d	477.56	10.3
^{58}Ni	γ,p	^{57}Co	8.2	270.0d	122.07	85.6
	γ,n	^{57}Ni	12.2	37.0h	1377.62	84.9
	γ,np	^{56}Co	19.6	77.3d	846.75	99.99
	$\gamma,2n$	^{56}Ni	22.5	6.1d	158.30	99.00
	$\gamma,2np$	^{55}Co	29.5	18.0h	931.50	75.00
^{60}Ni	γ,np	^{58}Co	20.0	70.8d	810.75	99.45
^{54}Fe	γ,np	^{52}Mn	20.9	5.7d	1434.43	100.00
^{56}Fe	γ,np	^{54}Mn	20.4	312.2d	834.81	99.97
^{55}Mn	γ,n	^{54}Mn	10.2	312.2d	834.81	99.97
^{52}Cr	γ,n	^{51}Cr	12.0	27.7d	320.07	9.83
^{50}Cr	γ,np	^{48}V	21.6	15.97d	983.50	100.00

Table 3.3: List of photonuclear reactions and activation products found in tokamaks |13|

Device	References	Damaged Component	Material	Damage
TFR	128,129	vacuum vessel	stainless steel	piercing of the vessel
		poloidal limiter (outboard)	molybdenum	melting
		poloidal limiter (outboard)	stainless steel	melting
ORMAK	5	rodlimiter(outboard)	tungsten	melting/fracture after 10 runaway discharges
PLT	131,132	poloidal limiter (outboard)	stainless steel	melting
		poloidal limiter (outboard)	tung sten	melting
FT	134,135	mushroom limiter (outboard)	stainless steel	melting, erosion
TEXTOR	136	poloidal limiter (outboard)	graphite	crack formation to 2mm depth
JT-60	11,16,58,122	centre column tiles	molybdenum	melting
		centre column tiles	Inconel	melting
		centre column tiles	graphite	fracture of protruding tiles
		divertor tiles	graphite	fracture of tiles
JET	137-140	centre column tiles	Inconel	severe melting
		centre column tiles	graphite	fracture of protruding tiles
		centre column tiles	C-C	erosion
		outboard limiter	graphite	crack formation on one spot (~ 5 cm)

Table 3.4: Damage to plasma facing materials by runaway-electrons

(Injector)

Electron Gun	Model 12 (ARCO Type)
Applied Voltage	100 kV DC
Pulse Duration	3 - 100 ns (17 steps) 0.1 - 2.5 μs (continuous)
Emission Current	25 Amp. (20 ns), 6 Amps. (3 ns)

(Modulator)

High Voltage	23 kV	
Thyratron	KU 275C	
Repetition Rate	10 - 360 pps	480 - 720 pps
Pulse Duration	5 μs	2.4 μs
PFN	18 sections	9 sections

(accelerating waveguide)

Shunt impedance,	r'	40 MΩ/m
Figure of merit,	Q	19,000 (2π/3 mode)
Attenuation constant,	τ	0.834 nep (3.62 db)
Length,	L	3.0 meters (40 cavities)
Initial attenuation coefficient,	α(0)	0.0944 nep/m
Initial normalized group velocity,	V_g	0.0075
Electric field intensity,	V/L	11.63 MV/m
Filling time,	t_f	1.96 μs
Stored energy,	J	24 joules (18 MW)
Operating frequency,	f	1300 MHz

(Beam)

	Single Pulse Mode	Transient Mode	Steady State Mode
Pulse Duration	39.5 ps	3 - 100 ns	0.1 - 2.5 μs
Peak Current	14.0 nC	16 Amp.	0.6 Amp.
Energy	35 MeV	35 MeV (Zero Current)	
ΔE/E	1 %	3 %	3 %

Table 4.1: Specification of the electron linear accelerator of the Institute of Scientific and Industrial Research, Osaka University

	Experiments Section 4.2,4.3			*Experiments Section 4.5*	
Energy (MeV)	20	25	30	20	30
Pulse current (mA)	300	280	240	133*	113*
Pulse length (μs)	1.5	1.5	1.5	1.5	1.5
Repetition rate (pps)	120	120	120	120	120
Beam diameter (mm)	5	5	5	4	4
Power (J/pulse)	9.0	10.5	10.8	4.0	5.1

Remarks: * after passing through aluminium blind, aperture 4 mm; uncertainty in the pulse current: 20 %

Table 4.2: Electron beam irradiation parameters

System	*Energy and pulse number*	*Observed Damages*
2 mm graphite + 10 m stainl. steel	30 MeV 1200 pulses	Twin formation on substrate
5 mm graphite + 10 mm stainl. steel	30 MeV 1200 pulses	Initial twin formation on substrate
10 mm graphite + 10 mm stainl. steel	30 MeV 1200 pulses	
5 mm graphite + 10 mm stainl. steel	20 MeV 7200 pulses	Initial melting of stainl. steel substrate
10 mm graphite + 10 mm stainl. steel	20 MeV, 60 s 7200 pulses	Grain growth on substrate
2 mm graphite + 10 mm Mo (TZM)	20 MeV 5400 pulses	Melting of stainl. steel attachment, bolts, grain growth on substr.
5 mm graphite + 10 mm Mo (TZM)	20 MeV 5400 pulses	Initial melting of attachment bolts, slight grain growth on substrate
10 mm graphite + 10 mm Mo (TZM)	20 MeV 5400 pulses	

Table 4.3: Results of the irradiation tests on model layer systems

Material	Range (mm) at		Critical energy E_c (MeV)
	20 MeV	30 MeV	
Graphite	55.2	83.6	111.1
SiC + 2%AlN	31.1	47.0	62.5
Stainl. steel	12.4	18.8	29.4
Mo	9.7	14.7	18.5
W	5.2	7.8	10.6

Table 4.4: Electron range and critical energy of the materials tested (equ. 3.2 and 3.5)

material	peak comp. stress (N/mm^2)	comp. strength (N/mm^2)	peak tens. stress (N/mm^2)	tens. strength (N/mm^2)
AXF-5Q	-315	-143	64	63
CL5890PT	-141	-130	30	33
EK98	-105	-110	21	30
FP219	- 78	- 75	15	16
ATJ	- 72	- 70	17	30

Table 4.5: Comparison of the numerically determined thermal stresses (peak values) for a surface heat load of 100 MW/m^2 and a duration of 200 ms with the compressive and tensile strengths of the materials at room temperature

Operation phase	Physics	Technology
Maximum fusion power MW	1000	700-1000
Maximum thermal power MW	~1300	1000-1300
Plasma configuration		
major radius, m	5.8	5.5
minor radius, m	2.2	1.8
elongation	1.88	2.0
Number of pulses x 10^4	1	2-5
Plasma energy MJ		
thermal	≤900	≤600
magnetic	<1000	<400
First wall neutron fluence MWa/m^2		
average	0.02	1-3
maximum	0.03	1.5-4.5
Availability %	low	
average	-	≈10
maximum	-	≈25
peak (2 week period)	-	close to 100
Pulse burn time, s	$2 \cdot 10^2$	$1\text{-}3 \cdot 10^3$
Pulse off-burn time, s	$\geq 10^3$	$>10^2$

OPERATION PHASE		PHYSICS		TECHNOLOGY	
COMPONENTS		FIRST WALL	DIVERTOR PLATES	FIRST WALL	DIVERTOR PLATES
DISRUPTIONS					
- THERMAL QUENCH					
• TOTAL NUMBER AT FULL LOAD		1000	200*	10-100	2-20*
• TIME	ms	0.1-3		0.1-3	
• PEAK ENERGY DEPOSITION	MJ/m^2	2.5	5-10	2	5-10
- CURRENT QUENCH					
• TOTAL NUMBER AT FULL LOAD		2000	400*	10-100	2-20*
• TIME	ms	5-50		5-50	
• RADIATIVE ENERGY DEPOS.	MJ/m^2	2	2	1.5	1.5
• RUN-AWAY ELECTRONS	MJ/m^2	50-500		50-500	

NOTES

* Assuming about 5 divertor plate replacements during each phase.

Table 5.1: ITER operation and disruption parameters |26|

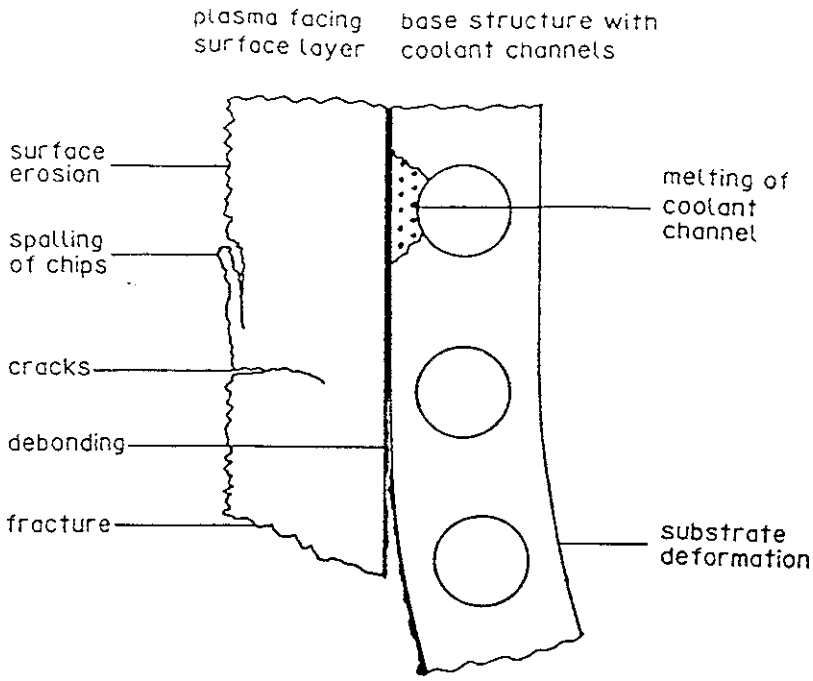

Figure 1.1: Possible damage to plasma facing materials and components due to runaway-electron impact

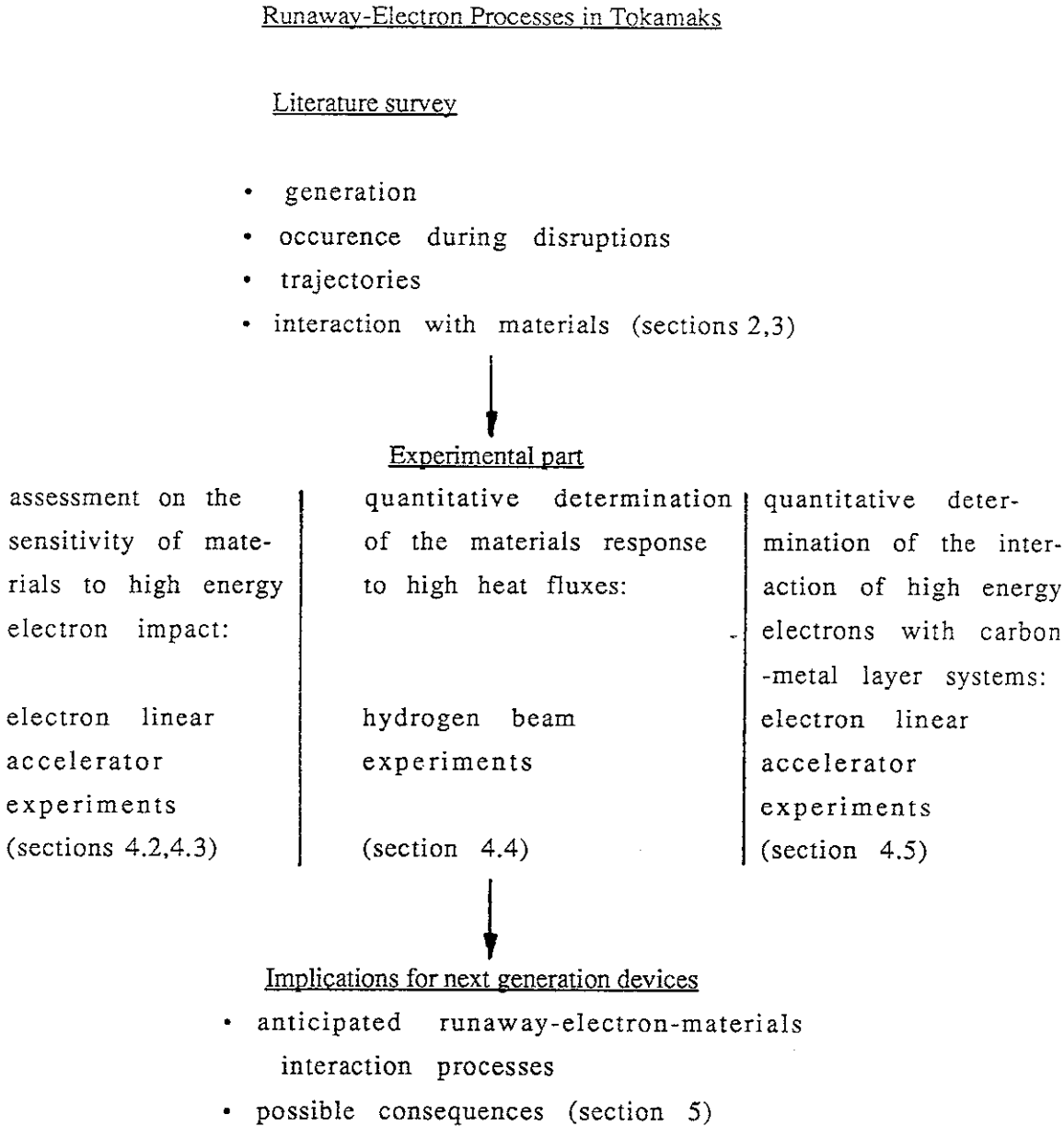

Figure 1.2: Structure of the work

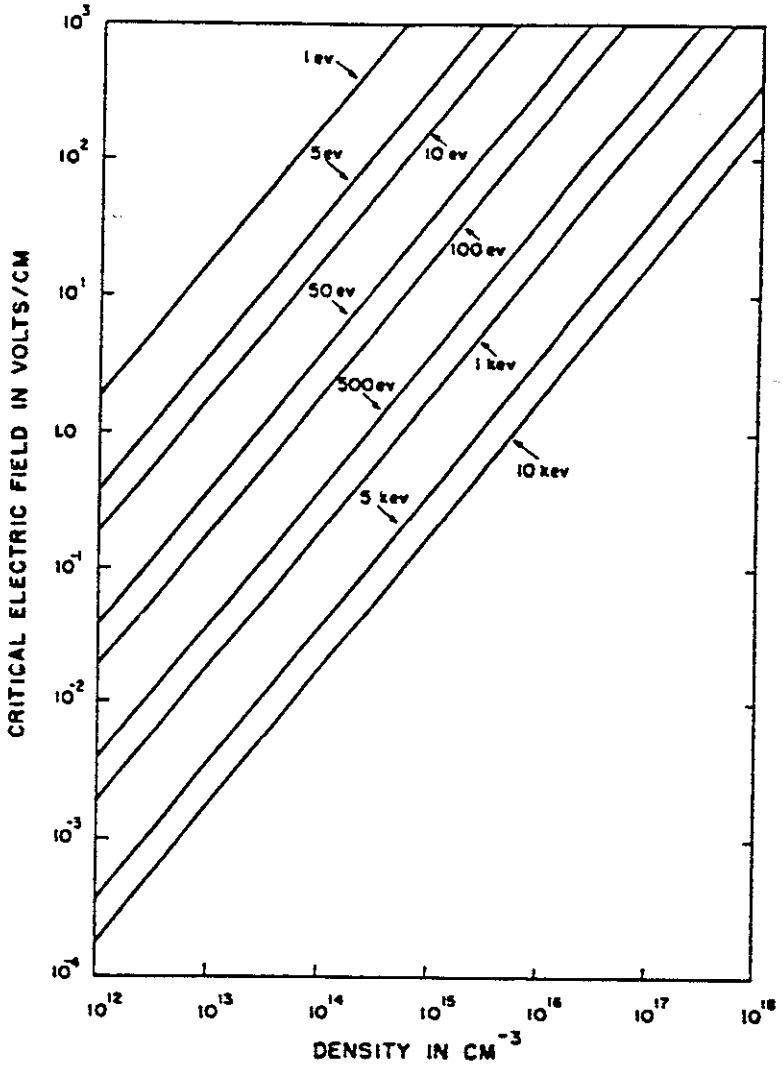

Figure 2.1: Dreicer field as a function of the particle density for different electron energies [51]

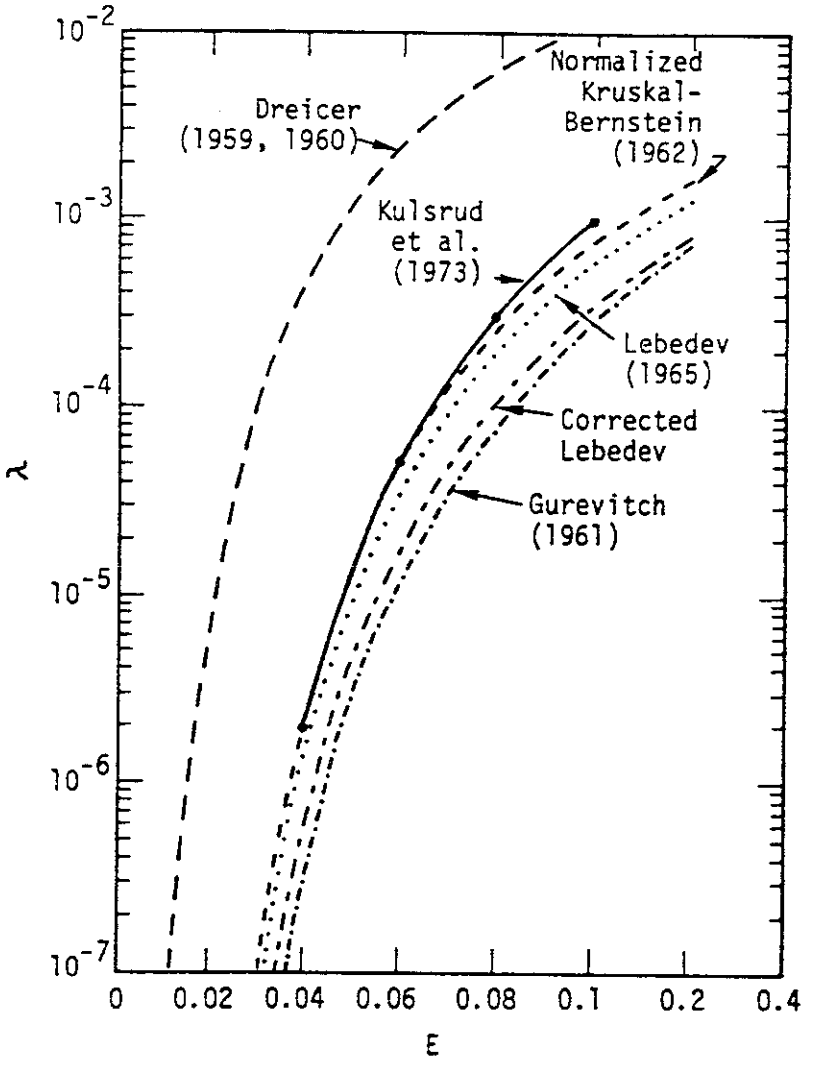

Figure 2.2: Comparison of analytically and numerically determined runaway rates for Z = 1. The Kruskal-Bernstein expression is normalized to the numerical value of Kulsrud et al. at E = 0.04 |5,46|

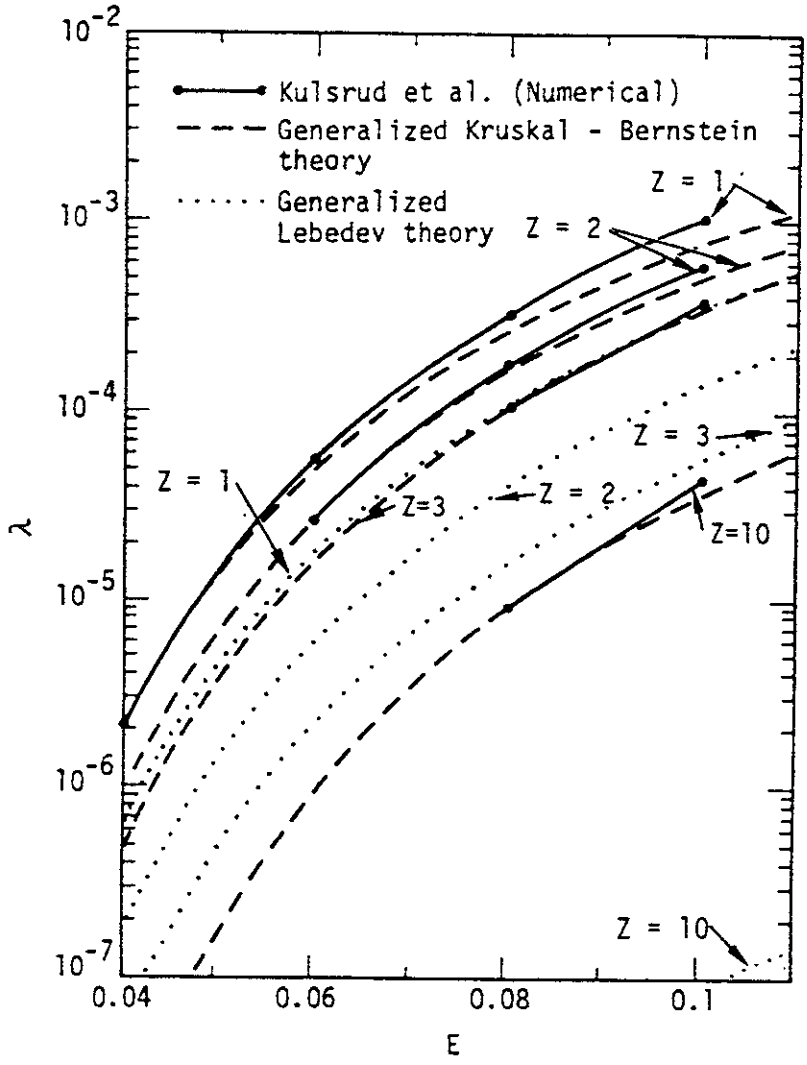

Figure 2.3: Comparison of analytically and numerically determined runaway rates for several values of Z. For each value of Z the generalized Kruskal-Bernstein expression is normalized to the numerical value at the lowest electric field strength considered by Kulsrud et al. |53|

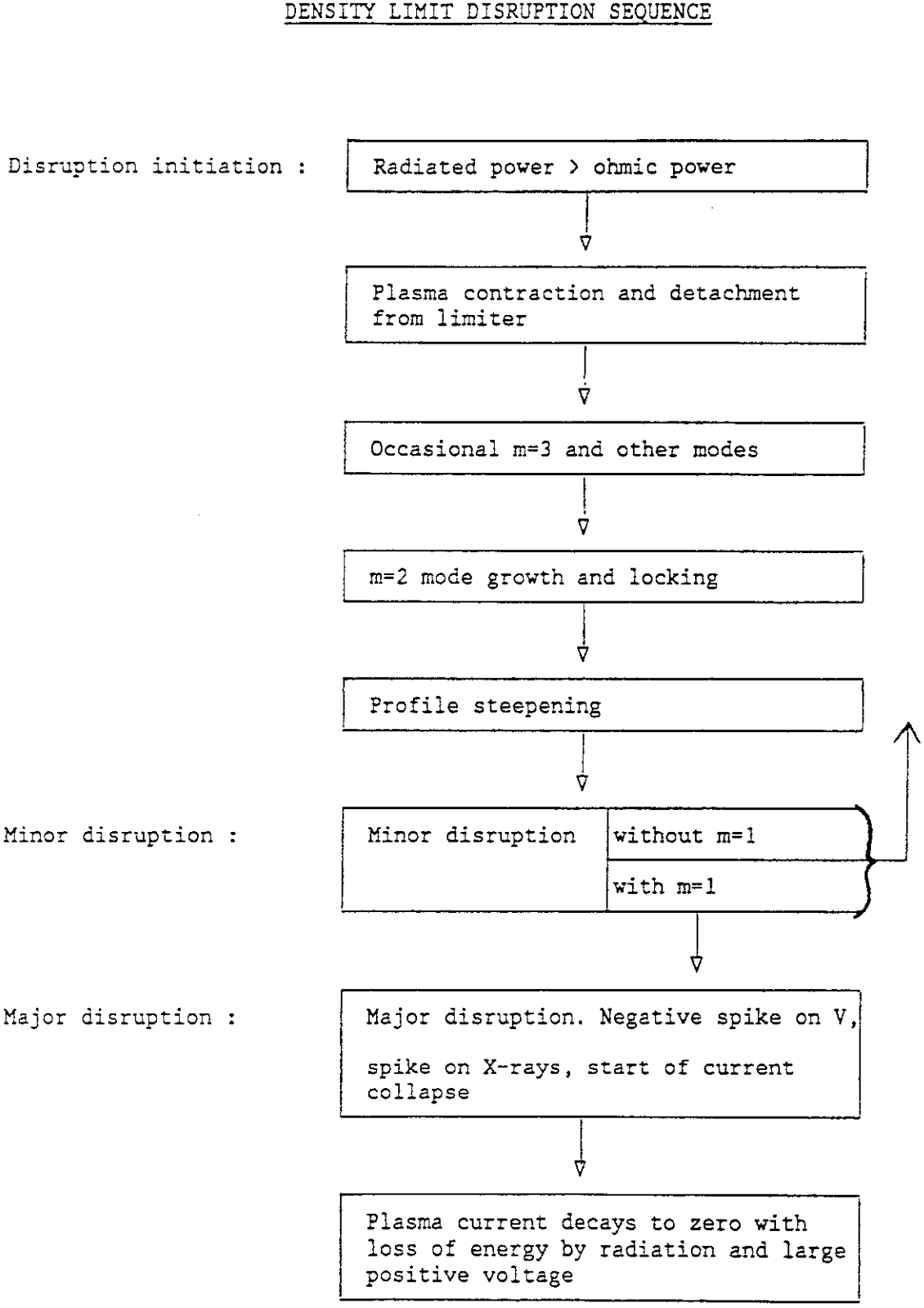

Figure 2.4: Density limit disruption sequence |13|

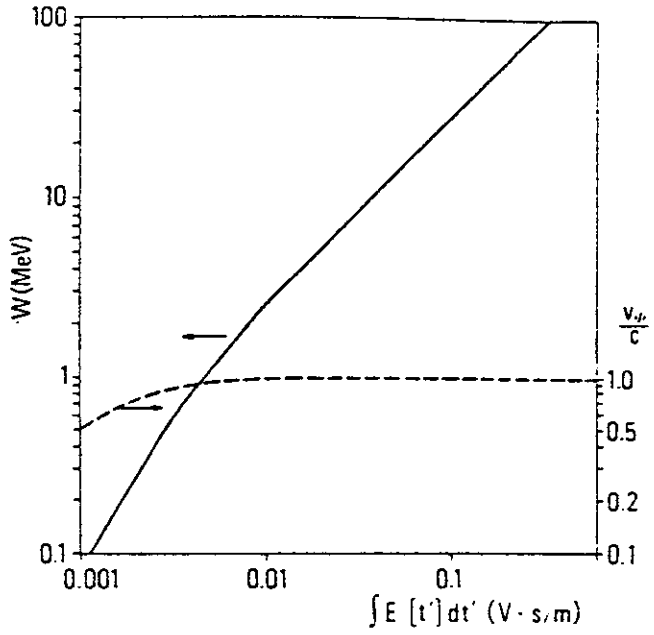

Figure 2.5: Energy and velocity of an electron undergoing free-fall acceleration as function of $\int_0^t E\,(t')\,dt'$ (Vs/m) [5]

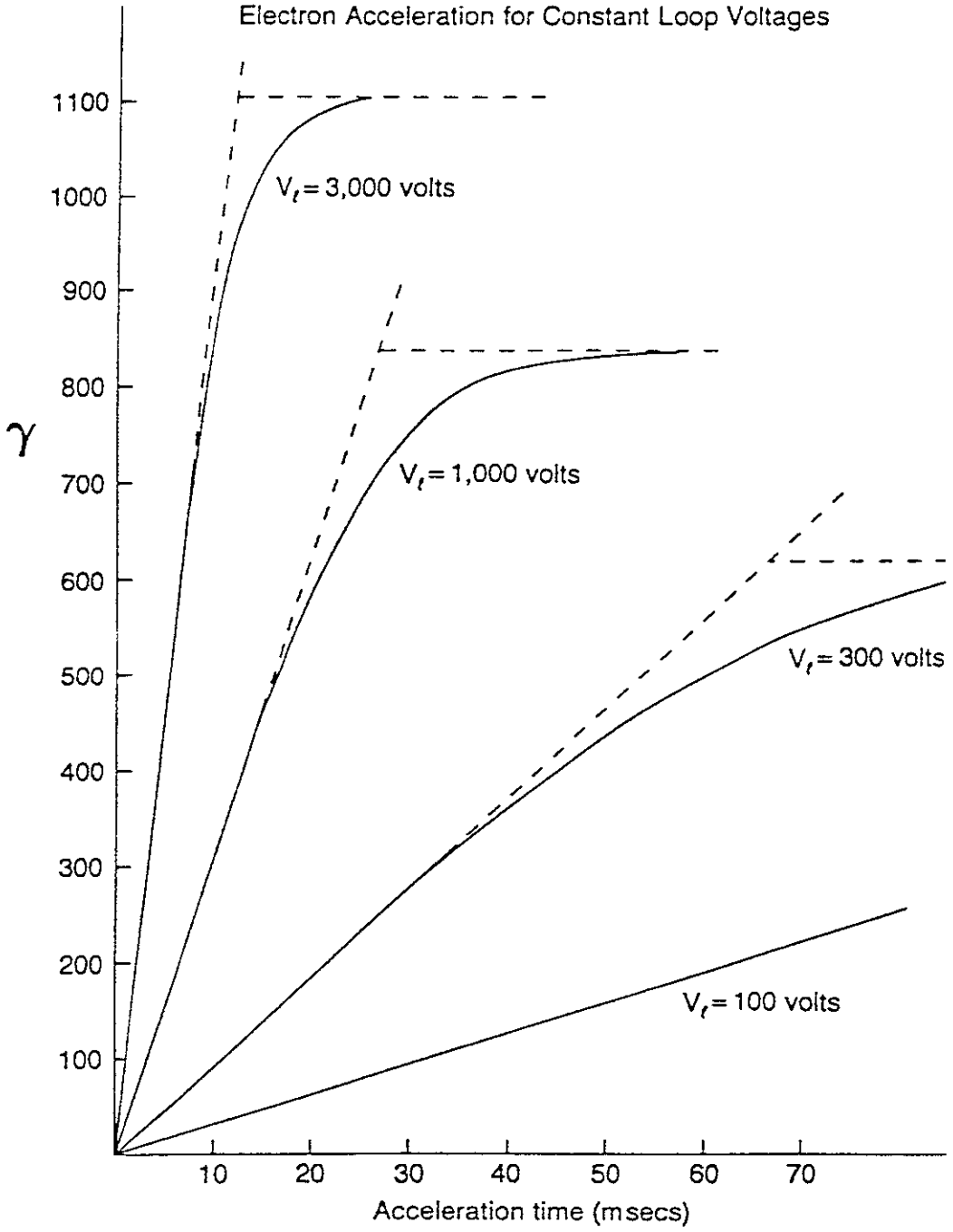

Figure 2.6: Acceleration of electrons under the influence of constant loop voltages of different magnitudes. The electron energy is given by $W = \gamma\ m_e c^2$ and an orbit radius of 3.0 m is assumed |13|

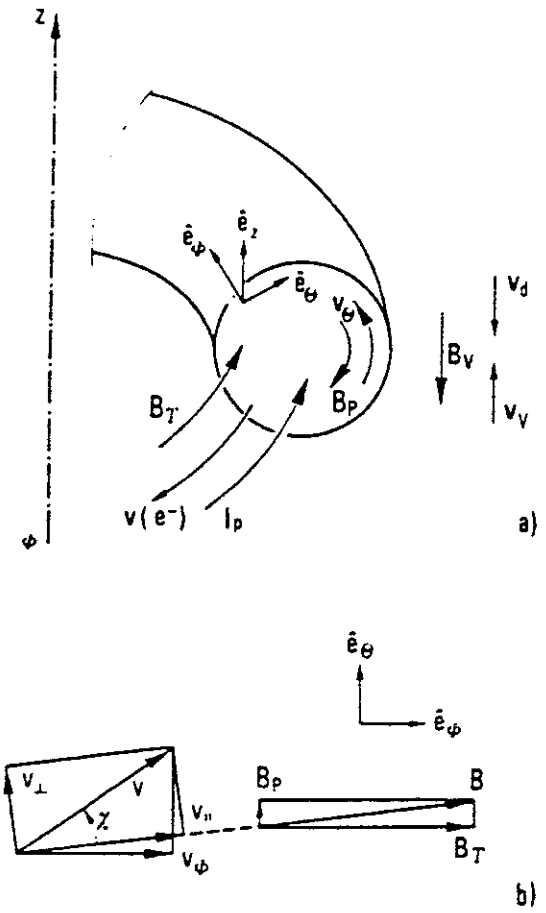

Figure 2.7: a) Drift velocities for electrons and magnetic field in a tokamak configuration
b) Definition of velocity and magnetic field components

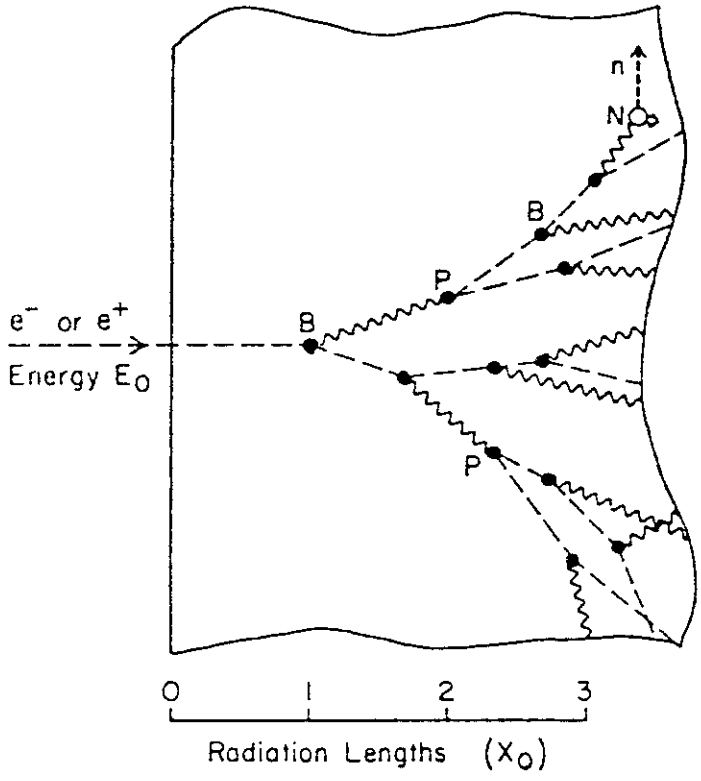

Figure 3.1: Development of an electromagnetic cascade in a semi-infinite medium at high energy (well above the critical energy). The dashed lines represent electrons or positrons and the wavy lines are photons. An electron or positron of energy W_0 is incident at the left (a cascade can also be initiated by a photon). The spreading in the transverse direction is greatly exaggerated for clarity. Only bremsstrahlung (B) and pair production (P) events are shown, but Compton scattering also plays a role in the dispersal of energy. Energy is deposited in the medium along dashed lines by ionization. Photonuclear reactions, as illustrated by the (γ,n) reaction at N, may take place along any of the wavy lines if the energy of that photon is high enough. They occur much less frequently than might be inferred from this illustration |97|.

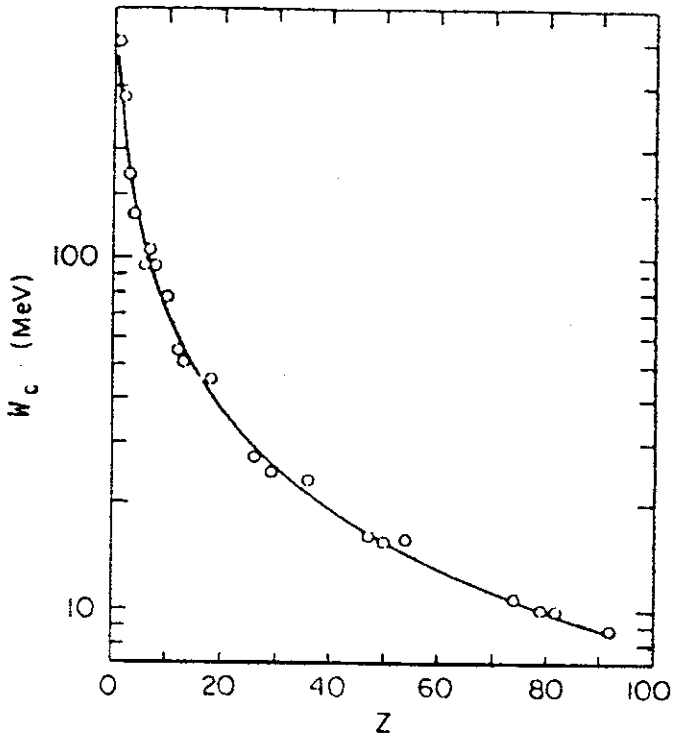

Figure 3.2: Critical energy W_C as a function of the atomic number Z (equ. 3.2) |97|.

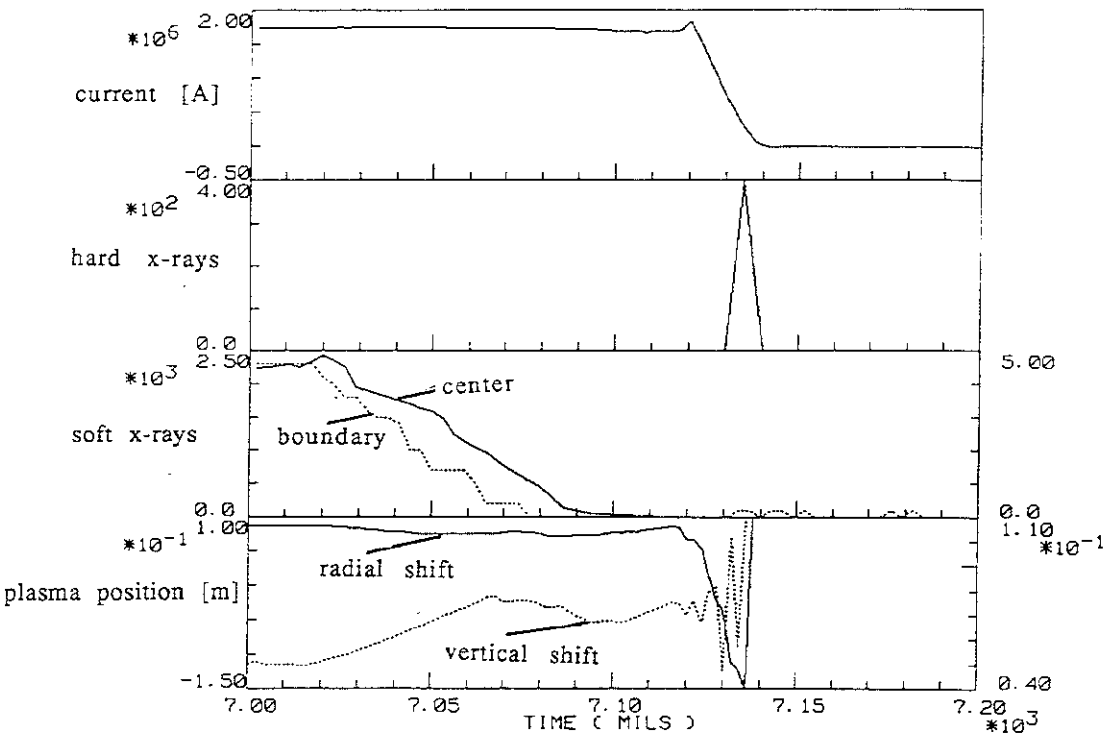

Figure 3.3: Plots of current, hard x-ray and soft x-ray emission, and plasma position during a JT-60 discharge which was terminated by a disruption. Besides a radial shift the plasma performs strong vertical movements [16].

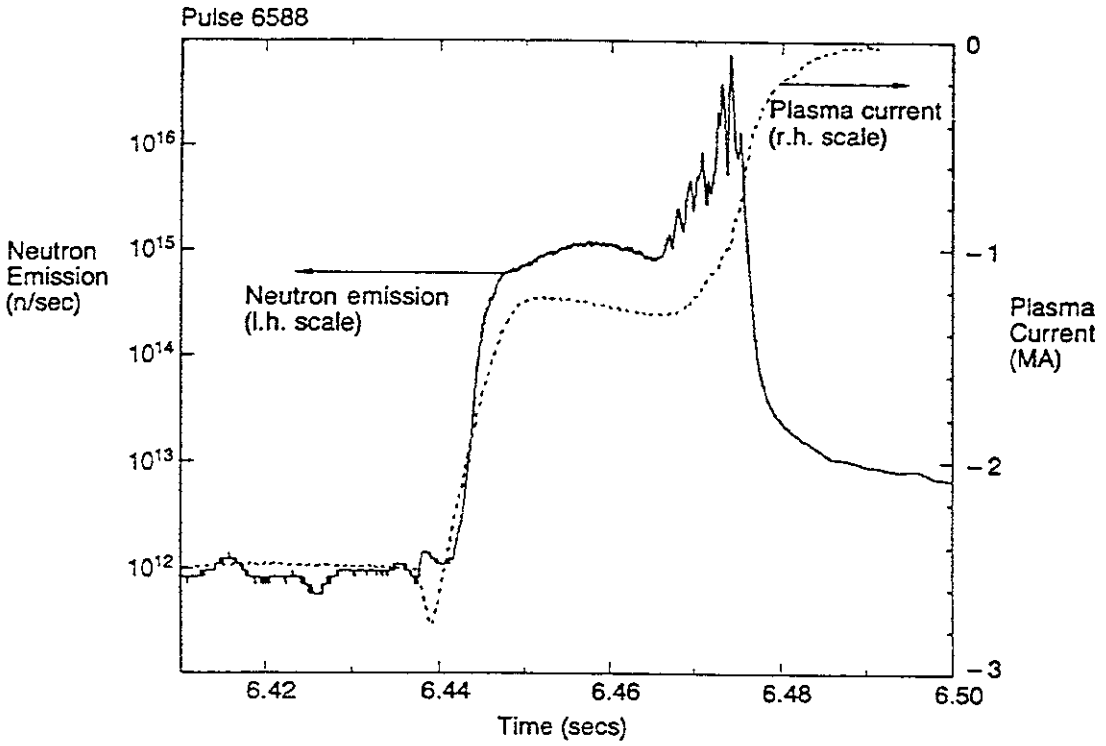

Figure 3.4: Neutron emission and plasma current during a disruption in JET. The hesitation in the decay of the plasma current indicates that a runaway-electron current of > 1 MA has been established for a duration of more than 20 ms |13|.

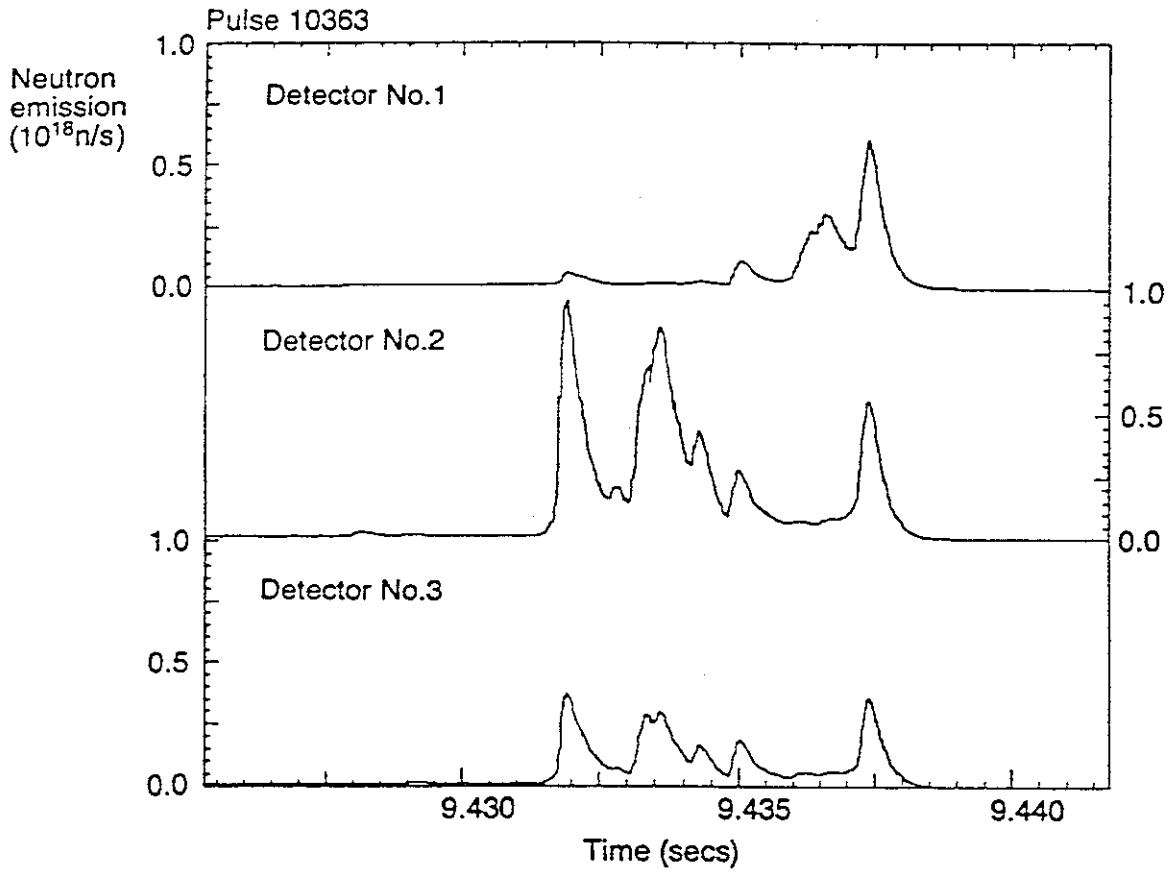

Figure 3.5: Plots of the neutron emission during a disruption in JET. The detectors were located at different toroidal positions. The different relative amplitudes of the signals indicate that the neutrons originate from several distinct locations |13|.

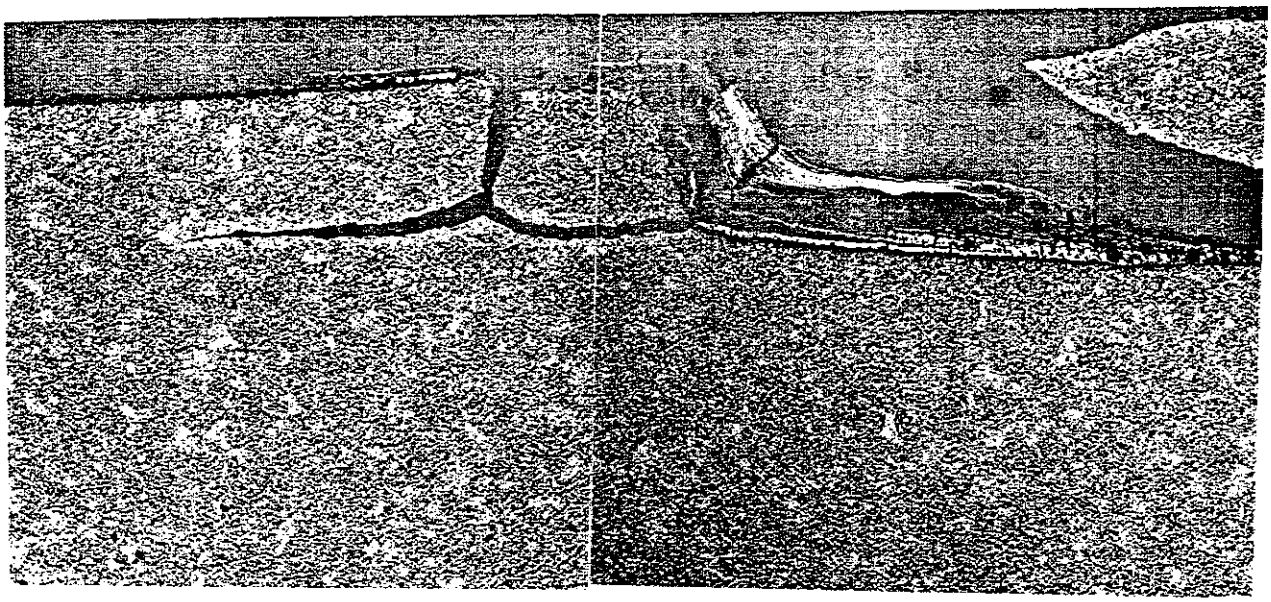

Figure 3.6: Metallographic cross-section through a graphite limiter from TEXTOR. The limiter surface was hit by a runaway-electron event which caused cracking of the graphite on a surface area of several cm^2.

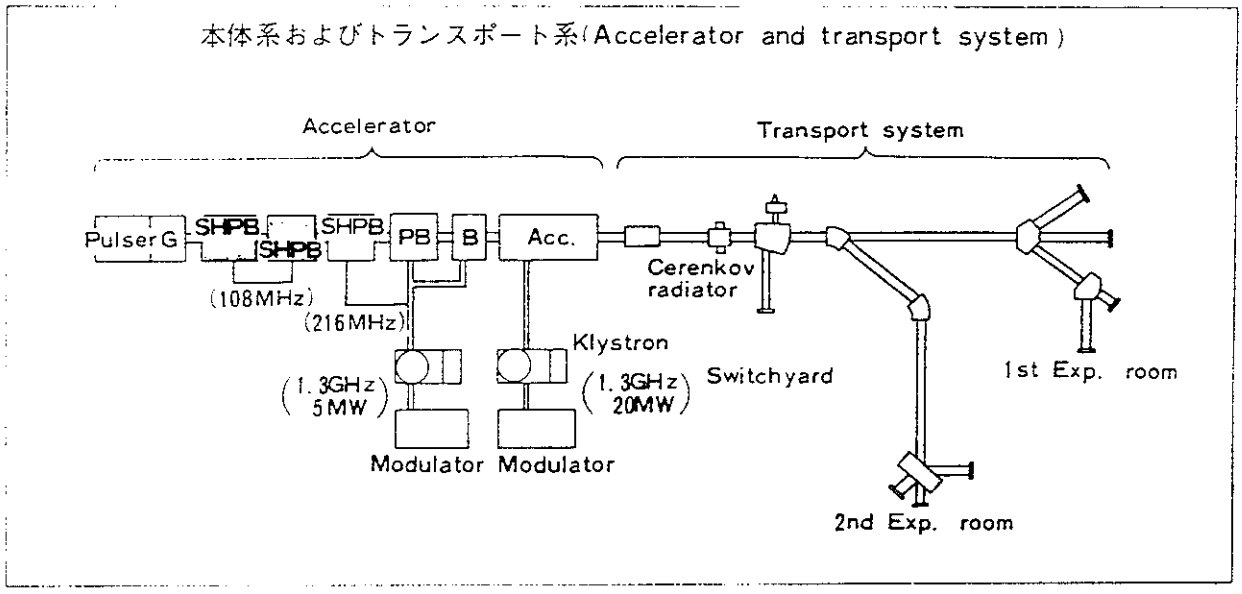

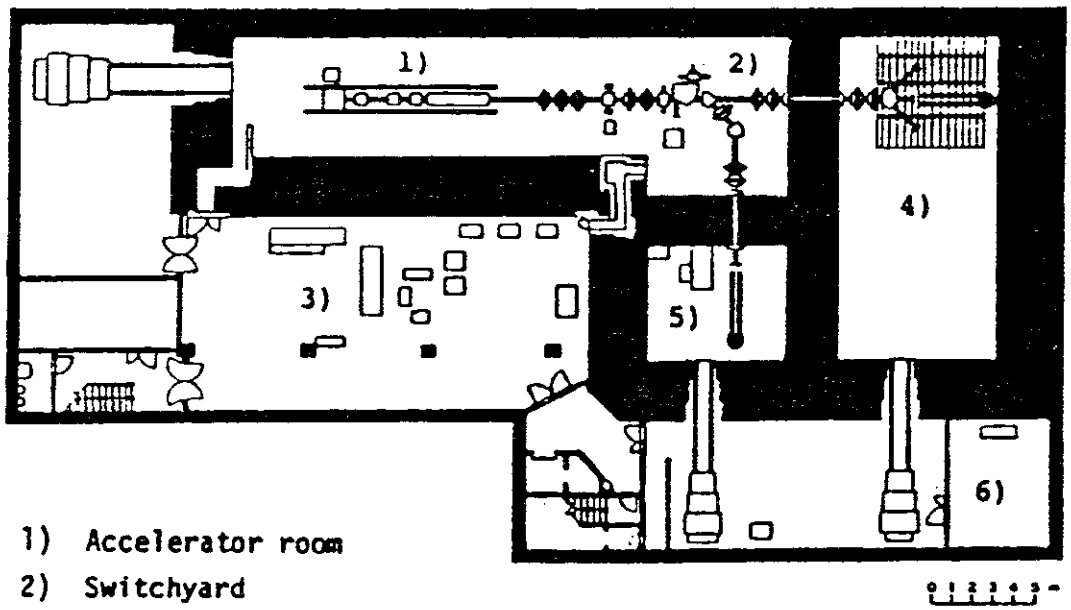

1) Accelerator room
2) Switchyard
3) Control room and measurement room
4) No.1 Experimental room
5) No.2 Experimental room
6) Measurement room

Figure 4.1: Layout of the electron linear accelerator of the Institute of Scientific and Industrial Research, Osaka University, which was used for experiments.

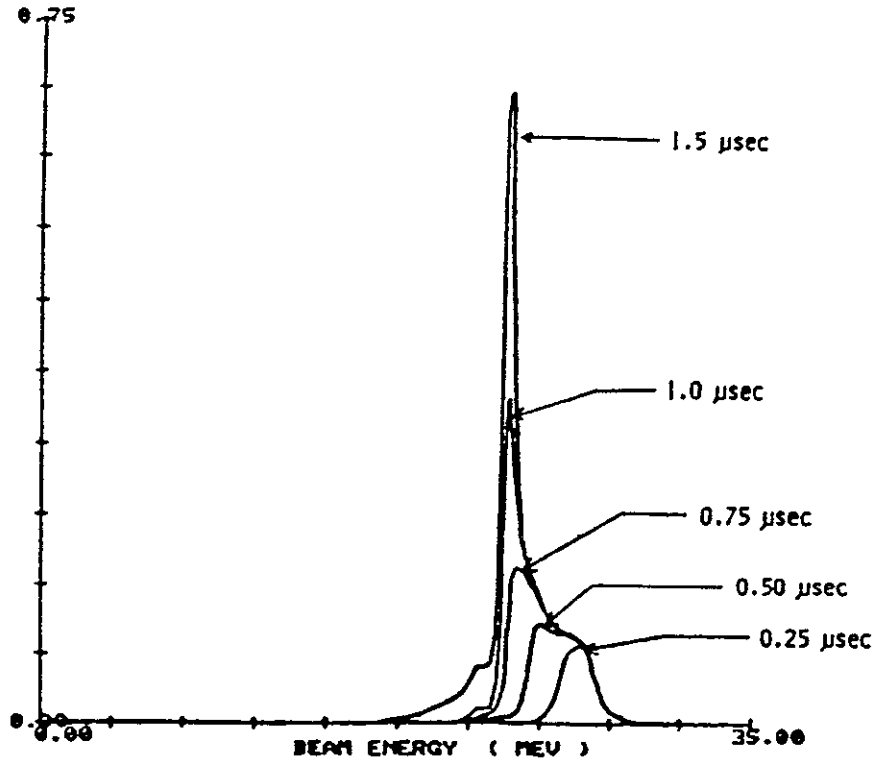

Figure 4.2: Beam energy spectra for different pulse lengths of the electron linear accelerator.

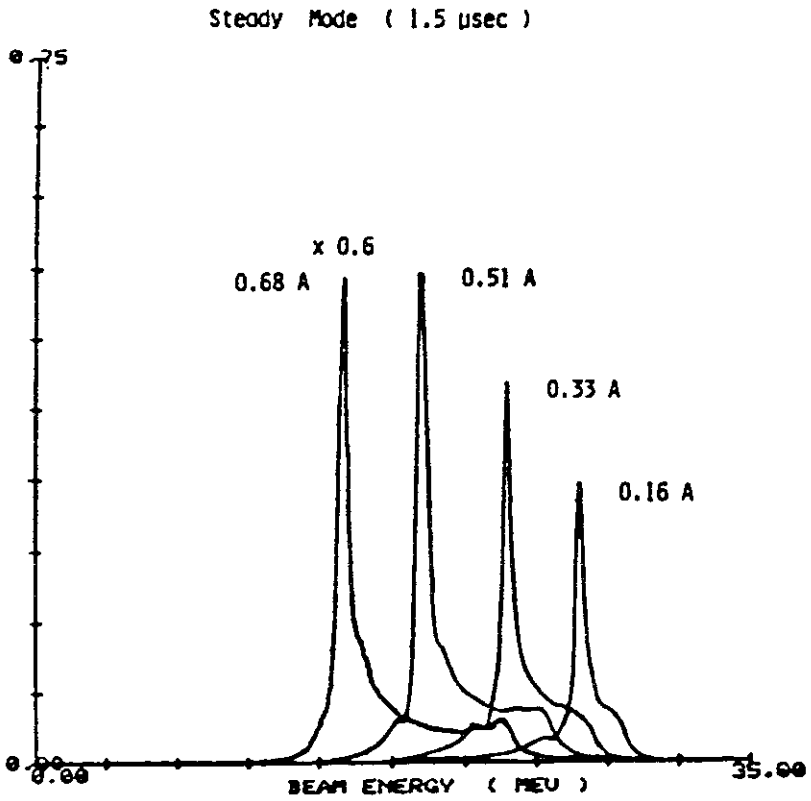

Figure 4.3: Typical energy spectra of the electron linear accelerator beam (1.5 μs) in the steady state mode. The current decreases with increasing beam energy.

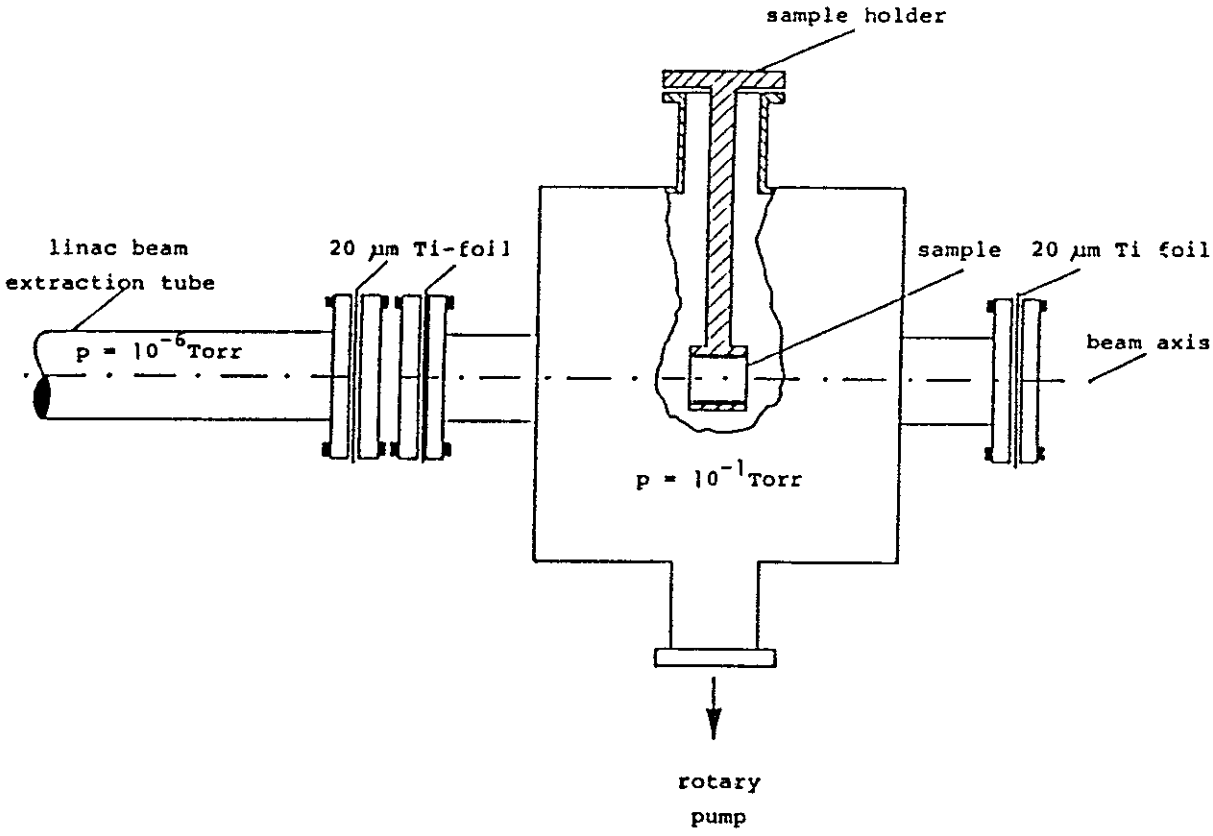

Figure 4.4: Set-up for linear accelerator experiments. The beam is coupled into the target chamber via 20 µm thick Ti-foils. Beam incidence onto the specimen surface is perpendicular.

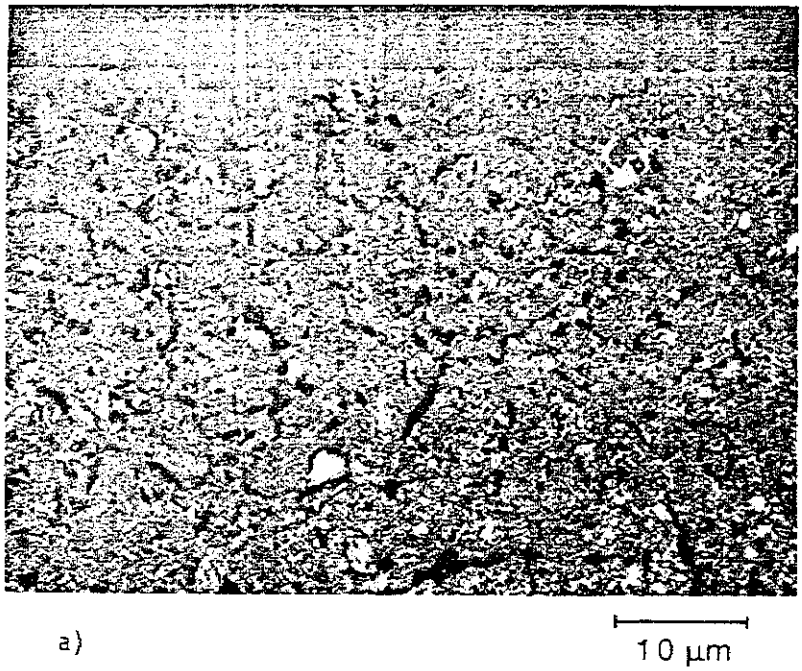

Figure 4.5: a) Cross-section of unirradiated graphite EK 98
b) Cross-section of a graphite EK 98 sample subjected to 7200 pulses, 20 MeV (64.8 kJ)

124

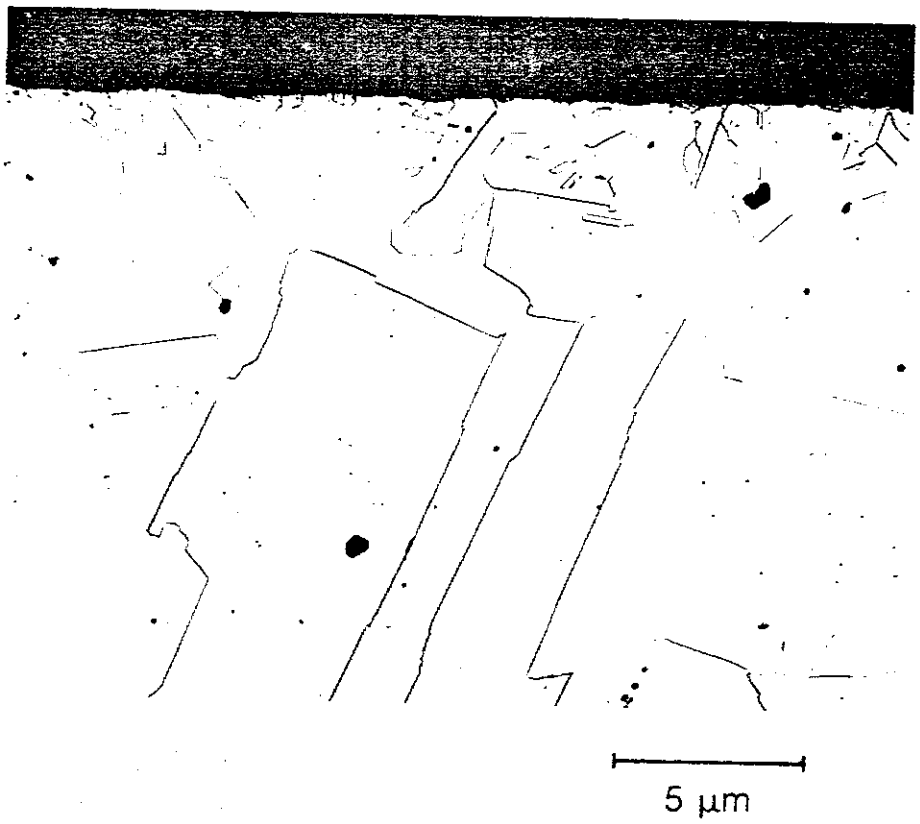

Figure 4.6: Cross-section of a stainless steel (SUS316) sample subjected to 3600 pulses, 20 MeV (32,4 kJ).

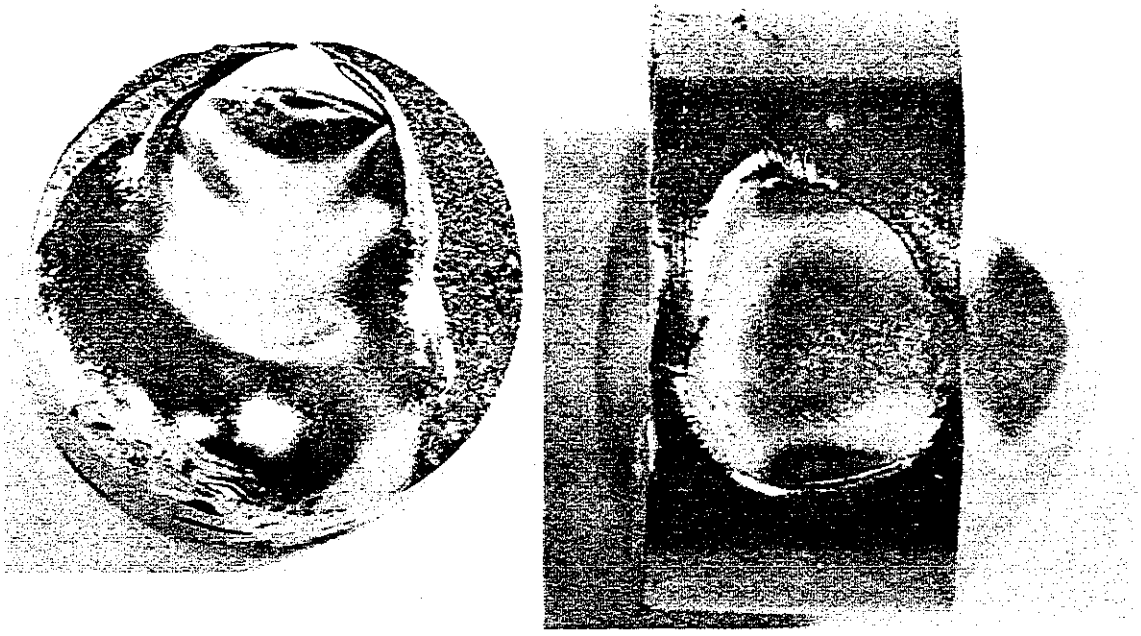

Figure 4.7: Stainless steel sample melted after 7200 pulses, 20 MeV (64.8 kJ)

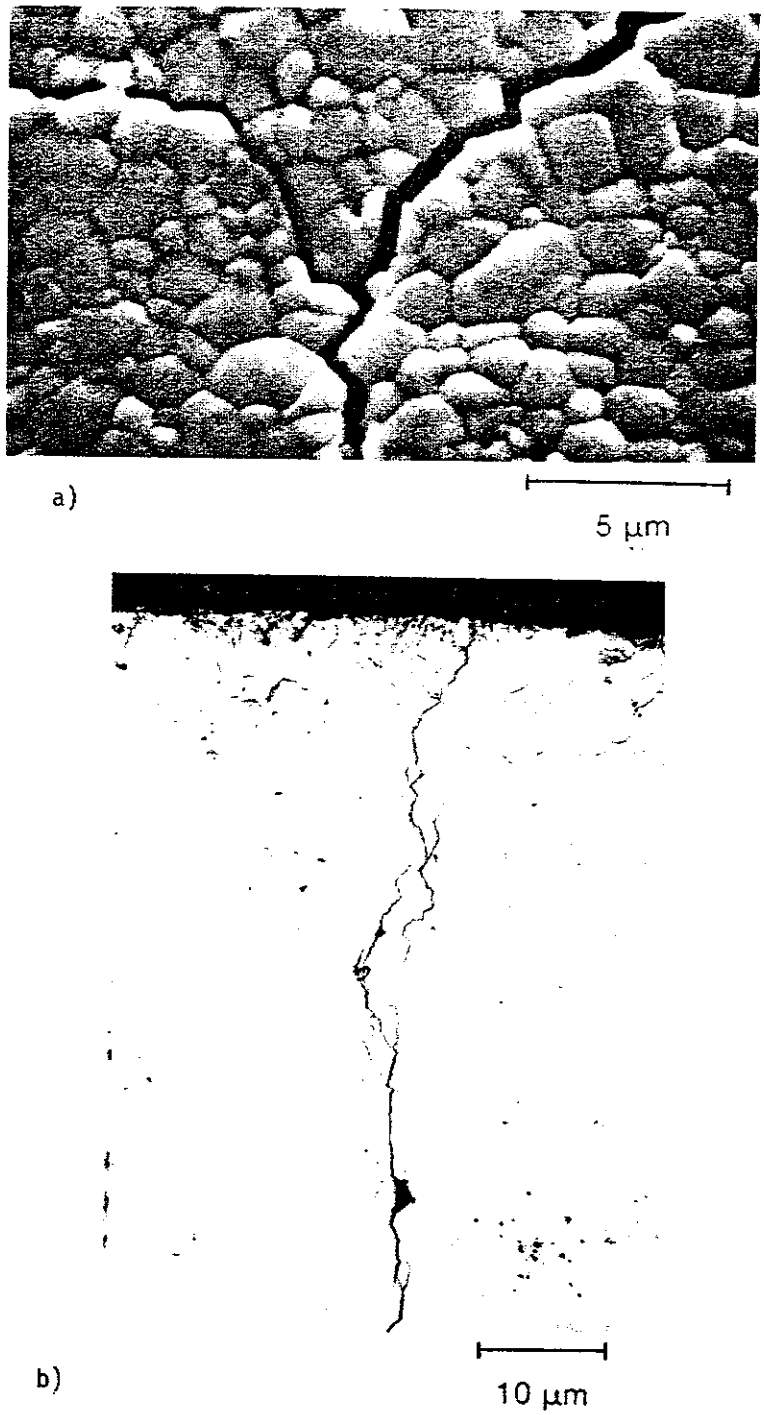

Figure 4.8: Tungsten sample subjected to 3600 pulses, 30 MeV (38.9 kJ)
a) SEM image of the impact surface
b) Cross-section showing the crack penetration

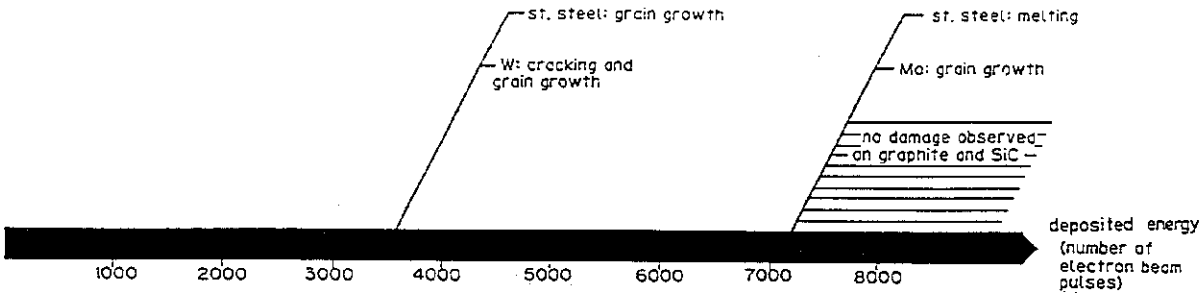

Figure 4.9: Results of the irradiation tests on bulk materials at 20 and 30 MeV as function of the deposited energy.

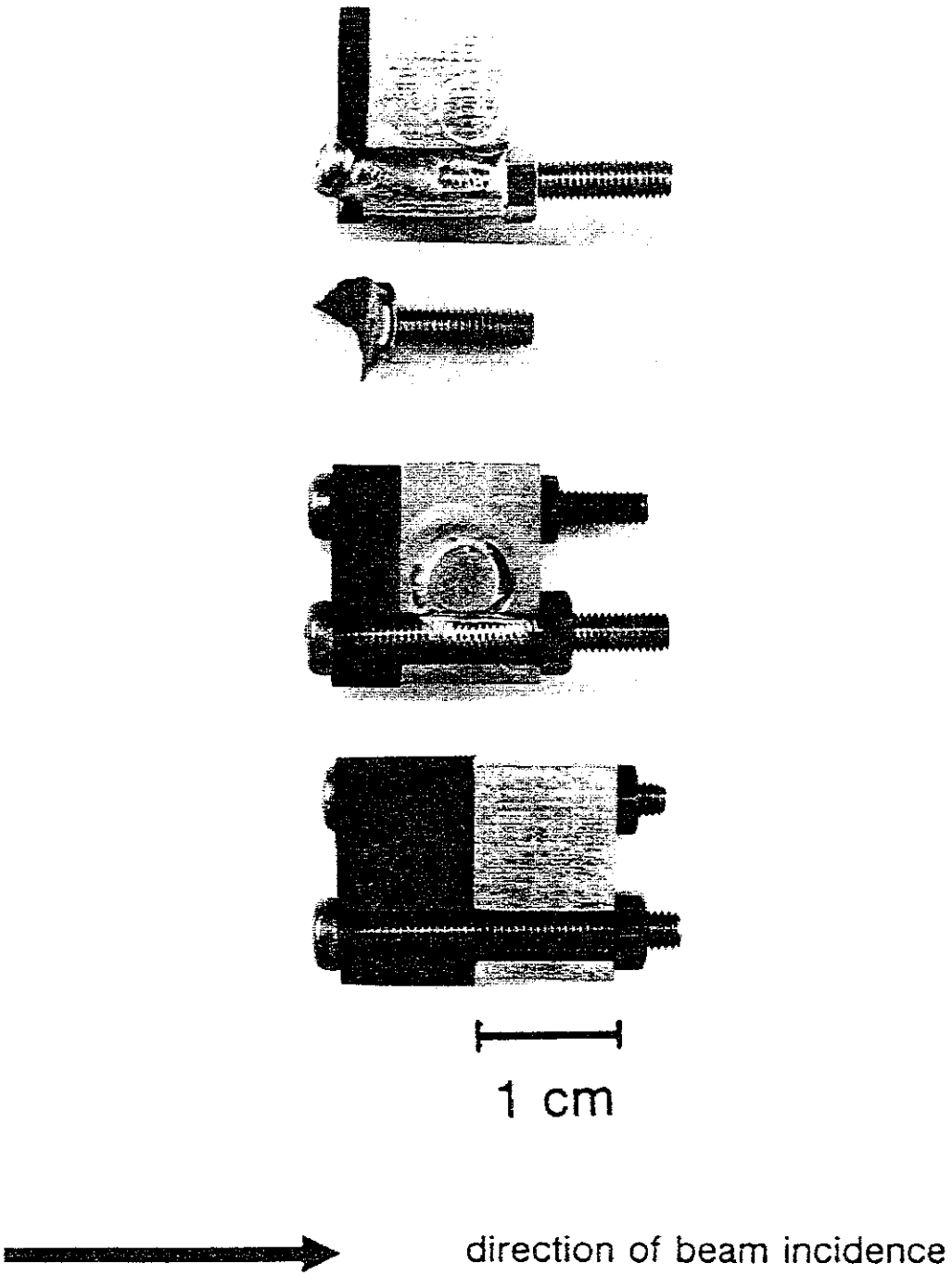

Figure 4.10: Model layer systems after electron irradiation, 5400 pulses, 20 MeV (48.6 kJ). Graphite layers (left) have been attached to molybdenum substrates (right) by stainless steel nuts and bolts. Thermal excursions of the substrates occured in the case of thin graphite layers and caused melting of the attachment parts.

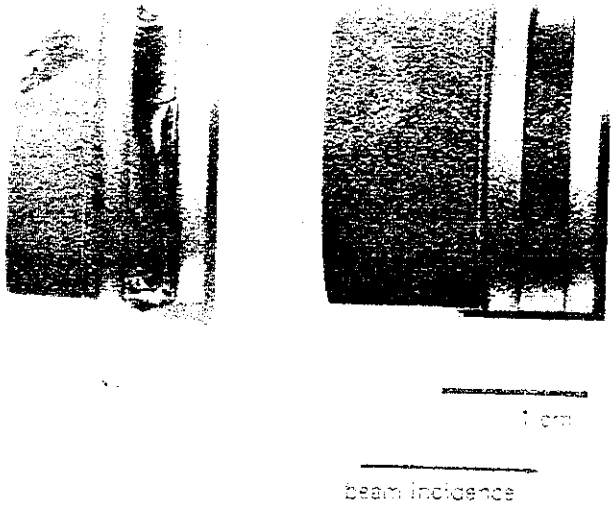

Figure 4.11: Brazed layer systems of graphite brazed Mo-Cu-Mo substrate after irradiation, 7200 pulses, 20 MeV (64.8 kJ). The specimen with a graphite layer of 5 mm thickness (left) underwent melting of the Cu-phase. The specimen with a 10 mm graphite layer (right) shows no damage.

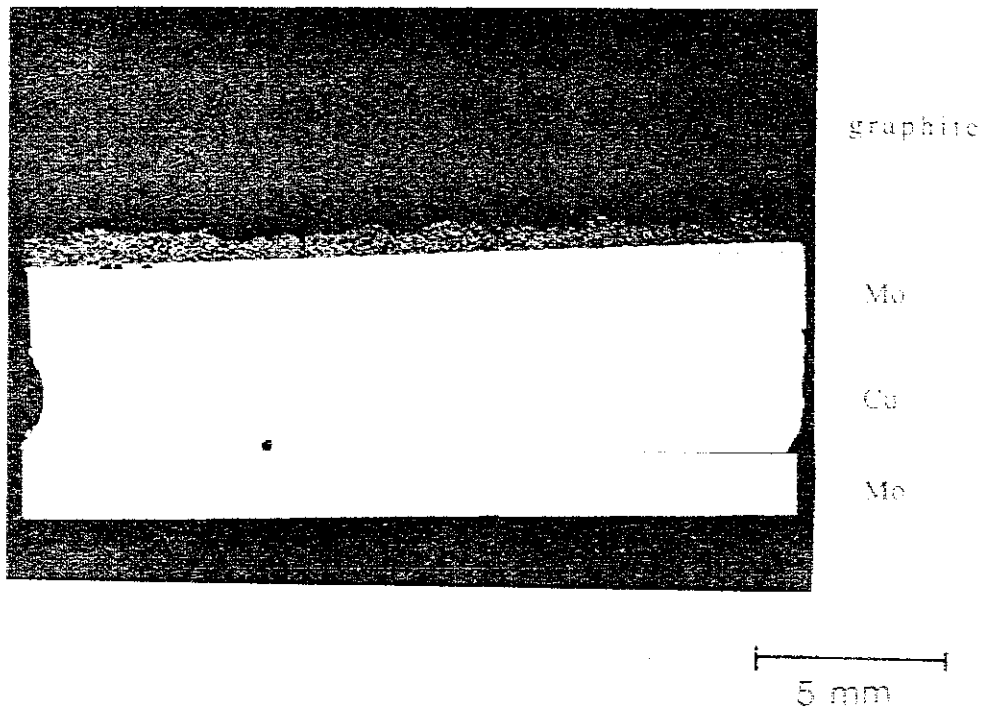

Figure 4.12: Cross-section of the left side sample of Fig. 4.11 showing the melted Cu-layer.

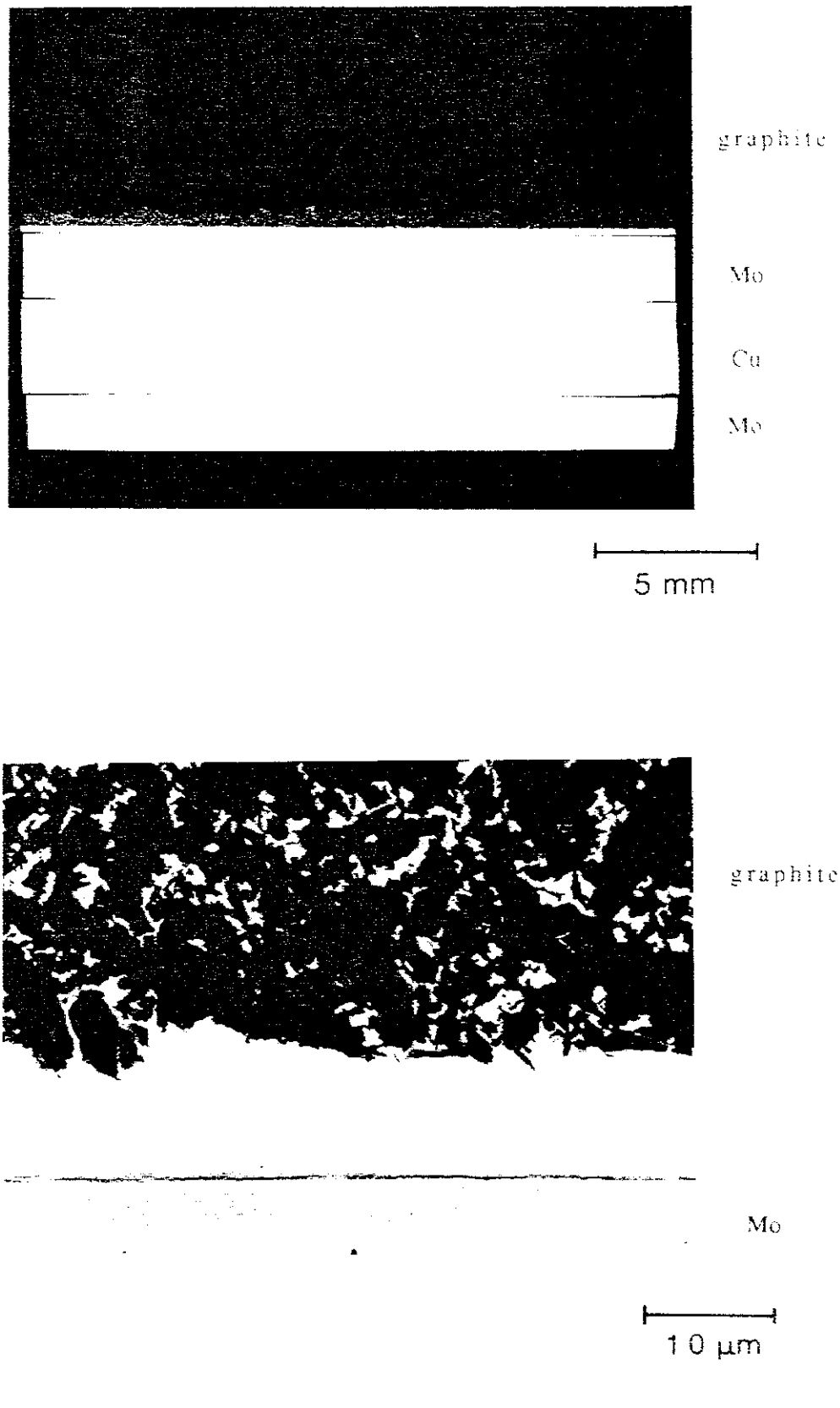

Figure 4.13: Cross-section of the right side sample of fig. 4.11. No damage occured in the interface region.

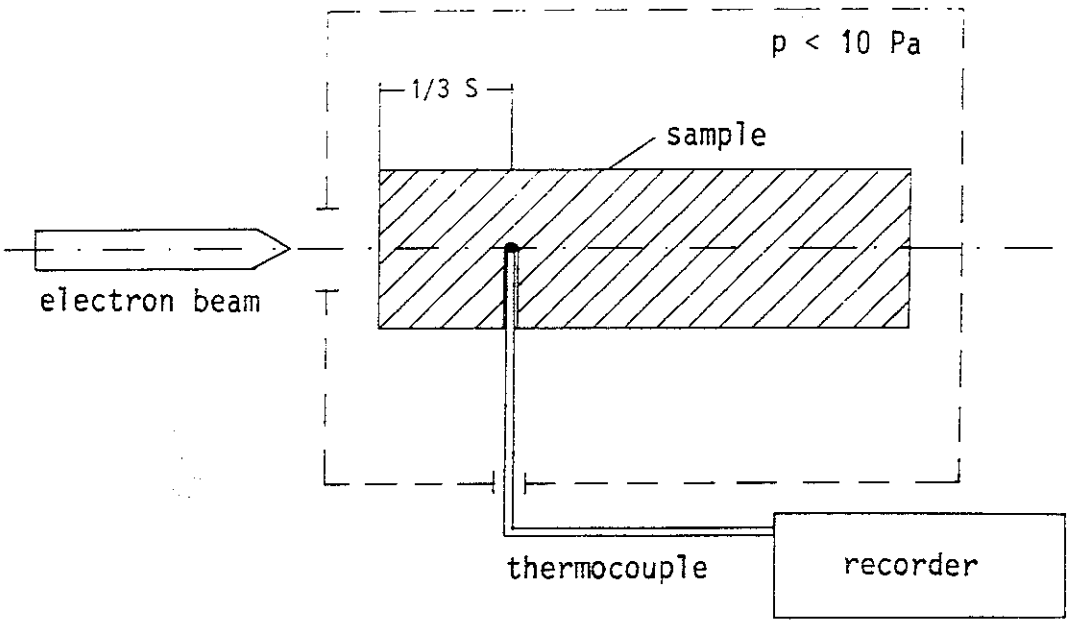

Figure 4.14: Set-up of experiments measuring the temperature rise in the materials under high energy electron irradiation.

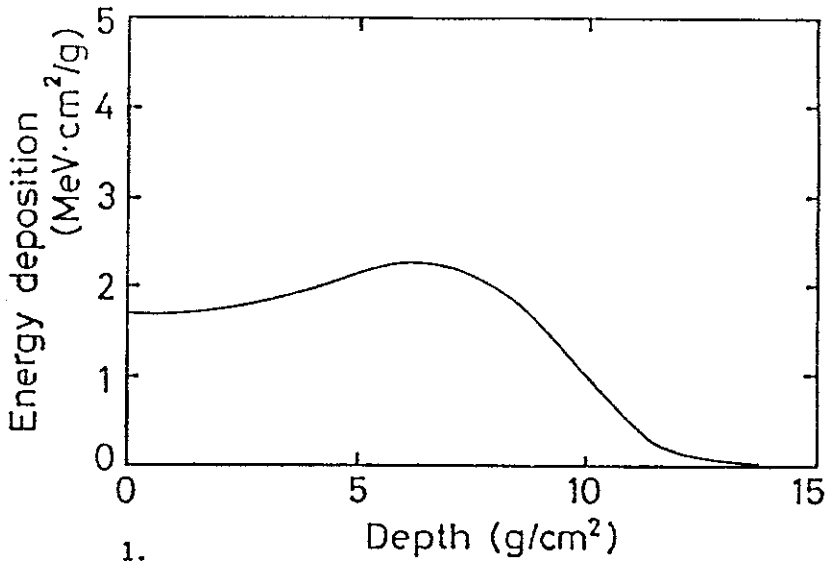

1.

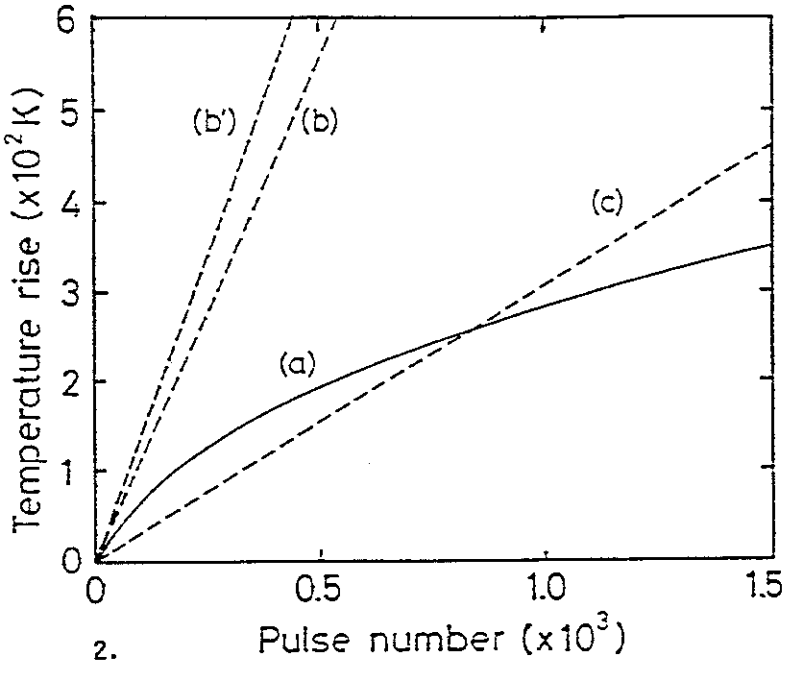

2.

Figure 4.15: 1. Energy deposition distribution of 20 MeV electrons in the semi-infinite absorber of graphite

2. Temperature rise within the graphite sample during 20 MeV electron irradiation

a) measured

b) no thermal diffusion, b') at energy peak

c) uniform body heating

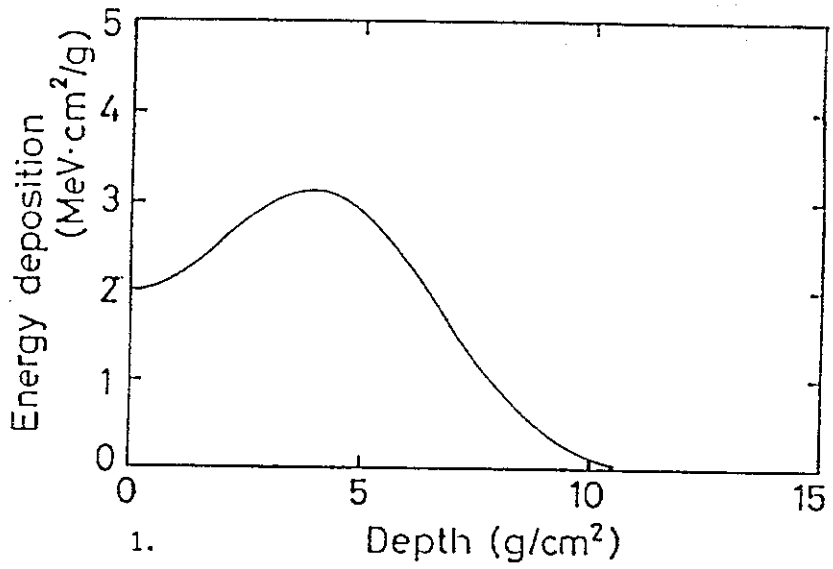

1.

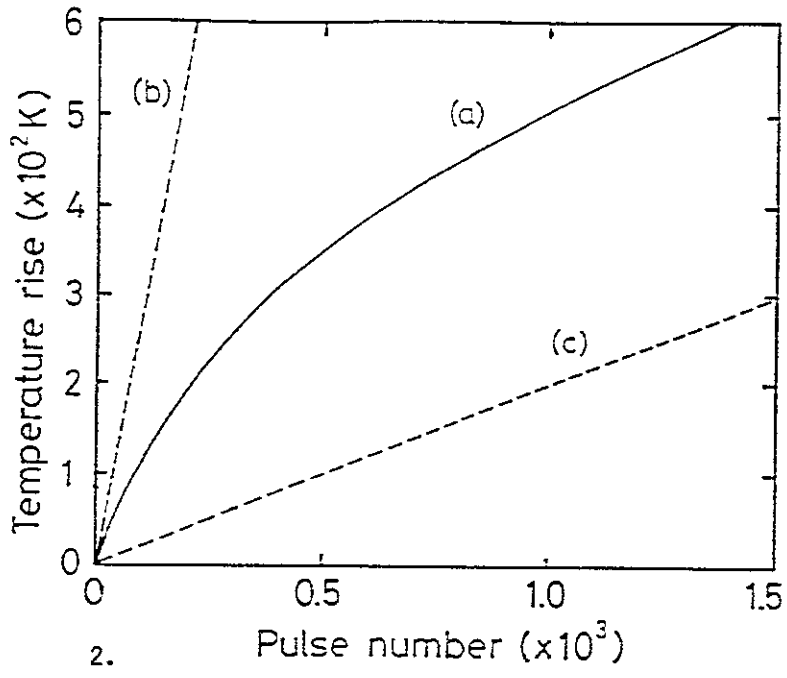

2.

Figure 4.16: 1. Energy deposition distribution of 20 MeV electrons in the semi-infinite absorber of stainless steel

2. Temperature rise within the stainless steel sample during 20 MeV electron irradiation

a) measured

b) no thermal diffusion

c) uniform body heating

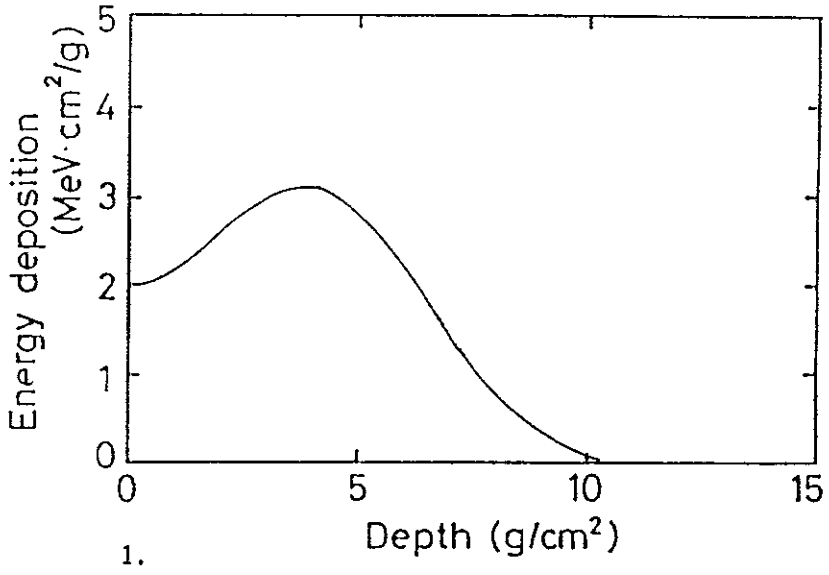

1.

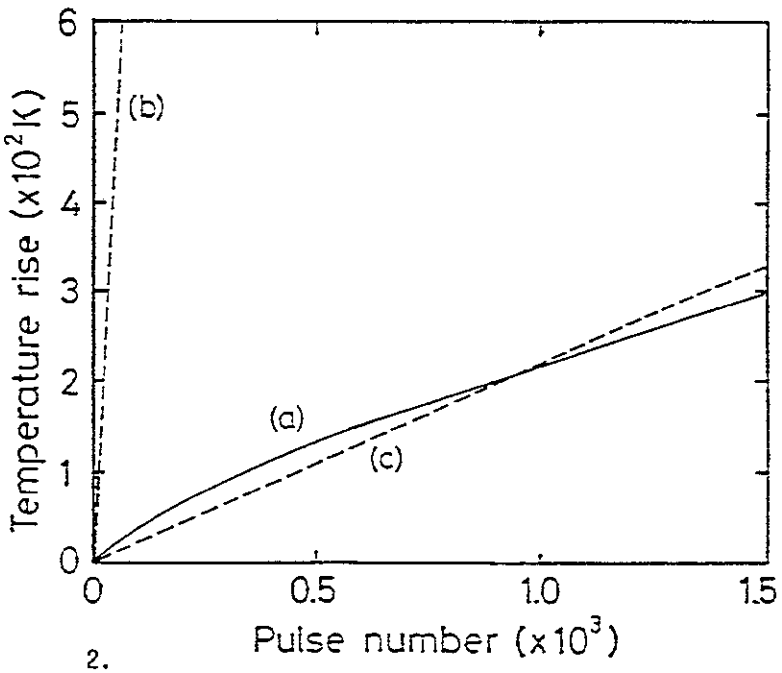

2.

Figure 4.17: 1. Energy deposition distribution of 20 MeV electrons in the semi-infinite absorber of copper.

2. Temperature rise within the copper sample during 20 MeV electron irradiation

a) measured

b) no thermal diffusion

c) uniform body heating

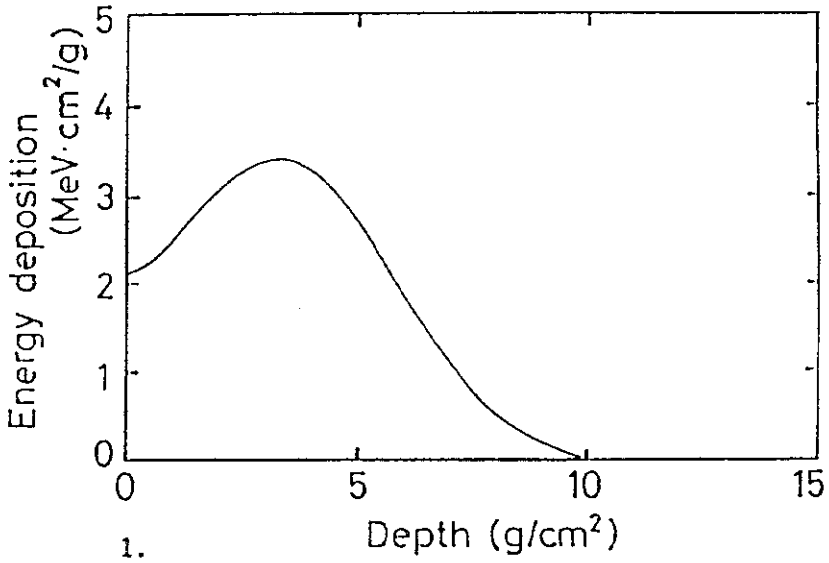

1.

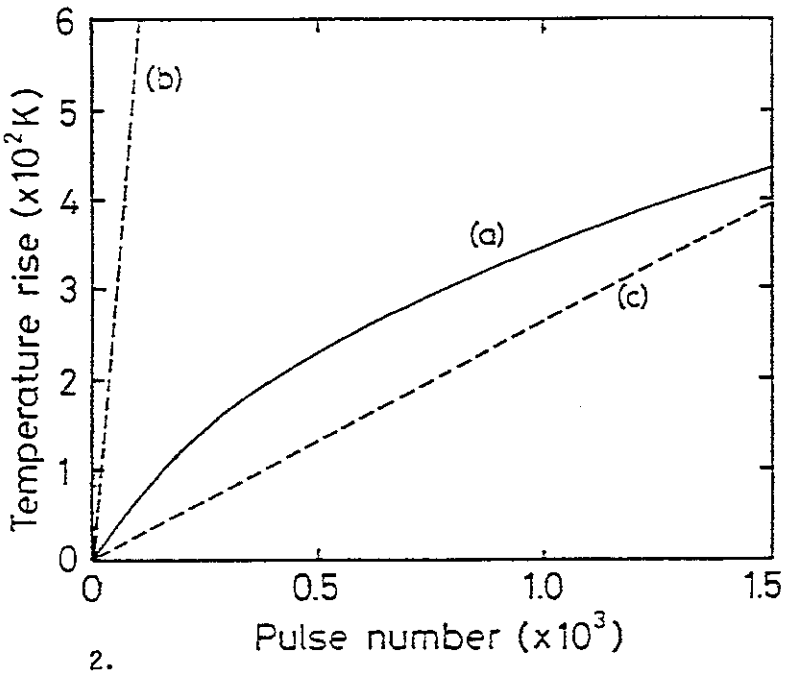

2.

Figure 4.18: 1. Energy deposition distribution of 20 MeV electrons in the semi-infinite absorber of molybdenum

2. Temperature rise within molybdenum sample during 20 MeV electron irradiation

a) measured

b) no thermal diffusion

c) uniform body heating

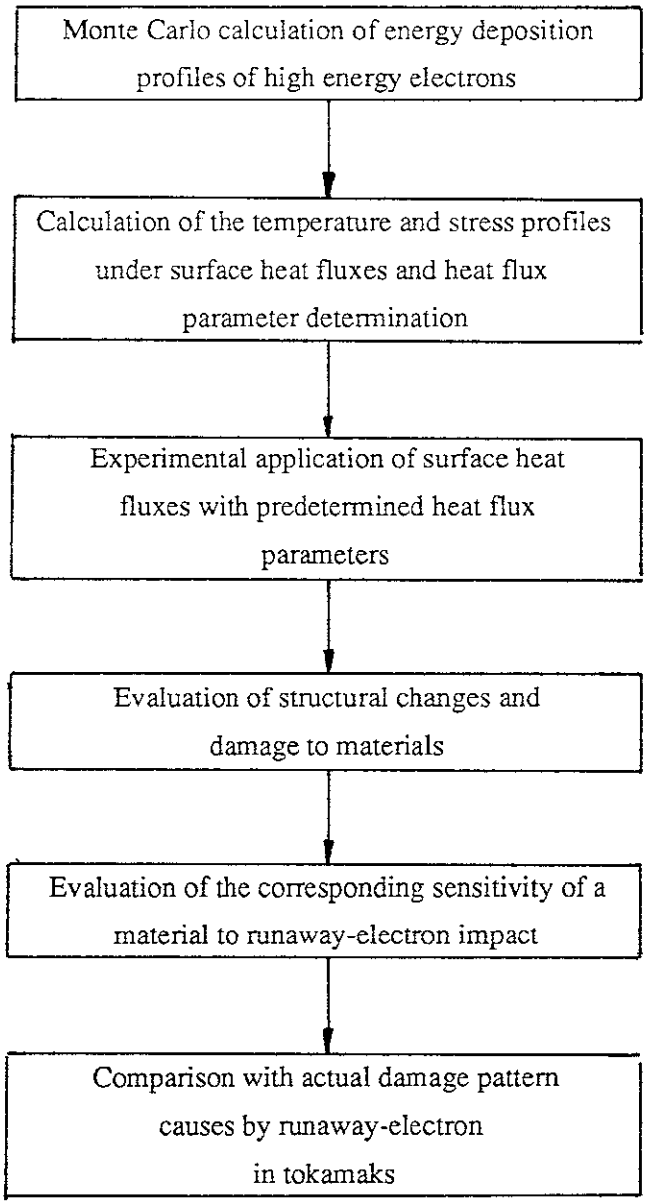

Figure 4.19: Schematic of the high heat flux correlation experiment

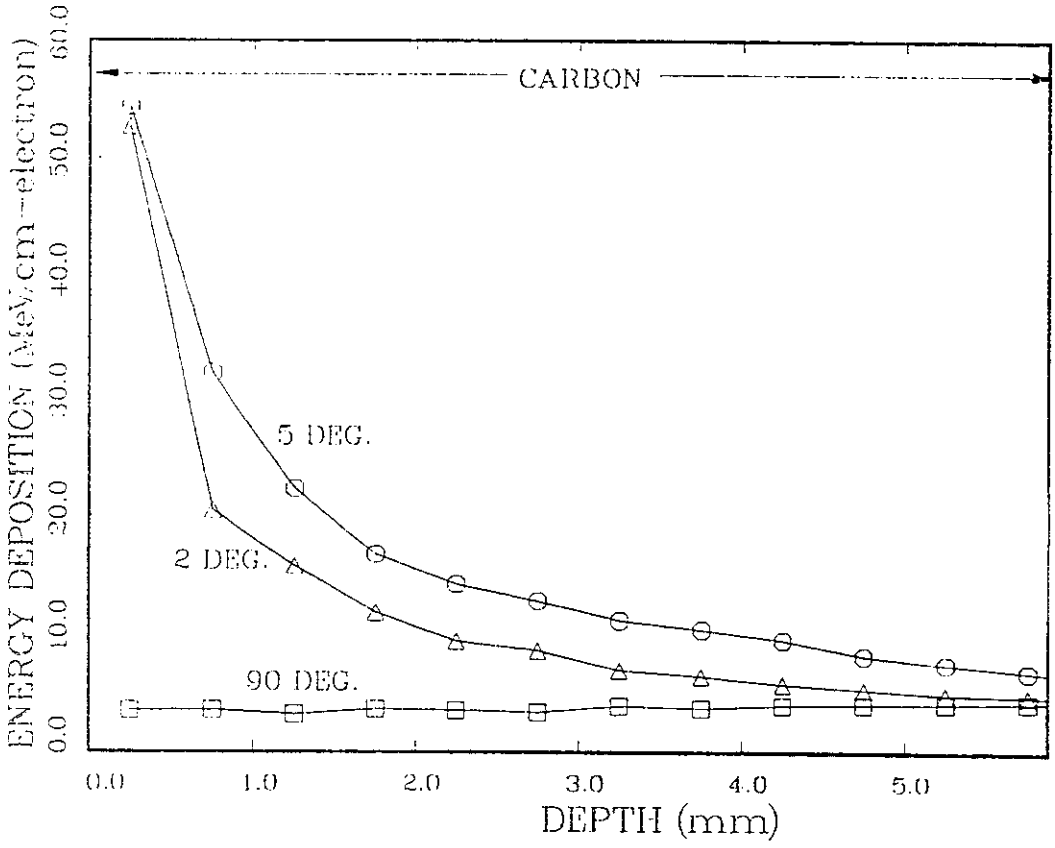

Figure 4.20: Monte Carlo calculation of the energy deposition in carbon by 20 MeV electrons under different angles of incidence |208|.

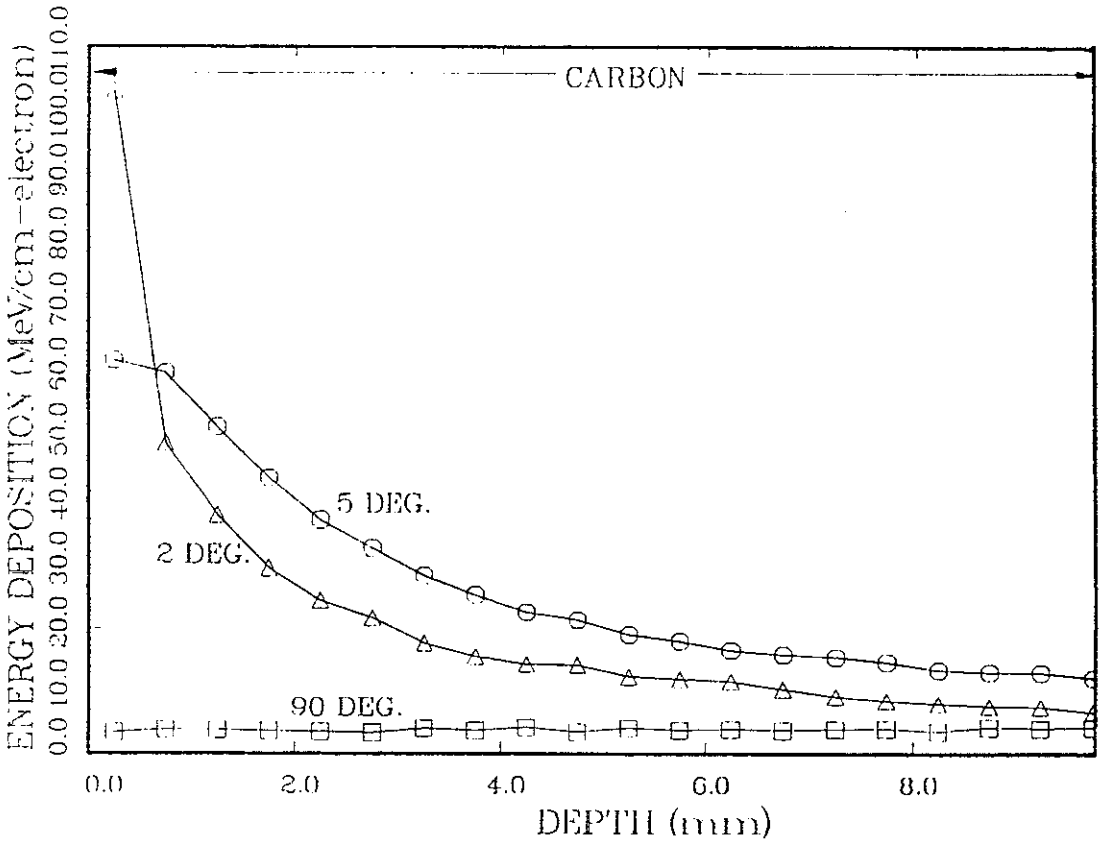

Figure 4.21: Monte Carlo calculation of the energy deposition in carbon by 50 MeV electrons under different angles of incidence |208|.

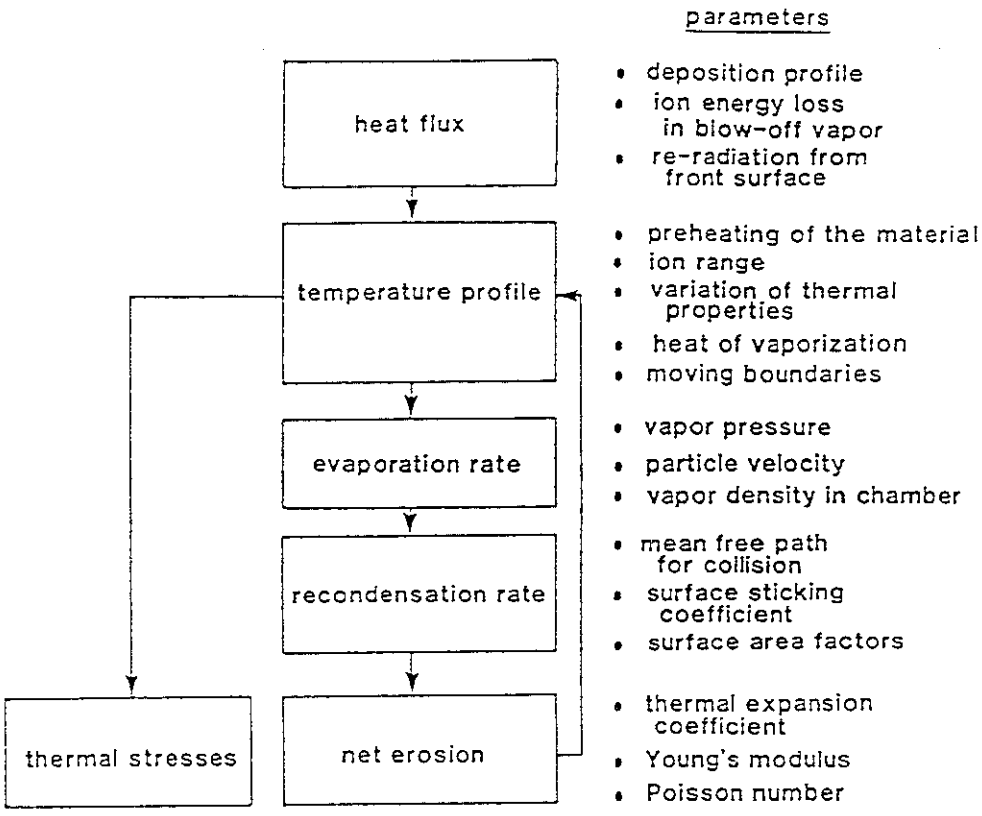

Figure 4.22: Schematic of the numerical calculation procedure used for parameter determination for the high heat flux tests.

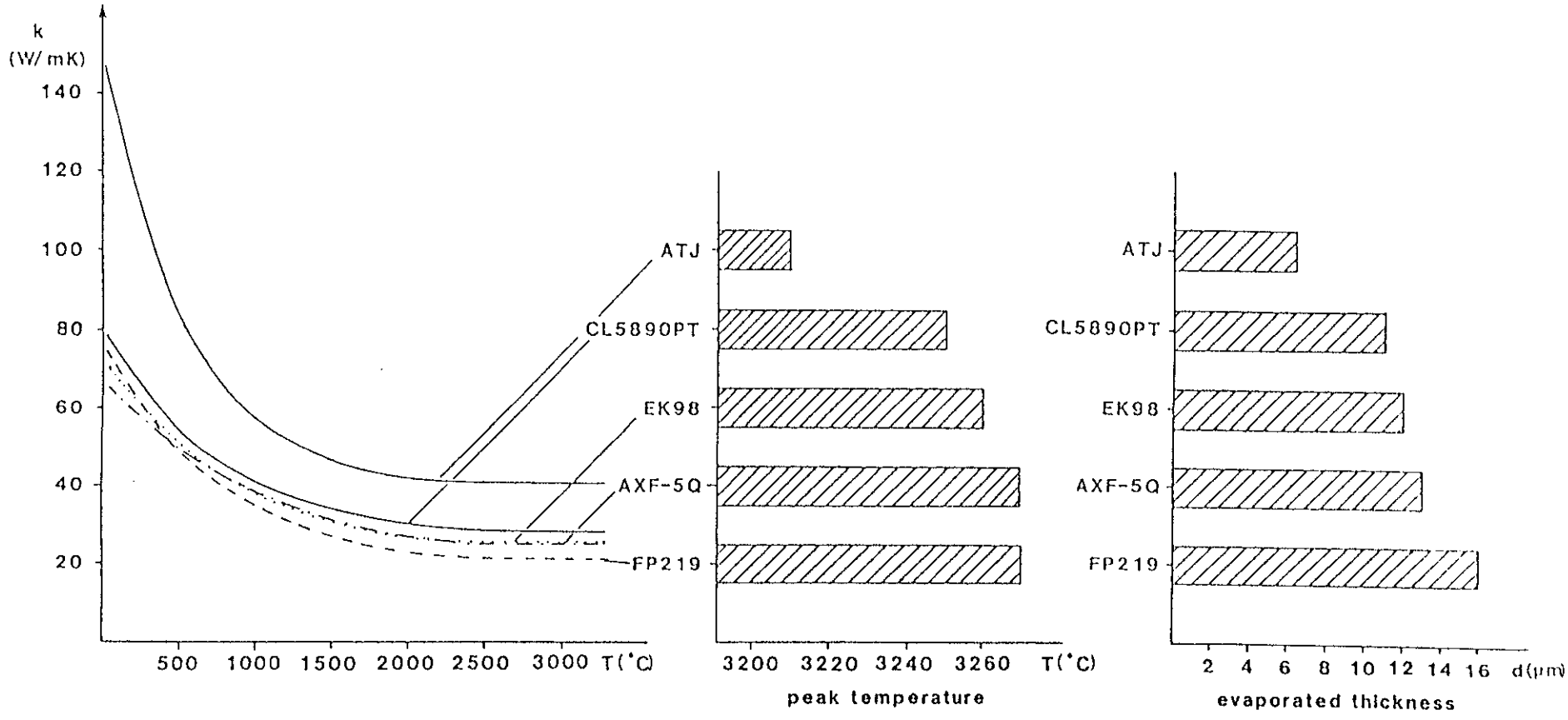

Figure 4.23: Thermal conductivity of different graphites as function of the temperature, the calculated maximum surface temperature and the thickness of the evaporated surface layer for a heat load of 200 MW/m^2 for 200 ms duration.

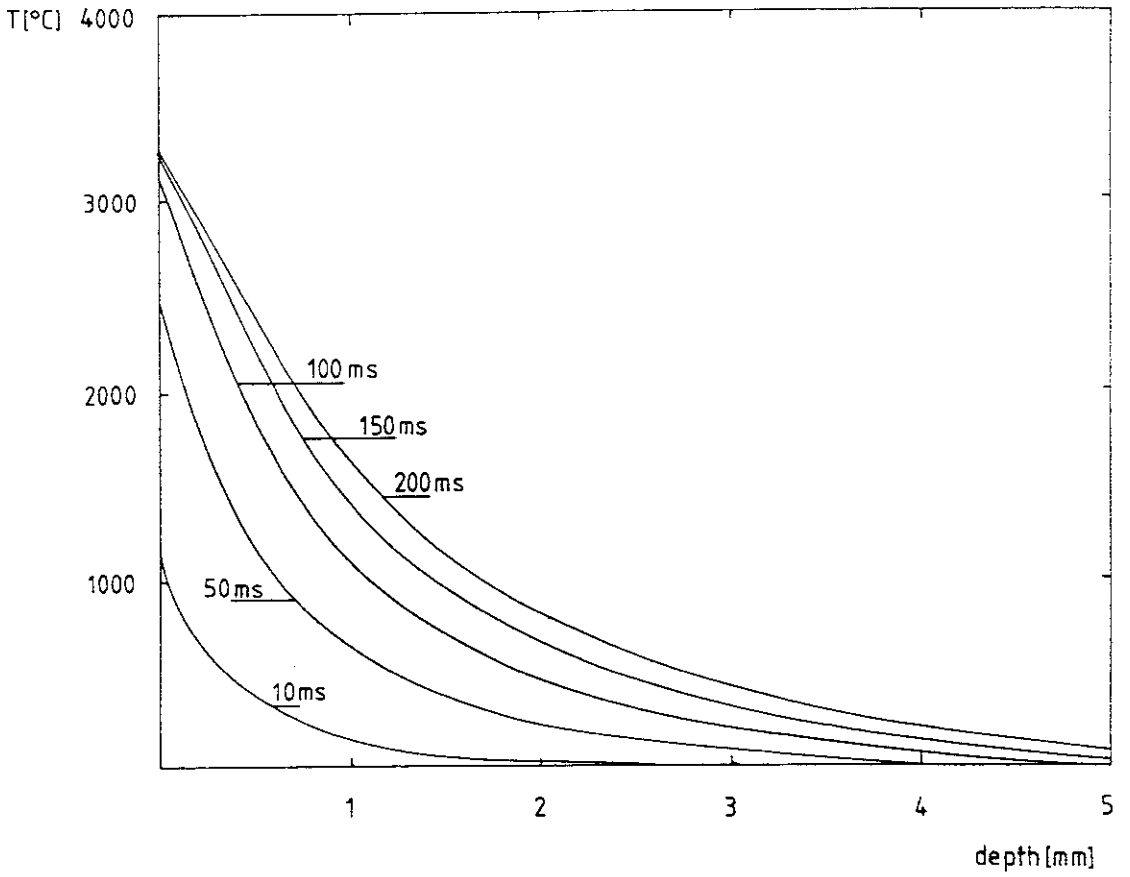

Figure 4.24: Temperature profiles in graphite AXF-5Q under a heat load of 100 MW/m^2 for various durations.

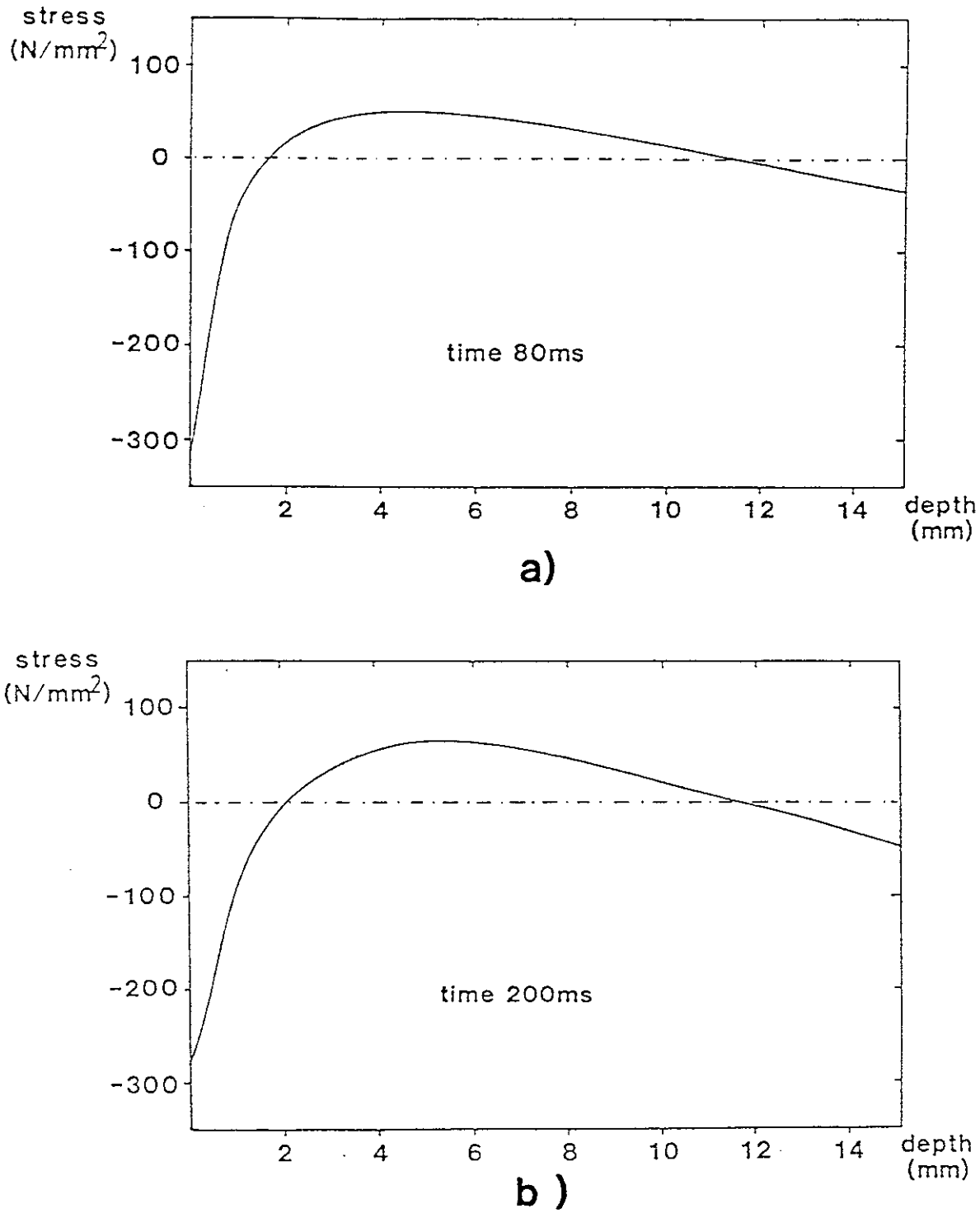

Figure 4.25: Numerically determined thermal stresses as function of the depth from the heated surface for a surface heat load of 100 MW/m^2 for the graphite AXF-5Q

a) stress distribution after 80 ms pulse length

b) stress distribution after 200 ms pulse length

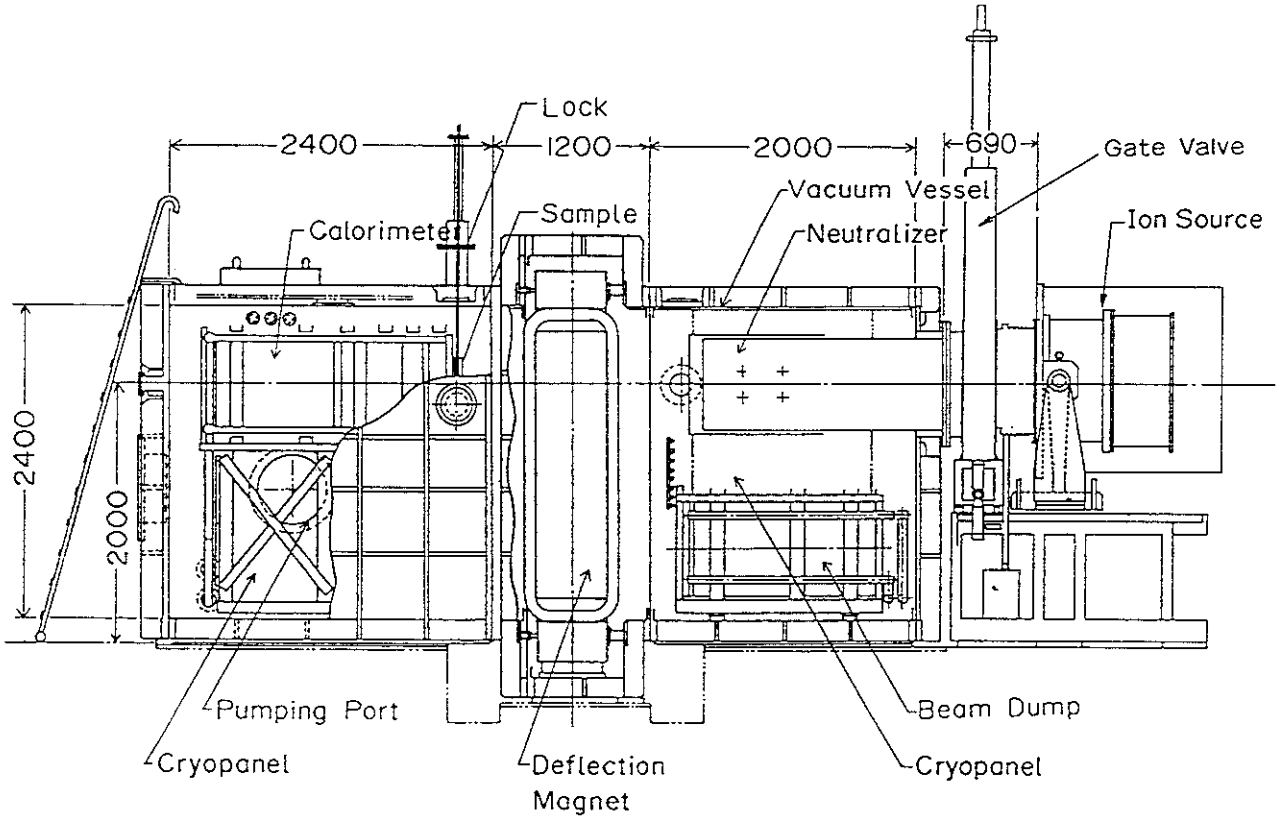

NBI - Test Stand

hydrogen beam:	120keV, 75A
beam divergence:	0.55 (horizontal axis) 1.2 (vertical axis)
electrode size:	150mm x 600mm
focal point:	9500mm
heat load on test pieces:	$\sim 150 MW/m^2$
pulse length:	<1s
size of components to be tested:	<150mm x 400 mm

Figure 4.26: Schematic and specification of the 10 MW NBI-test stand used for the experiments described in section 4.4. Materials samples can be driven in the beam line via a look system.

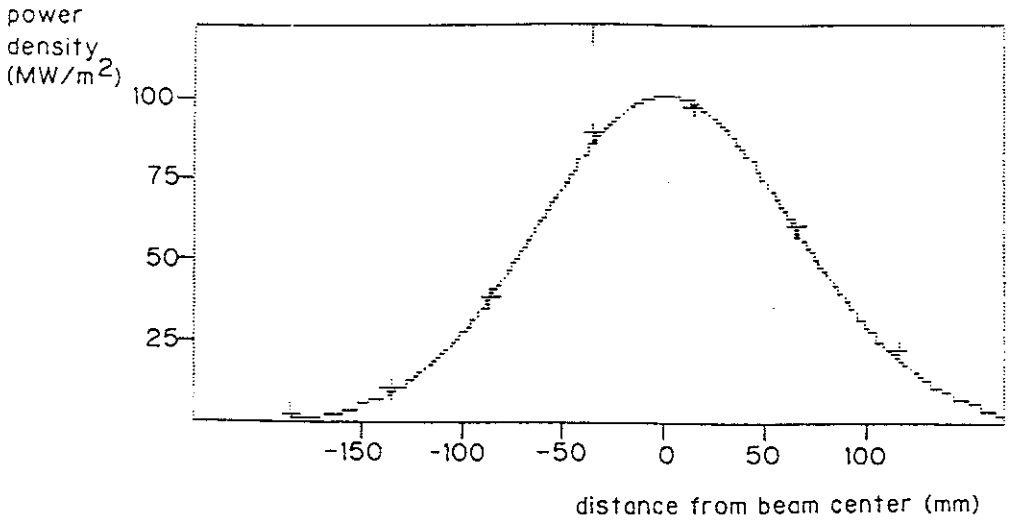

Figure 4.27: Spatial beam power density distribution for a beam pulse as applied in the experiments.

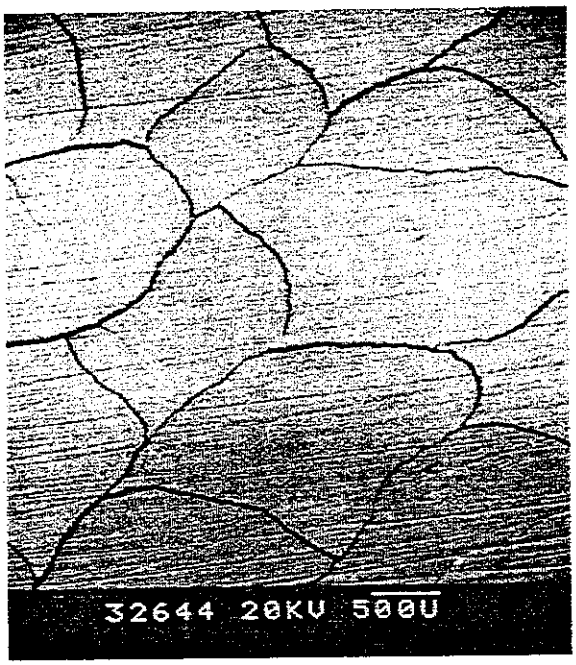

Figure 4.28: Crack pattern on the surface of an ultra fine grain graphite (ZXF-5Q) after a surface heat load of 97 MW/m^2 for 290 ms (28.1 MJ/m^2).

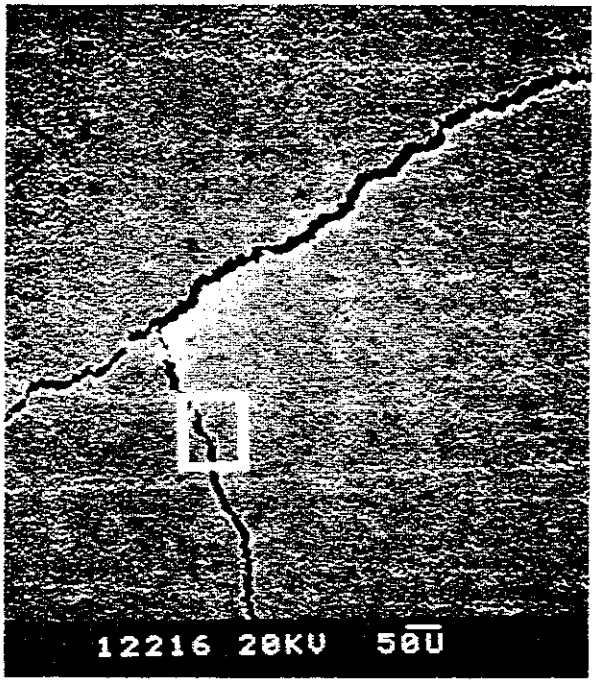

a)

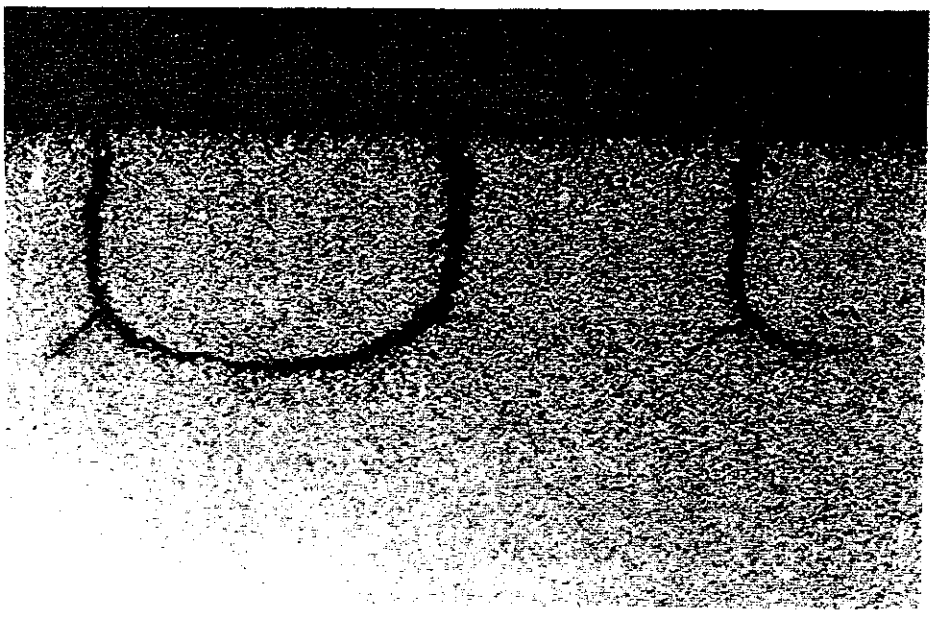

b)

500 µm

Figure 4.29: Cracks on the surface of an ultra fine grain graphite (ISO880) after a surface heat load of 93 MW/m^2 for 214 ms (19.9 MJ/m^2).

Graphite Grade	*Crack Formation occured at*		
	power density MW/m^2	*pulse length* ms	*energy* MJ/m^2
ZXF-5Q	98	145	14.2
ISO-880	91	164	14.9
T6-P	96	164	15.7
EK 98	88	183	16.1
AXF-5Q	93	176	16.4
MTK	93	183	17.0
YPD	98	189	18.5
CL5890PT	94	221	20.8
FP219	97	221	21.4
ETP-10	102	258	26.3
ATJ	105	271	28.4
JG110	103	315	32.4

band of the deposited energy which resulted in crack initiation in the tested graphites

Figure 4.30: Results of the correlation experiment on crack formation in graphite.

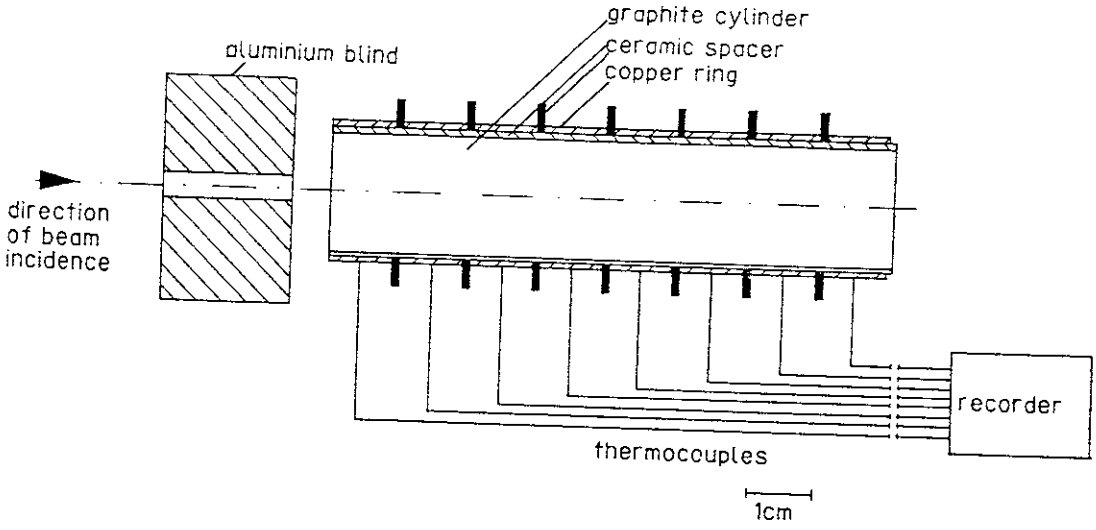

Figure 4.31: Schematic of the experimental set-up as described in section 4.5

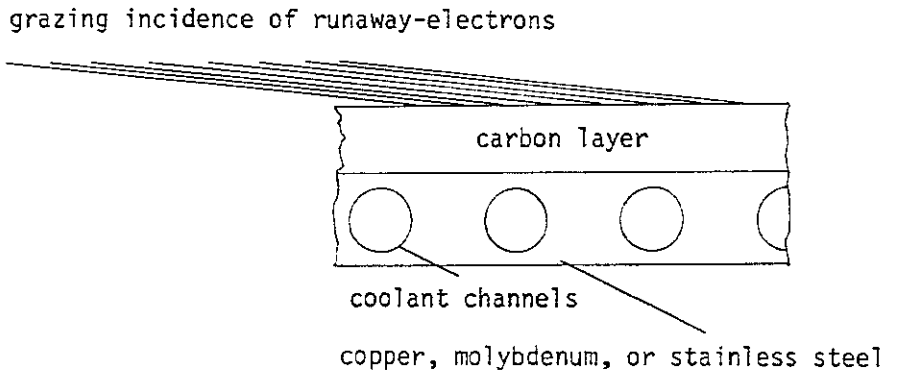

a)

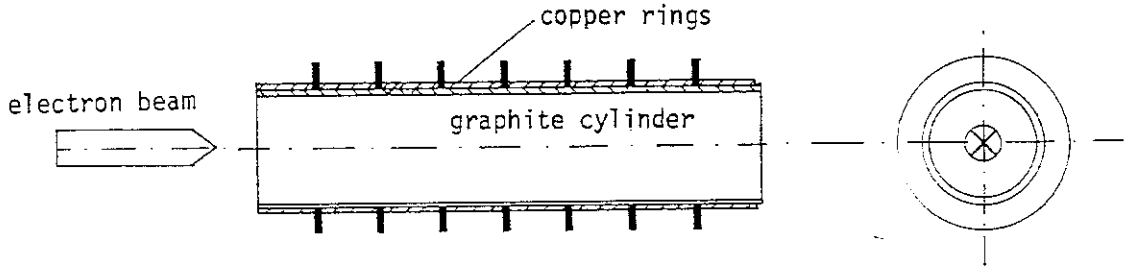

- analogy to grazing incidence
- heating of the metal due to collisional scattering of electrons/photons in graphite

b)

Figure 4.32: Comparison of the electron incidence situation in the experiments and in a tokamak.

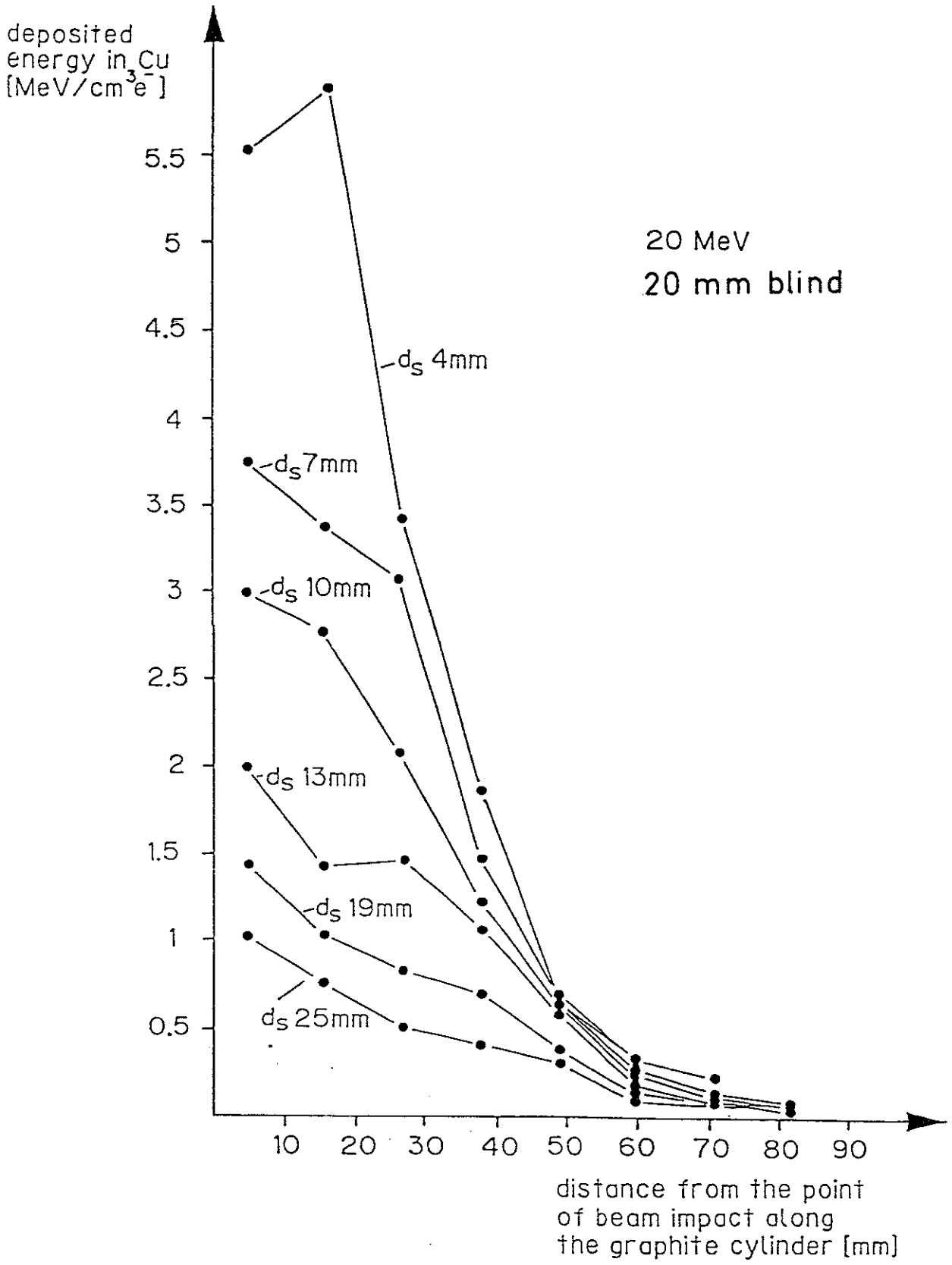

Figure 4.33: Energy deposition profiles for different diameters of the graphite cylinder d_S (20 MeV, 20 mm blind).

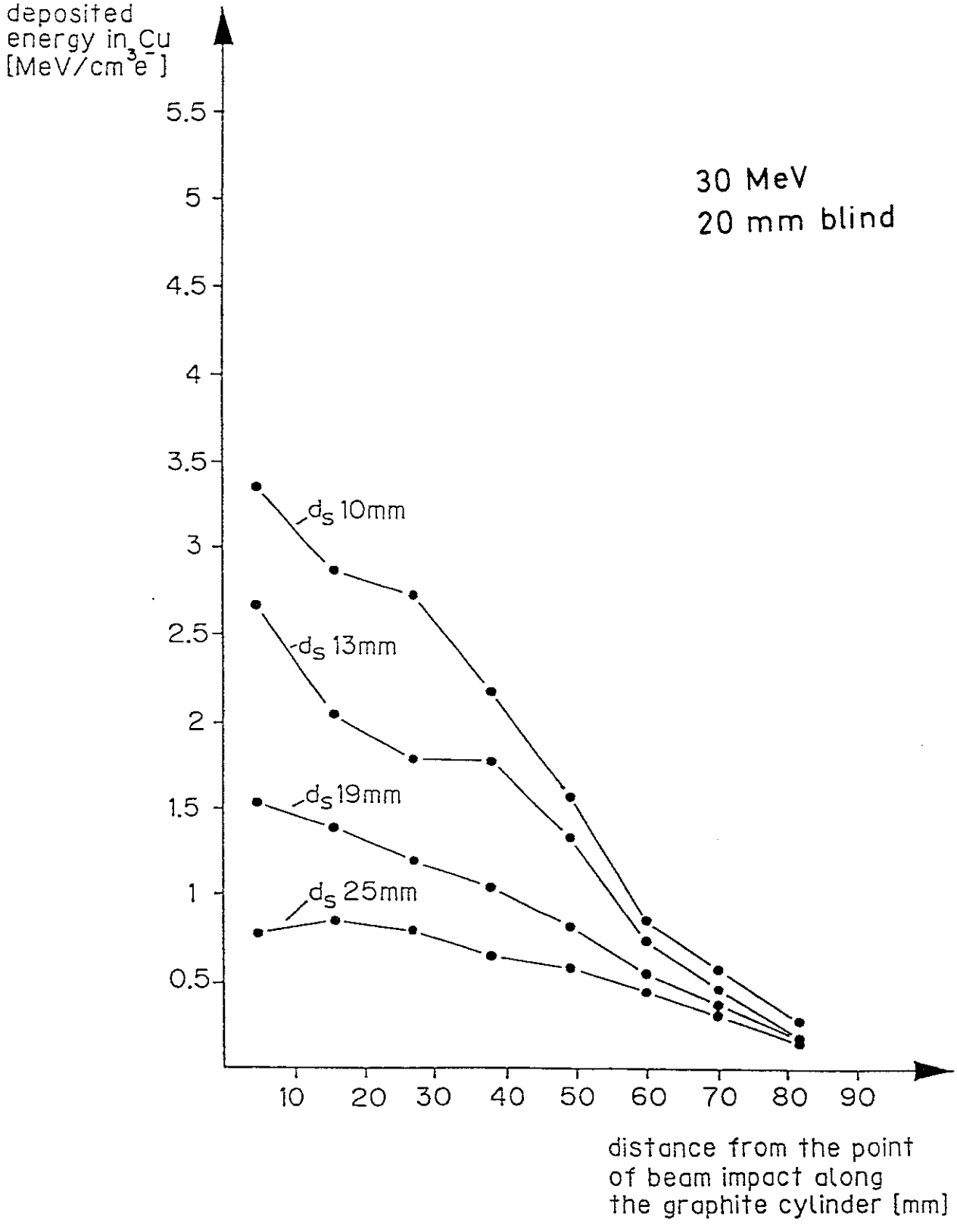

Figure 4.34: Energy deposition profiles for different diameters of the graphite cylinder d_s (30 MeV, 20 mm blind, 1st test).

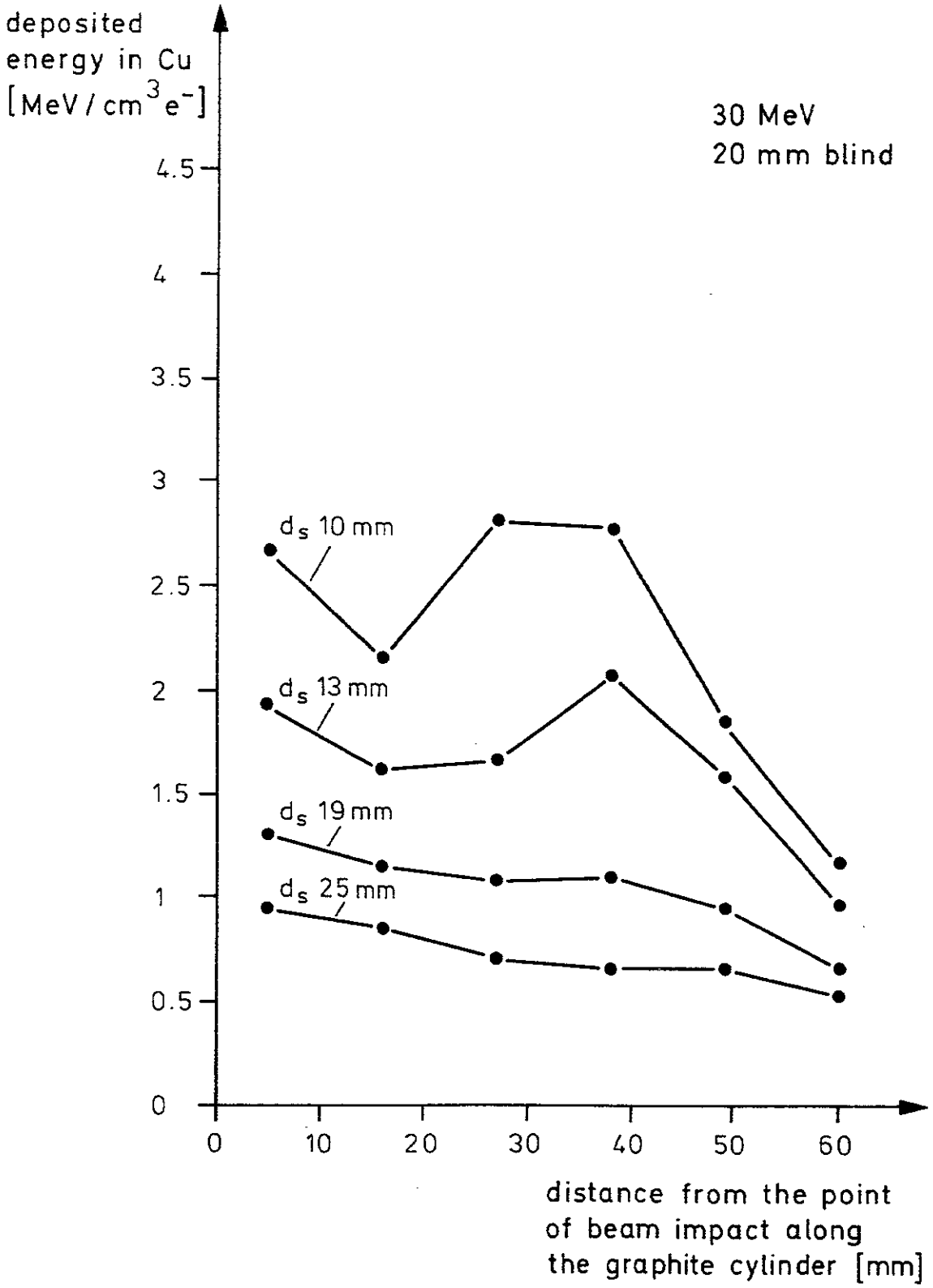

Figure 4.35: Energy deposition profiles for different diameters of the graphite cylinder d_S (30 MeV, 20 mm blind, 2nd test)

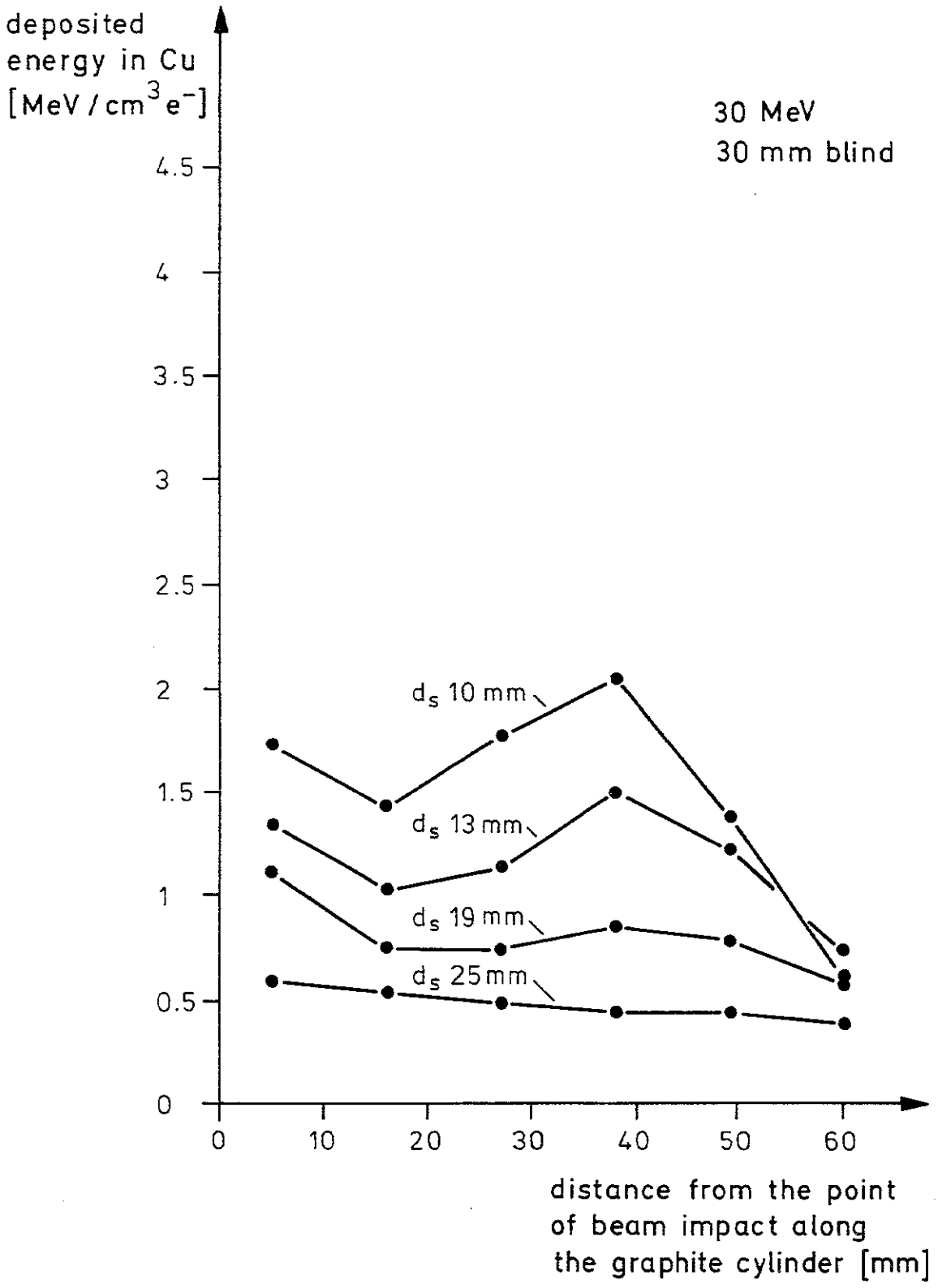

Figure 4.36: Energy deposition profiles for different diameters of the graphite cylinders d_s (30 MeV, 30 mm blind).

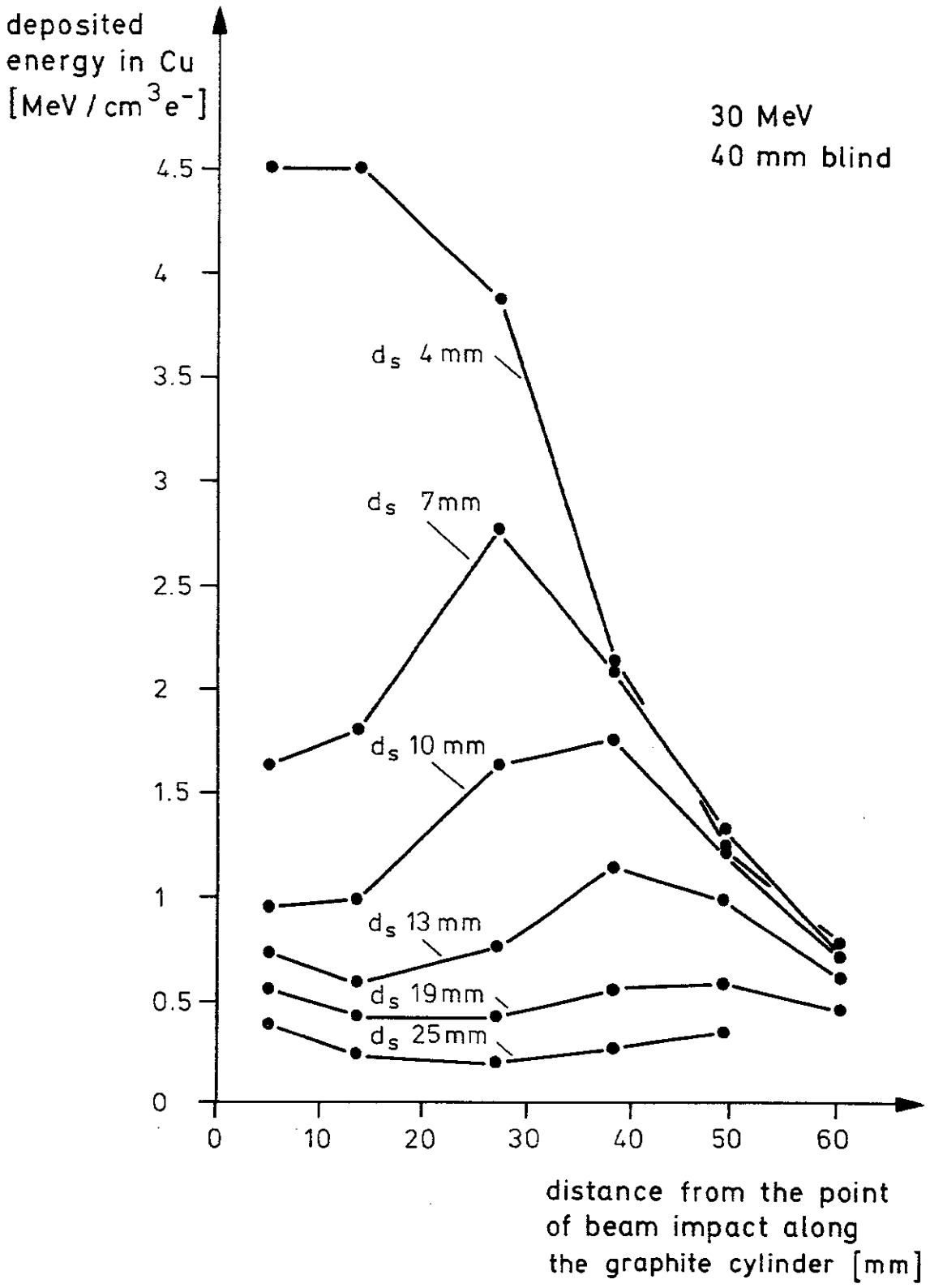

Figure 4.37: Energy deposition profiles for different diameters of the graphite cylinder d_s (30 MeV, 40 mm blind).

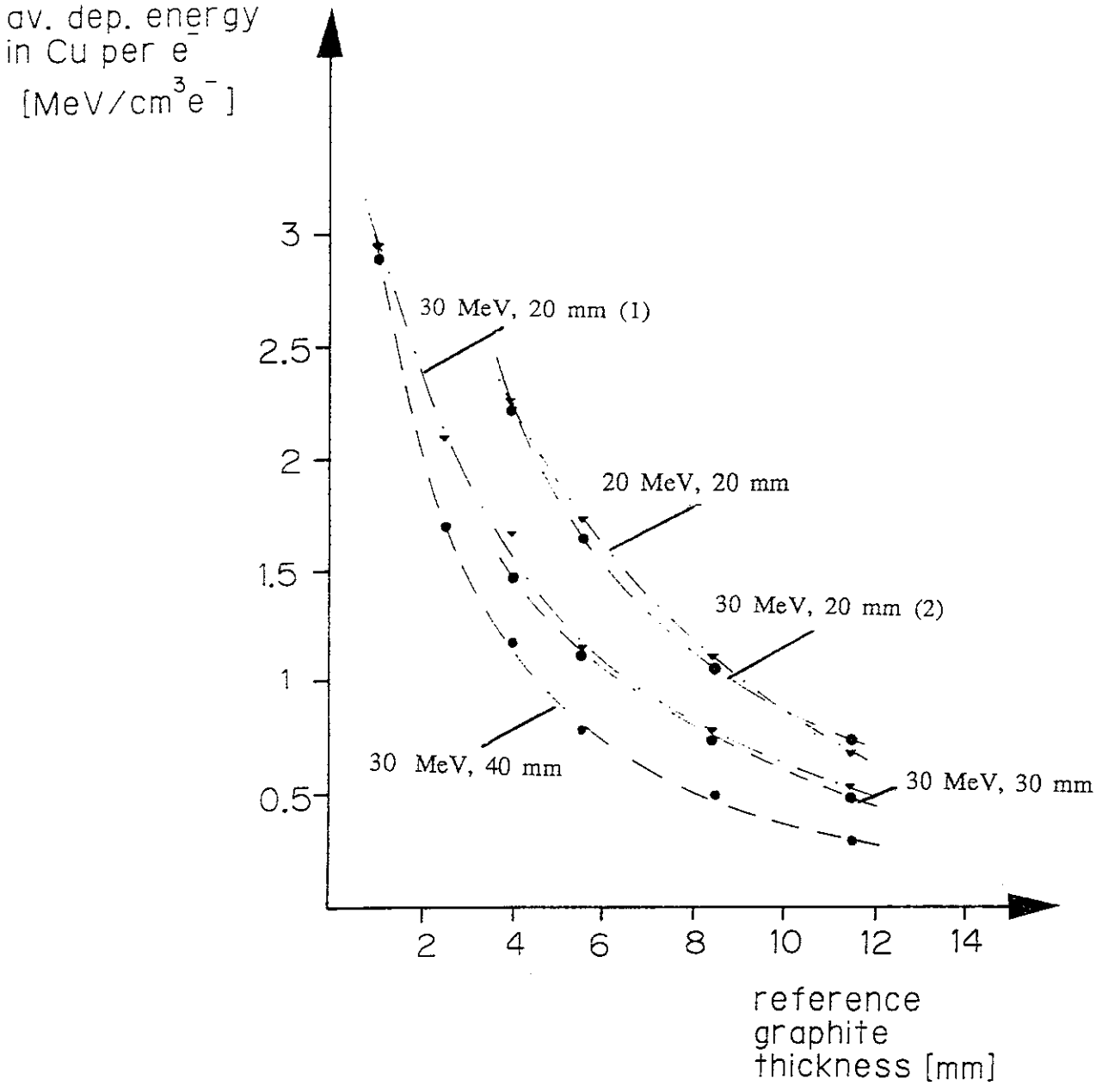

Figure 4.38: Energy deposited in the copper substrate as function of the reference graphite thickness D.

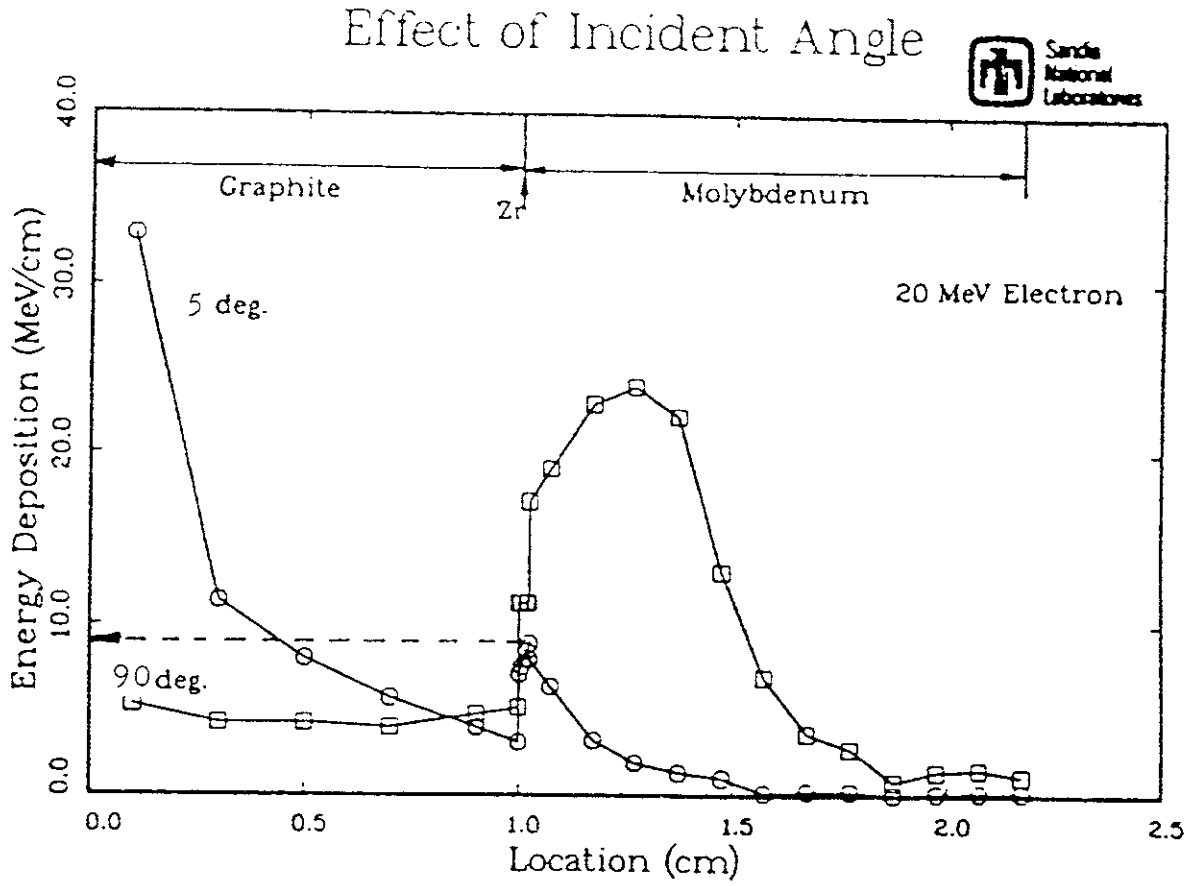

Figure 4.39: Under 5^{o} electron incidence 9 MeV/cm energy are deposited in molybdenum which is covered by 1 cm graphite |271|.

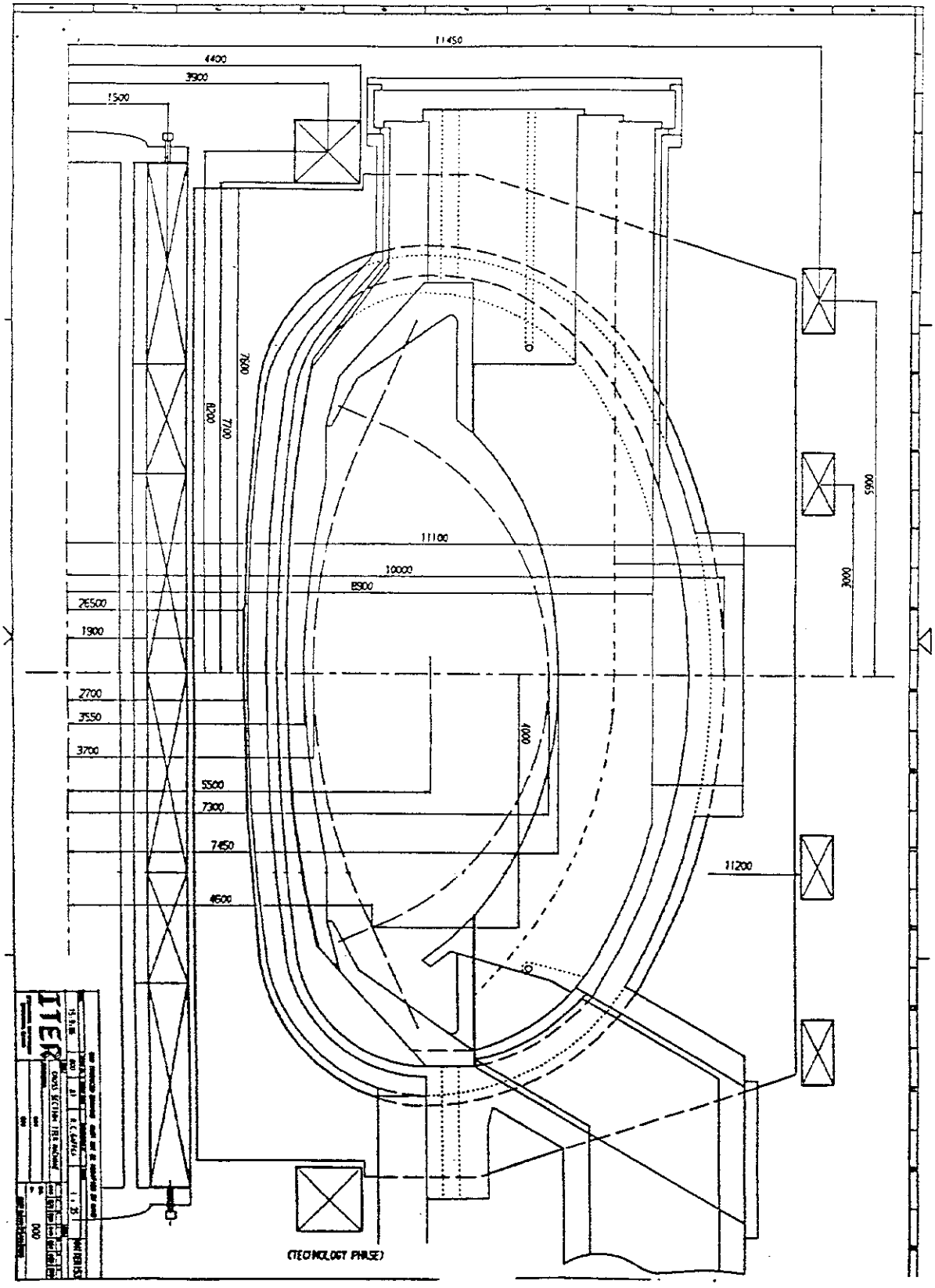

Figure 5.1: Cross-section of ITER |26|

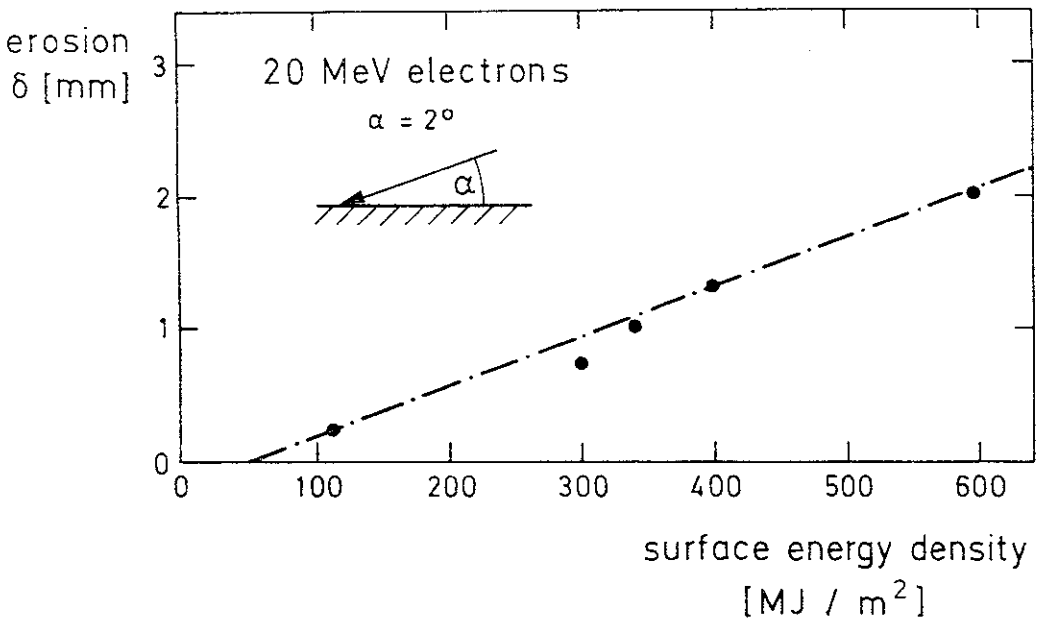

Figure 5.2: Surface erosion δ (mm) as function of the surface energy density J_{surf} (MJ/m^2) under 20 MeV electron impact (2^o).

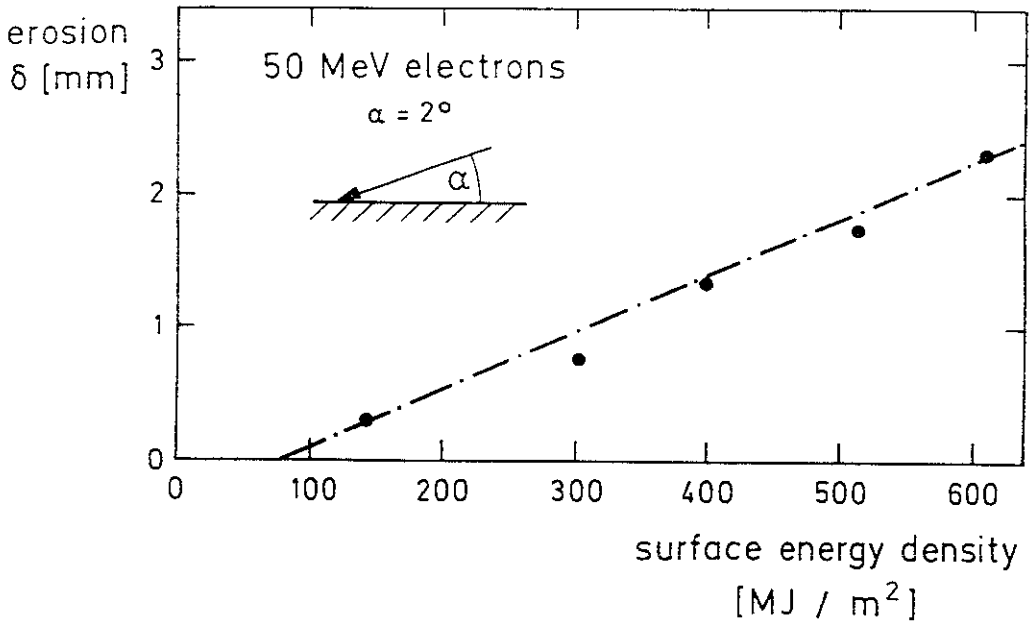

Figure 5.3: Surface erosion δ (mm) as function of the surface energy density J_{surf} (MJ/m^2) under 50 MeV electron impact (2°).

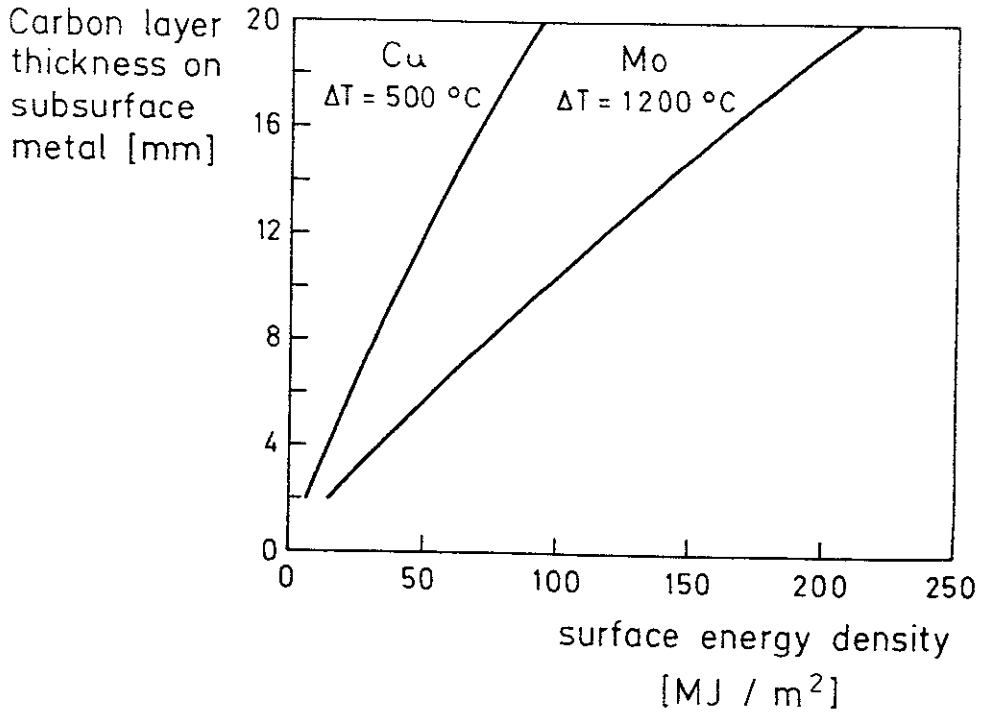

Figure 5.4: Surface energy density J_{surf} (MJ/m^2) to cause a ΔT_{Cu} = 500° C and ΔT_{Mo} = 1200°C in subsurface copper or molybdenum structures as function of the carbon layer thickness D under grazing 20-30 MeV electron impact.

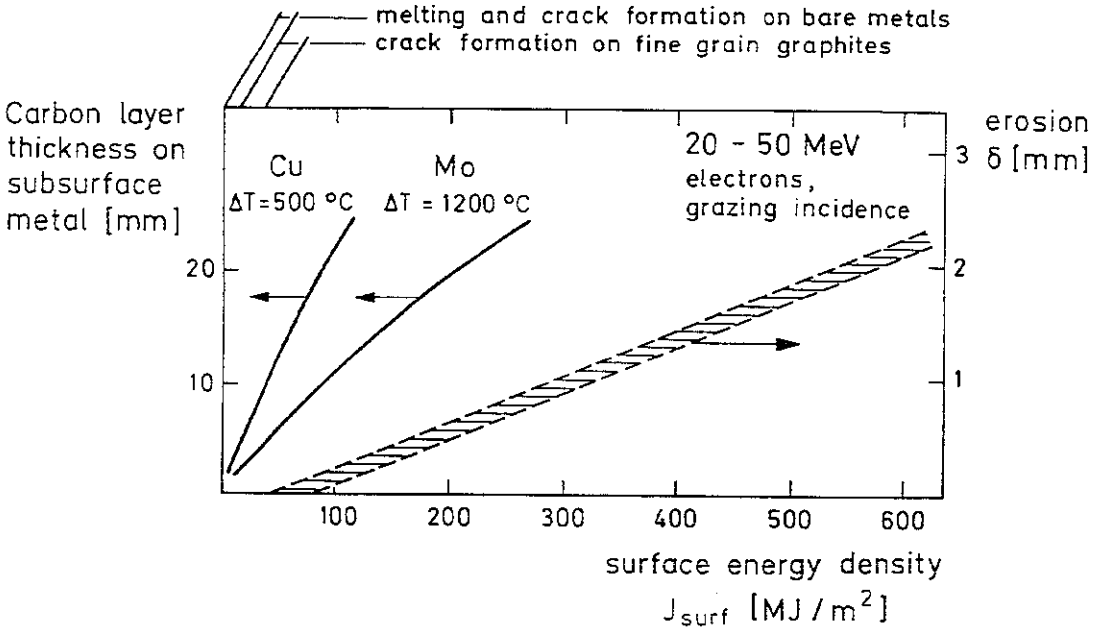

Figure 5.5: Summary of the threshold values for melting, cracking and erosion of plasma facing materials and thermal excursion thresholds for subsurface copper and molybdenum structures under grazing incidence of 20-30 (50) MeV electrons.

material	Z	A	density (g/cm^3)	melting point (°C)	specific heat at RT (J/g·K)	thermal conductivity at RT(W/m·K)
graphite (EK98)	6	12.01	1.86	3500	0.75	69*
SiC+2%AlN	10.0	20.06	3.20	2425	0.75	100
stainless steel (1.4311)	25.88	55.51	7.9	1450	0.50	14.7
Mo	42	95.94	10.2	2610	0.26	140
W	74	183.85	19.1	3410	0.14	170
Cu	29	63.55	8.95	1083	0.39	400

* at 100°C

Appendix 1.1 : Materials Properties

	AXF-5Q	CL5890PT	EK98	FP219	ATJ
density (g/cm^3)	1.83	1.79	1.86	1.76	1.74
spec. heat (J/gK)					
$c(T)=A+BT+CT^2+DT^3$					
T≤2000K /184/					
A	-2.09E-1				
B	3.94E-3				
C	-2.50E-6				
D	5.60E-10				
T>2000K /184/					
A	1.89				
B	1.26E-4				
th. cond. (W/cmK)					
$k(T)=E+FT+GT^2+HT^3$					
T≤1300K /133/					
E	8.15E-1	9.61E-1	7.41E-1	1.01	2.14
F	-5.43E-4	-6.26E-4	1.29E-4	-1.04E-3	-2.67E-3
G	1.08E-7	6.71E-8	-8.63E-7	5.27E-7	1.57E-6
H	3.81E-11	7.21E-11	4.24E-10	-8.94E-11	-3.54E-10
T≤2750K /185/					
E	9.30E-1	9.75E-1	9.37E-1	9.00E-1	1.09
F	-6.95E-4				
G	2.46E-7				
H	-3.08E-7				
T>2750K					
E	2.42E-1	2.86E-1	2.48E-1	2.12E-1	3.98E-1
Enthalpy (kJ/mol)	708.2				

	AXF-5Q	CL5890PT	EK98	FP219	ATJ
Vapor pressure (ATM) log p=I+K/T					
T≤1933K					
I		9.73			
K		-3.99E4			
T>1933K					
I		8.98			
K		-3.85E4			

Appendix 1.2 : Materials Properties used in the Computations, Section 4.4

Sample No.	*Material*	*Sample Geometry (mm)*	*Energy (MeV)*	*Pulse Number*
1	graphite EK 98	15.5 x 15.5 x 30	20	5400
2	"	"	20	7200
3	"	"	25	1200
4	"	"	30	1200
5	SiC + 2 % AlN	10 x 12 x 25	20	5400
6	"	"	25	1200
7	"	"	30	1200
8	"	"	30	7200
9	SUS316	15.5 x 15.5 x 30	20	1200
10	"	"	20	3600
11	"	"	20	5400
12	"	20 x 30	20	5400
13	"	15.5 x 15.5 x 30	20	7200
14	"	20 x 10	20	7200
15	"	20 x 30	20	7200
16	"	15.5 x 15.5 x 30	25	1200
17	"	15.5 x 15.5 x 30	25	3600
18	"	20 x 30	30	1200
19	"	20 x 30	30	3600
20	"	20 x 30	30	7200
21	"	20 x 10	30	7200
22	"	20 x 10	30	7200
23	molybdenum	20 x 10	20	3600
24	"	"	20	5400
25	"	"	20	7200
26	"	"	25	1200
27	"	"	25	3600
28	"	20 x 20	30	1200
29	"	20 x 20	30	3600
30	"	20 x 20	30	7200
31	TZM	15 x 14 x 10	20	7200
32	"	"	20	7200
33	"	"	30	7200

Sample No.	*Material*	*Sample Geometry (mm)*	*Energy (MeV)*	*Pulse Number*
34	"	"	30	7200
35	tungsten	20 x 30	20	3600
36	"	"	20	5400
37	"	"	20	7200
38	"	"	20	7200
39	"	"	30	1200
40	"	"	30	3600
41	"	"	30	7200
42	"	"	30	7200
43	SUS316 + 5 mm graphite	15 x 15 x (10+5)	20	7200
44	SUS316 + 10 mm graphite	15 x 15 x (10+10)	20	7200
45	SUS316 + 2 mm gr.	15 x 15 (10+2)	30	1200
46	SUS316 + 5mm gr.	15 x 15 (10+5)	30	1200
47	SUS316 + 10 mm gr.	15 x 15 (10+10)	30	1200
48	TZM + 2 mm gr.	15 x 15 (10+2)	20	5400
49	TZM + 5 mm gr.	15 x 15 (10+5)	20	5400
50	TZM + 10 mm gr.	15 x 15 (10+10)	20	5400
51	MoCuMo/5 mm gr.	20 x (6+5)	20	5400
52	"	20 x (6+5)	20	7200
53	MoCuMo/10 mm gr.	20 x (6 + 10)	20	7200

Appendix 2.1 : Samples and Test Parameters; Electron Linear Accelerator Tests, Section 4.2

no.	material	shot no.	pulse length (ms)	power density (MW/m^2)	weight loss (mg)	remarks
1	sandwich	18996	227	94		*, 3 shots on one sample
	sandwich	19011	170	94		
	sandwich	19058	195	102		
2	AXF-5Q	21091	258	94	11.7	
3	AXF-5Q	22127	233	92	8.7	
4	AXF-5Q	24537	176	93		
5	ZXF-5Q	29153	145	98	-0.2	
6	ZXF-5Q	29168	290	97	23.7	
7	ZXF-5Q	67	208	104	2.5	
8	ISO 880	21165	214	93	14.6	
9	ISO 880	24957	164	91		
10	T6-P	24344	164	96		
11	MT 200 K	23474	183	93	10.5	
12	CL 5890 PT	21120	221	94	16.4	
13	CL 5890 PT	23443	176	95	9.0	
14	CL 5890 PT	24713	158	94		
15	EK 98	17102	290	79		two shots on one sample
	EK 98	17120	284	81		
16	EK 98	22356	183	88	0.6	
17	EK 98	23418	176	98	12.9	
18	FE 219	29465	221	97	21.2	
19	FE 219	29566	183	103	15.2	
20	ETP-10	19383	176	98		two shots on one sample
	ETP-10	19431	202	97	28.5	
21	ETP-10	23012	195	91	7.2	
22	IG 110	18175	221	96		three shots on one sample
	IG 110	18210	202	99		
	IG 110	18234	195	105		
23	IG 110	22464	214	94	17.0	
24	IG 110	24805	202	92		

no.	material	shot no.	pulse length (ms)	power density (MW/m^2)	weight loss (mg)	remarks
25	ATJ	22321	170	93	9.6	
26	ATJ	23310	221	96	10.4	
27	ATJ	24610	183	92		
28	CGW	22449	227	97		
29	YPD (∥)	19102	353	99		two shots on one
	YPD (∥)	19115	302	101	26.5	sample
30	YPD (∥)	23158	309	96	20.3	
31	YPD (⊥)	19136	202	98		two shots on one
	YPD (⊥)	19201	189	98	31.5	sample
32	AXF-5Q	79	265	105	17.1	stress c. sample
33	AXF-5Q	425	321	103	17.7	"
34	CL 5890 PT	203	277	105	25.0	"
35	CL 5890 PT	486	252	106	22.9	"
36	ETP-10	252	258	102	23.8	"
37	ETP-10	507	214	106	13.1	"
38	IG 110	377	315	103	22.0	"
39	IG 110	632	321	104	18.7	"
40	ATJ	95	271	105	36.1	"
41	ATJ	650	201	103	10.4	"

remarks: *: 14 small size samples of 9 grades clamped together and irradiated at the same time

stress c. sample: A hole of 6 mm diameter was drilled in the surface of these samples to initiate concentration of thermal stresses at the edge of the hole.

Appendix 2.2 : Experimental Parameters, Section 4.4